

Important Notice

This copy may be used only for the purposes of research and private study, and any use of the copy for a purpose other than research or private study may require the authorization of the copyright owner of the work in question. Responsibility regarding questions of copyright that may arise in the use of this copy is assumed by the recipient.

THE UNIVERSITY OF CALGARY

**Seismic Anisotropy in Salt from Theoretical Study,
Modelling, and Field Experiments**

by

Zandong Sun

A THESIS

SUBMITTED TO THE FACULTY OF GRADUATE STUDIES
IN PARTIAL FULFILLMENT OF THE REQUIREMENTS FOR THE
DEGREE OF MASTER OF SCIENCE

DEPARTMENT OF GEOLOGY AND GEOPHYSICS

CALGARY, ALBERTA

AUGUST, 1994

© Zandong Sun 1994

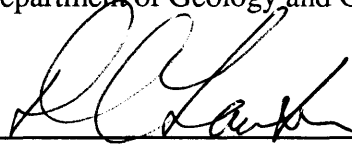
THE UNIVERSITY OF CALGARY
FACULTY OF GRADUATE STUDIES

The undersigned certify that they have read, and recommend to the Faculty of Graduate Studies for acceptance, a thesis entitled "Seismic Anisotropy in Salt from Theoretical Study, Modelling, and Field Experiments" submitted by Zandong Sun in partial fulfillment of the requirements for the degree of Master of Science.



Supervisor, Dr. R. J. Brown

Department of Geology and Geophysics



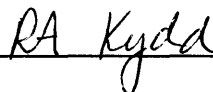
Dr. D. C. Lawton

Department of Geology and Geophysics



Dr. L. V. Hills

Department of Geology and Geophysics



Dr. R. A. Kydd

Department of Chemistry

1994-12-31

Abstract

In this thesis, it is first found that there are three types of anisotropic salt: chevron-crystal salt, recrystallized salt and burial-metamorphic salt. Velocity tests of many salt samples under varying pressure and temperature suggest that there is little resulting velocity change. But pure halite shows a different V_P/V_S pattern than mixtures of halite with sylvite and impure salt. Exact expressions for phase velocities in any arbitrary direction are derived for cubic symmetry. Group velocity formulae are also developed in symmetry planes. The maximum difference between the qSV and qSH velocities occurs in a direction halfway between symmetry axes.

Physical modelling experiments were undertaken on different types of salt, including a chevron-salt sphere. Pure chevron-salt and recrystallized-salt are found to exhibit shear-wave splitting. However, impure salts (salt mixed with clay, sands, etc.) show no shear-wave splitting. It is found that chevron-crystal salt exhibits cubic symmetry.

A pillar of potash ore was selected for a high-resolution seismic experiment in the Prairie Evaporite formation about 1 km underground in Saskatchewan. I observed shear-wave splitting for many of the three-component record sets acquired in this experiment and attribute it to the alignment of salt crystals in the rock in response to the stress field prevailing at the time of recrystallization.

Acknowledgments

After the idea of investigating and studying salt anisotropy was initiated, my supervisor, Dr. R. James Brown strongly supported the project and supervised the study in all aspects. From laboratory measurement to three-component seismic field experiment, much help was gained from many people throughout my research. Dr. Don C. Lawton provided considerable guidance and assistance on acoustic modelling in the CREWES physical modelling lab. I am grateful to Dr. Zhijing Wang for his help in carrying out velocity tests on different salts. Even though it was unsuccessful, he tried to design a new piezoelectric apparatus to measure anisotropy under varying pressure and temperature for this study. My classmate Donald T. Easley provided many constructive suggestions to this study, and we had many fruitful discussions. I gained much computer assistance from CREWES systems people.

Dr. N.C. Meijer Drees at the Geological Survey of Canada is thanked for his help in salt identification at the beginning of the research. I also had many discussions with Dr. Ron Spencer in this Department regarding salt subdivision. In the CREWES modelling laboratory I have gained help from Mr. Malcolm Bertram and Mr. Eric Gallant. Numerical modelling was done by using software developed by Sean Guest at Queen's University. During the field tests Mr. Arnfinn Prugger of Potash Corporation of Saskatchewan (PCS) coordinated and directed the field acquisition in the Allan mine, and Mr. Larry Erickson and Mr. Vance Thom, also of PCS, provided invaluable assistance during the underground experiment. We also appreciate the many helpful suggestions and knowledgeable advice that we have received from Dr. Don Gendzwill of the University of Saskatchewan. This research was supported by the CREWES Project at The University of Calgary. Permission to cut and use cores from the ERCB Core Research Centre has been very much appreciated. The field study was carried out with the cooperation and support of the Allan Division of PCS Inc.

Table of Contents

Abstract	iii
Acknowledgments.....	iv
Table of Contents.....	v
List of Tables.....	vii
List of Figures	viii
Chapter 1 – Introduction.....	1
1.1 Background.....	1
1.2 Thesis objectives and structure.....	4
1.3 Data sets used in thesis.....	4
1.3.1 Core laboratory velocity data.....	5
1.3.2 Modelling datasets.....	5
1.3.3 Three–component field experiments datasets.....	6
1.4 Hardware and software used.....	6
Chapter 2 – Salt classification and velocities measurement in laboratory.....	8
2.1 Introduction.....	8
2.2 Salt classification.....	9
2.3 Laboratory measurement of compressional- and shear-wave velocities.....	18
2.3.1 Experimental apparatus and procedure.....	18
2.3.2 Experimental results.....	20
2.3.2.1 Pressure effects.....	21
2.3.2.2 Temperature effects	29
2.3.2.3 Sensitivity analysis of V_P/V_S pattern.....	33
Chapter 3 – Theory of anisotropic media of cubic symmetry	36
3.1 Introduction.....	36
3.2 Determination of anisotropic parameters of salt.....	36
3.3 Formulae for phase and group velocities in media of cubic symmetry	39

3.3.1 Phase Velocity	41
3.3.1.1 P-wave phase velocity	41
3.3.1.2 SV-wave phase velocity	41
3.3.1.3 SH-wave phase velocity.....	41
3.3.2 Group Velocity.....	42
3.4 Phase and group velocity surfaces in cubic salt	44
Chapter 4 – Physical modelling with salts and numerical modelling with cubic salt	48
4.1 Introduction.....	48
4.2 Physical modelling with different types of salt.....	49
4.2.1 Experimental setup	49
4.2.2 Zero-offset azimuthal-rotation transmission experiment	50
4.2.3 Offset transmission experiment	55
4.2.4 Transmission experiment around a chevron-salt sphere	63
4.3 Numerical modelling with cubic salt.....	68
4.3.1 Model description.....	68
4.3.2 Analysis of VSP synthetic seismograms.....	70
Chapter 5 – Three-component seismic anisotropy experiment around a salt pillar	75
5.1 Introduction.....	75
5.2 The high-resolution experiment	76
5.3 Results and interpretation	80
5.4 Discussion	87
Chapter 6 – Conclusions	89
References	92
Appendix A – P- and S-wave velocities of salt versus pressure	97
Appendix B – P- and S-wave velocities of salt versus temperature.....	98
Appendix C – Empirical relations between seismic velocities and pressure or between seismic.....	99
Appendix D – Phase and group velocity in anisotropic media of cubic symmetry.....	103

List of Tables

Table 2.1.	Salt classification and velocity properties.....	17
Table 3.1.	Salt anisotropy parameters.....	39
Table 4.1.	Velocities on different types of salt samples	55
Table 5.1.	Field recording parameters for all experiments.....	78

List of Figures

FIG. 1.1.	P-wave velocity-density relationship for different lithologies showing salt's special location in the density-velocity plot (after Gardner, 1974).....	2
FIG. 2.1.	Photographs of all types of salt samples.....	11
FIG. 2.2.	Crystal framework of three major types of salt: (a) chevron-crystal salt; (b) detrital salt; (c) recrystallized, burial-metamorphic salt.....	15
FIG. 2.3.	Temperature dependence of the intensities of the preferred fibres in extruded synthetic salt and natural salt.	16
FIG. 2.4.	Schematic diagram of the acoustic measurement system in Core Laboratories for ultrasonic shear-wave (V_S) and compressional-wave (V_P) velocity measurement.....	19
FIG. 2.5.	(a) V_P and V_S and (b) V_P/V_S ratio versus pressure in an impure salt sample.. ..	21
FIG. 2.6.	(a) V_P and V_S and (b) V_P/V_S ratio versus pressure in a salt sample composed of halite and sylvite.	23
FIG. 2.7.	(a) V_P and V_S and (b) V_P/V_S ratio versus pressure in a large pure recrystallized halite sample.....	24
FIG. 2.8.	(a) V_P and V_S and (b) V_P/V_S ratio versus pressure in a recrystallized pure halite sample with dissolution cavities.....	25
FIG. 2.9.	(a) V_P and V_S and (b) V_P/V_S ratio versus pressure in a visually layered recrystallized pure halite sample.....	26
FIG. 2.10.	(a) V_P and V_S and (b) V_P/V_S ratio versus pressure in pure huge halite crystal with minor clay fragments.	27
FIG. 2.11.	(a) V_P and V_S and (b) V_P/V_S ratio versus pressure in pure halite of detrital-framework salt.	28
FIG. 2.12.	(a) V_P and V_S and (b) V_P/V_S ratio versus pressure in a salt sample of fine crystal halite and minor sylvite.	30
FIG. 2.13.	(a) V_P and V_S and (b) V_P/V_S ratio versus pressure in a salt sample composed of halite with sylvite.	31
FIG. 2.14.	(a) V_P and V_S and (b) V_P/V_S ratio versus pressure in a pure halite sample. .	32
FIG. 2.15.	Pressure V_P/V_S pattern sensitivity analysis for pure halite.....	34
FIG. 2.16.	Pressure V_P/V_S pattern sensitivity analysis for impure halite.....	34
FIG. 2.17.	Pressure V_P/V_S pattern sensitivity analysis for detrital-framework salt.	35
FIG. 2.18.	Temperature V_P/V_S pattern sensitivity analysis for pure halite.	35

FIG. 3.1.	Photograph of a pure large halite crystal (measuring 115×115×100 mm) for deducing salt anisotropic parameters.	37
FIG. 3.2.	Crystal symmetry and definition of directions (1,0,0), (1,1,0) and (1,1,1) and symmetry planes {1,0,0}, {0,1,0} and {0,0,1}.	37
FIG. 3.3.	Schematic diagram of a wavefront in an anisotropic medium at times t and $t + \delta t$, showing the phase and group velocities (v and V respectively), their respective unit vectors (n_i and ξ_i) and the angle Δ between n_i and ξ_i . (modified after Cheadle et al., 1991).	45
FIG. 3.4.	Phase-velocity surfaces for compressional and shear waves in two quadrants on section {0,0,1} (symmetry plane) for cubic salt.	45
FIG. 3.5.	Phase-slowness surfaces for compressional and shear waves in the first quadrant on section {0,0,1} (symmetry plane) for cubic salt.	47
FIG. 3.6.	Group-velocity (wave) surfaces for compressional and shear waves in the first quadrant on section {0,0,1} (symmetry plane) for cubic salt.	47
FIG. 4.1	Schematic diagram of the apparatus used for shear-wave splitting experiments showing that it clamps the sample between two shear-wave transducers of parallel and orthogonal polarization. During the experiment the sample is rotated while the transducers remain fixed. A circular protractor scale is used to determine the azimuth of the rotation.	50
FIG. 4.2.	Shear-wave record from a zero-offset transmission experiment on a pure salt crystal (axis length: 100.4 mm). The rotation axis is a principal axis of symmetry (approximately) of the salt crystal . Both shear-wave transducers were rotated from 0° to 360° at increments of 11.25°.	51
FIG. 4.3	Shear-wave record of zero-offset transmission experiment on a chevron-salt sample (length: 279.9 mm) with the same experimental setup as in figure 4.2; the rotational axis is the long axis of the core.....	52
FIG. 4.4.	Shear-wave record of a zero-offset transmission experiment on a recrystallized salt sample (length: 95.9 mm, crystal size: 1-6 mm) with the same experiment setup as in figure 4.2; the rotation axis is long axis of the core.	53
FIG. 4.5	Shear-wave record of a zero-offset transmission experiment on an impure salt sample mixed uniformly with clay (length: 145.4 mm) with the same experimental setup as in figure 4.2; the rotational axis is the long axis of the core.	54
FIG. 4.6	Plan view and cross-sectional schematic diagram of offset transmission	

	experiment. D (depth) is the length of the salt sample. X is the lateral offset of the receiver position, and H is the hypotenuse connecting the source and receiver. The distance is scaled by 1:10,000.	56
FIG. 4.7.	Schematic diagram of the energy radiation pattern of the offset transmission experiment showing that most energy is restricted within a narrow range of incidence angles (near-offset). The further the offset, the less the energy propagating through.	57
FIG. 4.8.	Shear-wave splitting rationale in an anisotropic medium of cubic symmetry. Away from the symmetry axes (three directions) shear-wave splitting can be observed.	58
FIG. 4.9.	Record of a source-receiver offset transmission experiment along line 2 with a P-wave source and P-wave receiver.	59
FIG. 4.10.	Shear-wave record of a source-receiver offset transmission experiment along line 3 with inline shear (S1) source and both inline (a) and crossline (b) receivers.....	60
FIG. 4.11.	Shear-wave record of a source-receiver offset transmission experiment along a random line (line 1) with inline shear source and crossline receiver, showing fast shear (S1) and slow shear (S2) and polarity reversal of S1. ..	61
FIG. 4.12.	Shear-wave record of a source-receiver offset transmission experiment along line 2 with inline shear (S1) source and (a) inline and (b) crossline receivers.	62
FIG. 4.13.	Schematic diagram of modelling geometry showing layout of source and receiver, black dots representing locations of transducers (source and receiver). All the source-receiver pairs connected by straight lines. The source and receiver were moved after each 'shot' was finished at each pair of locations (one straight line).	64
FIG. 4.14.	Group velocities against ray angle calculated from the theoretical equations discussed in chapter 3.	65
FIG. 4.15.	Zero-offset shear transmission record over a chevron-salt sphere along circle 1: a) R-R polarization; b) T-T polarization; c) T-R polarization.....	66
FIG. 4.16.	Zero-offset shear transmission record over a chevron-salt sphere along circle 2: a) R-R polarization; b) T-T polarization; c) T-R polarization.....	67
FIG. 4.17.	Schematic diagram of a VSP numerical model and model parameters with a cubic anisotropic layer (layer 2).	68
FIG. 4.18.	Ray diagram, time-distance curves, multisource three-component synthetic seismograms generated by source B (1000 m offset) with a 500 m thickness	

of salt (layer 2).

- (a) Ray diagram of an SV source (bottom) and time–distance curves (top);
- (b) VSP synthetics generated by shear sources at location B; shear waves recorded on the radial and vertical components (left and right panel) are generated by a radial (inline) shear source; the shear wave recorded on the transverse component (middle panel) was generated by a transverse (crossline) shear source. 72

FIG. 4.19. Ray diagram, time–distance curves, multisource three–component synthetic seismograms generated by source B (400 m offset) with 500 m thickness of salt (layer 2).

- (a) Ray diagram of SV source (bottom) and time–distance curves (top);
- (b) VSP synthetic seismograms generated by shear sources at location A; shear waves recorded on radial and vertical component (left and right panel) were generated by a radial (inline) shear source; the shear wave recorded on the transverse component (middle panel) was generated by a transverse (crossline) shear source. 73

FIG. 4.20. Ray diagram, time–distance curves, multisource three–component synthetic seismograms generated by source A (400 m offset) with 100 m thickness salt (layer 2).

- (a) Ray diagram of SV source (bottom) and time–distance curves (top);
- (b) VSP synthetic seismograms generated by shear sources at location A; shear waves recorded on radial and vertical component (left and right panel) are generated by a radial (inline) shear source; the shear-wave recorded on the transverse component (middle panel) was generated by a transverse (crossline) shear source. 74

FIG. 5.1. A stratigraphic section of the mining zone showing the location of the experiment. 77

FIG. 5.2. Plan view of the experimental salt pillar showing source and receiver locations and mine-survey stations. Three-component record sets are displayed below for the highlighted source locations..... 78

FIG. 5.3. Three-component record set for the shotpoint at S-6, i.e. south wall, shot location 6. There is little or no shear-wave splitting observed..... 82

FIG. 5.4. Three-component record set for the shotpoint at E-12, i.e. east wall, shot location 12. There is no obvious shear-wave splitting observed, this is particularly on the farthest offsets..... 83

FIG. 5.5. Three-component record set for the shotpoint at W-22, i.e. west wall, shot

location 22. There appears to be significant shear-wave splitting on all traces.

..... 84

FIG. 5.6. Three-component record set for the shotpoint at E-2, i.e. east wall, shot location 2. There appears to be significant shear-wave splitting on all traces. .

..... 85

FIG. 5.7. Three-component record set for the shotpoint at E-28, i.e. east wall, shot location 28. There appears to be significant shear-wave splitting on all traces.

.....86

Chapter 1 - Introduction

1.1 Background

Devonian salts play a very important role in hydrocarbon accumulation and distribution in western Canada (Anderson and Brown, 1991a, b). The Athabasca anticline, the largest single liquid oil accumulation in the world indicated by new data, is a trap structure caused by Devonian salt removal (Masters, 1984).

The importance of salt units and their history of dissolution and deformation in sedimentary basins has been documented by many authors (e.g. De Mille et al., 1964; Parker, 1967; Smith and Pullen, 1967; Langstroth, 1971; Lohmann, 1972; Edmunds, 1980; Oliver and Cowper, 1983; Simpson, 1984; Wilmot, 1985; Hopkins, 1987; Jenyon and Taylor, 1987; Jenyon, 1988; Anderson, 1991; Anderson and Brown, 1991a, b). Dissolution in the western Canada basin, particularly of Devonian salt units, and the subsequent differential subsidence, has helped to establish hydrocarbon reservoirs by creating structural closure in the overlying section, as well as various controls on contemporaneous or later deposition. Edmunds (1980) has stated that salt removal is perhaps the most important hydrocarbon-trapping mechanism in western Canada. Salt remnants and dissolution features can also, unless fully recognized, lead to gross misinterpretation in the subsurface in terms of reefs, basement structure, etc. By *salt* we mean primarily halite (NaCl) but potash or sylvite (KCl) often occurs together with halite and both have cubic symmetry.

Among sedimentary rocks, as documented by Gardner et al. (1974), salt is a special type of rock. It has anomalously high velocity (4.5 to 5.5 km/s) and low density (2000 to 2200 kg/m³) (Figure 1.1). Salt may be changed from elastic to anelastic rock at lower temperature and pressure, compared with other sedimentary rocks.

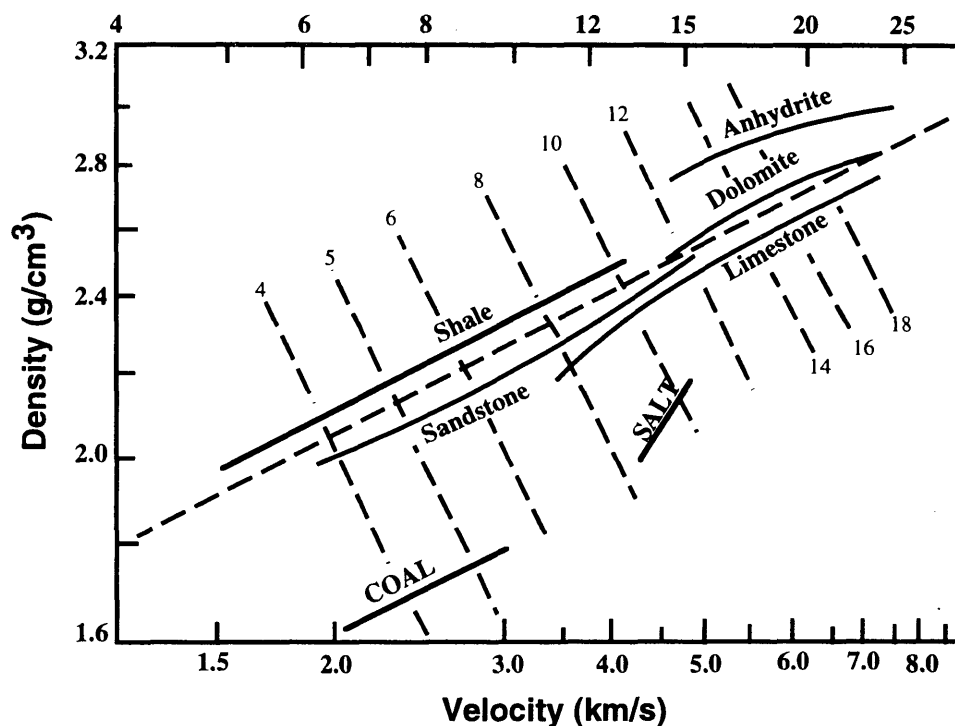


FIG. 1.1. P-wave velocity-density relationship for different lithologies showing the special location of salt in the density-velocity plot (after Gardner et al., 1974). Solid lines show the range of velocity-density change of each lithology; numbered dashed lines are constant acoustic impedance.

The question of whether salt layers in the subsurface may be anisotropic or not is a controversial one. Geologically, as seawater evaporates, the concentration of the carbonates, sulphates and chlorides increases to the point where one or more salts will precipitate. The depositional sequence of evaporites is that calcite and gypsum are the first salts to precipitate, followed by halite and sylvite. Under subsurface conditions, gypsum is converted to anhydrite due to increased pressure and temperature. This sequence is very common in the Devonian of western Canada where salt (halite and sylvite) is usually associated with anhydrite. Salt crystals grow in certain trends where salt was originally deposited in a stable environments. Different types of salt represent different original depositional environment and diagenesis histories. Chevron-salt represents a stable environment. The thicker and purer the chevron-salt unit stratigraphically, the more stable the environment of deposition was. Chevron-salt is quite common in western Canadian

Devonian units (e.g., the Whitkow Member of the Prairie Evaporite Formation, (Meijer Drees, 1986). Crystal lattices in recrystallized salt can be rearranged in a certain way due to the paleogeothermal gradient and pressure in the region.

Salt textures have been documented. Skrotzki and Welch (1983) studied the relation between salt texture and temperature and concluded that the preferred orientation developed in extruded salt is a function of extrusion temperature. Also the connections with the diapirism of salt domes were discussed. Larsen (1983) did a textural analysis and crystallographic orientation study of a salt dome. Spencer and Lowenstein (1990) systematically analyzed diagenesis and geological process of different types of salt and textural features. Those types of salt that have preferred crystal orientation exist widely.

In order to understand what types of salt are anisotropic, the features of salt anisotropy, and how the anisotropy can be observed, I first did a classification of salts. Then I carried out a physical modelling study and an investigation that included microscope study of salt texture correlated with laboratory velocity measurement. Theoretical derivation of phase and group velocity for cubic symmetry has been completed. Group velocities versus ray angle have been observed and fit well with theoretical calculations for salt samples with chevron crystals from the Whitkow Member of the Prairie Evaporite Formation in the western Canada basin. The experimental study has been done on 17 salt samples which were collected from different areas in Alberta, Canada. From some ultrasonic laboratory experiments ($f \sim 10^5$ - 10^6 Hz), I have found some types of salt to exhibit shear-wave splitting (Sun et al., 1991).

Because salt crystals (halite, sylvite, etc.) have cubic symmetry and are therefore elastically anisotropic, we have been considering the possibility of using the diagnostic properties of this seismic anisotropy (such as shear-wave splitting) as an additional tool for mapping salt, in combination with the traditional well-logging tools – mainly caliper and gamma-ray logs. In order that salt units exhibit such diagnostic properties for frequencies of relevance to exploration ($f \sim 10$ - 10^2 Hz), salt crystals would have to be aligned

throughout certain volume of salt layer. The objective of the field 3-component study (Chapter 5) is to see whether in-situ salt might exhibit observable seismic anisotropy in the so-called high-resolution frequency range ($f \sim 10^3$ Hz), closer to that of exploration.

1.2 Thesis objectives and structure

This thesis is concerned with seismic anisotropy of salt for the purpose of mapping salt in a new way. Salt anisotropy study is not only meaningful in seismic theory but also important in practice such as separating salt remnants from reefs on seismic sections and the possibility of exploiting these properties, e.g. directional dependence of salt structure migration etc. After salts were classified into different types in terms of possible seismic anisotropy, the laboratory velocity measurements on different types of salt were implemented (Chapter 2). The phase and group velocity formulae for cubic symmetry were elaborated, which provide a theoretical prediction of phase and group velocity for cubic symmetry (Chapter 3). Much evidence of salt anisotropy was collected through physical modelling, and the results fit the theoretical prediction (Chapter 4). The field 3-component study (Chapter 5) was carried out and it was found that the recrystallized and thermomechanically altered salt studied in this experiment appears to exhibit observable seismic anisotropy in the so-called high-resolution frequency range ($f \sim 10^3$ Hz), closer to that of exploration. The symmetry axes of the anisotropy appear to be consistent with a cause rooted in the alignment of salt crystals.

1.3 Data sets used in thesis

The following datasets were created and used while the salt seismic anisotropy study was pursued through theoretical study, modelling, and 3-component experiments in a potash mine.

1.3.1 Core laboratory velocity data

The data for all the plots of compressional and shear velocity versus pressure and temperature shown in Chapter 2 were measured at Core Laboratories Division of Western Atlas Canada Ltd. using ultrasonic instruments on different types of salt samples which were from the Core Research Centre of the Energy Resources Conservation Board (ERCB).

1.3.2 Modelling datasets

(1) The physical modelling data set shown in Chapter 4 was created in the elastic and acoustic modelling laboratory at The University of Calgary. Different types of salt samples were used as modelling materials.

For zero-offset transmission modelling with azimuthal rotation of the sample, the shear source and receiver transducers were oriented with the same polarization. For source-receiver offset transmission experiments source and receiver were polarized both in the same direction and perpendicular to each other. A similar source-receiver setup was used for the transmission experiments around a chevron-salt sphere. Further descriptions are given in Chapter 4.

A table of salt anisotropy parameters (Chapter 3) was deduced using velocity data measured from a large pure salt crystal in the same laboratory.

(2) The numerical synthetic data set shown in Chapter 4 was created by the program coded by Sean Guest at Queen's University, Ontario, Canada.

1.3.3 Three-component field experiments datasets

A three-component data set was recorded in the spring of 1993 using a hammer-impact source in the Allan Mine of the Potash Corporation of Saskatchewan, Saskatoon, Canada using acquisition parameters summarized in Table 5.1. The data were acquired in a high frequency range ($f \sim 10^3$ Hz). Normal, inline and crossline components were acquired by changing the geophone orientation. Detailed acquisition procedure is given in Chapter 5.

1.4 Hardware and software used

Salt velocity measurement under pressure and temperature was performed using the Core Laboratories Canada ultrasonic system. All the physical modelling was performed using the CREWES Project acoustic modelling system at The University of Calgary, Canada. Panametrics **V103** piezoelectric transducers were used for both P-wave sources and receivers. Panametrics **V153** piezoelectric transducers were used for both S-wave sources and receivers. Amplified modelling data were recorded using a Nicolet oscilloscope connected, through an IBM-XT, which controls the experiment, to a Perkin-Elmer 3240 seismic processing system for storage. The three-component experiment in Allan Mine of PCS was implemented using a 24-channel Bison GeoPro for data recording and storage. A hammer was employed as the energy source (frequencies from 100 to 2000 Hz), and high-frequency geophones were used for recording.

Programming was undertaken mostly on a SUN workstation through the UNIX operation system. Field recorded seismic data were converted to SEG-Y IBM format using the VISTA software package (Seismic Image Ltd). Some additional programming was undertaken on IBM PC 386. Some data processing work was done using the Inverse Theory and Applications (ITA) and ProMax processing packages, running on SUN workstations. The seismic displays were generated using a Versatec plotter attached to the

system. The thesis text was written on the Macintosh computer with Microsoft Word while the mathematical equations were generated using Expressionist. The figures and tables were created using graphics software such as Canvas, Cricket Graph, MacDraw, and Photoshop on Macintosh computers.

Chapter 2 - Salt classification and velocities measurement in laboratory

2.1 Introduction

In order to facilitate the description of the evaporitic deposits in a very simple way, Meijer Drees (1986) subdivided evaporitic deposits into two groups. Major evaporitic deposits are thick, extensive and include interbeds of halite. Minor evaporitic deposits are relatively thin, have a local distribution, and do not include salt beds.

Geologically, on the one hand, as seawater evaporates, the concentration of carbonates, sulphates and chlorides increases to the point where one or more salts will precipitate. The depositional sequence of evaporites is that calcite and gypsum are the first salts to precipitate, followed by halite and sylvite. This sequence can be seen in the Devonian of western Canada (Meijer Drees, 1986). Under subsurface conditions, gypsum is converted to anhydrite due to increased pressure and temperature. On the other hand, brine crystallization is more complex than ordinarily believed. It is influenced by a number of variables including brine concentration, temperature, solubility of the salts in the brine, and paleo-environmental factors such as energy, depth of water, bathymetry of the basin, and geomorphological characteristics of the adjacent land bodies. Additionally, salt layers in the subsurface afterwards undergo diagenesis.

In this chapter I present salt classification based on salt velocity features and seismic anisotropy. Under laboratory conditions some types of salt have been found to exhibit shear-wave splitting (Sun et al., 1991). By *salt* I mean primarily halite, NaCl; but sylvite (potash), KCl, often occurs together with halite and both have cubic symmetry. As a matter of fact, chevron salt is produced syndepositionally in a very stable environment and has a syntaxially grown crystalline framework consisting of vertically oriented and elongated crystals. The preferred orientation can be developed in extruded salt as a function of

extrusion temperature (Skrotzki and Welch, 1983). Schwerdtner (1966) also reported a preferred orientation found in halite rocks of Gulf Coast domes (U.S.A.).

In the process of seismic exploration, an understanding of seismic velocities in rocks plays a vital role in the success of seismic methods. The objectives of salt-velocity measurements in the laboratory are to observe the changing pattern of V_P/V_S and elastic velocity anisotropy, and to determine the degree of velocity contrast among different types of salt.

2.2 Salt classification

Geophysically, the criterion for classifying salts is to observe whether the different types of salt cause seismic waves to behave differently as they propagate through the salt units, with a view to observing any anisotropy. Geologically, these properties of salt depend on several factors such as: origin, composition, and the influence of diagenesis or burial metamorphism. The salt classification presented below is related to the velocity characteristics (properties) of salt.

Primarily, salt can be classified according to composition into two groups: pure, and impure salts. Impure salts are those in which salt crystals are mixed uniformly with clastic deposits (due to intrasedimentary growth of salt). Pure salt layers interbedded with non-salt thin layers (e.g., thin anhydrite layers) are considered as pure salt. If salt crystals are mixed uniformly with clastic deposits, the crystals are usually randomly oriented (Figure 2.1a). My laboratory results show that such salt is isotropic. According to the characterization of salt-crystal orientation and alignment, pure salt is classified into three types: chevron-crystal, detrital, and recrystallized or burial-metamorphic.

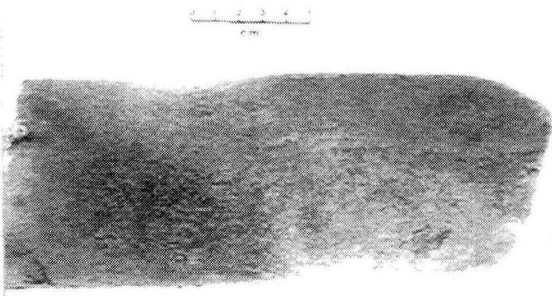
I: Chevron-crystal salt: this type of salt is produced syndepositionally in open spaces on the bottom of a brine body and has a syntaxially grown crystalline framework consisting of vertically oriented and vertically elongated crystals. This type of salt is

commonly preserved in modern and ancient evaporites. It represents a stable environment (e.g., an ephemeral lake-salt pan or permanent brine body). Gypsum is also reported with similar features (Schaller and Henderson, 1932; Lowenstein, 1982, 1988). Visually, the sample in Figure 2.1b and c shows white to colourless halite, with a 2-3 mm thick anhydrite lamination (c), cloudy or milky paths of vertically oriented, and equigranular (around 2 mm) crystals, crystallographic orientation is not observable. The experimental results show crystals are vertically oriented.

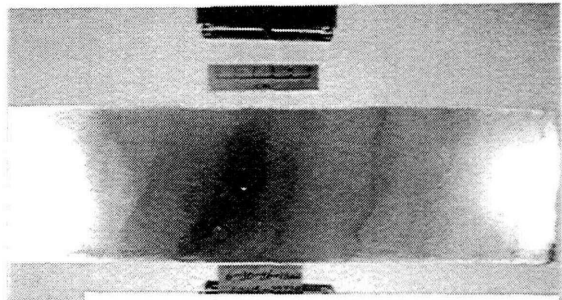
In geological processes, salt type I is layered and has a syntaxially grown crystalline framework consisting of vertically oriented and vertically elongated crystals. In essence, this fabric represents competitive crystal growth upward into a free-standing, saturated brine. Vertical orientation exhibits two forms: (1) vertically directed "chevrons" (syntaxial overgrowths on upward-facing cube coigns, Spencer and Lowenstein, 1990) and "cornets" (syntaxial overgrowths on upward-facing cube faces); (2) upward-coarsening and widening crystals.

Stratigraphically, a salt layer usually consists of many salt units interbedded with thin shale (mud), anhydrite or carbonate. This entails three different causes: (1) environmental change, whereby the concentration of evaporite changes to the point where gypsum or carbonate precipitates; (2) dissolution or erosional surfaces that truncate vertically oriented crystals and act as substrates for growth of a new crystalline layer; and (3) clastic deposits, such as clay, moved to the brine pools via certain channels (e.g. rivers) from outside a brine pool while salt crystals were growing. One typical example of this is in Qaidam Basin, China (Casas et al., 1992). There are two processes that produce this type of salt: (1) mechanical accumulations of cubes that precipitated in a water column and settled to the bottom of brine pool (Lowenstein and Hardie, 1985); and (2) frameworks of abraded crystals sorted by bottom currents (Weiler et al., 1974).

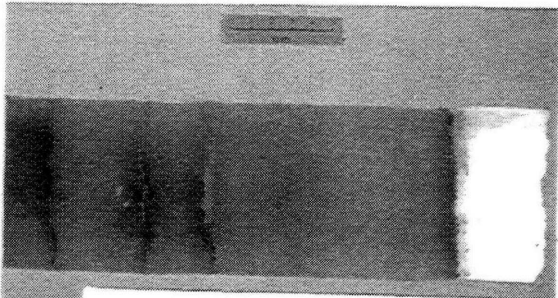
II. Detrital-framework salt: the framework of grains with point contacts establishes a primary detrital texture in evaporites which is produced in high-energy ephemeral



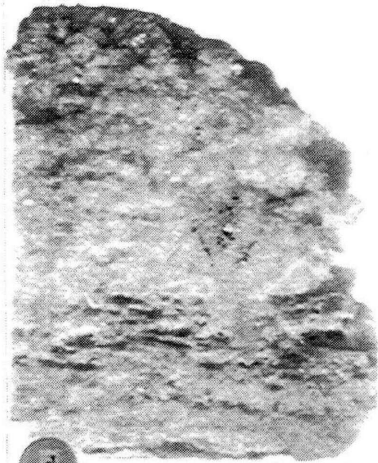
a well: 10-32-45-1W4
depth: 3440 - 3500 ft



b well: 6-30-86-13W4
depth: 2215 - 2272 ft



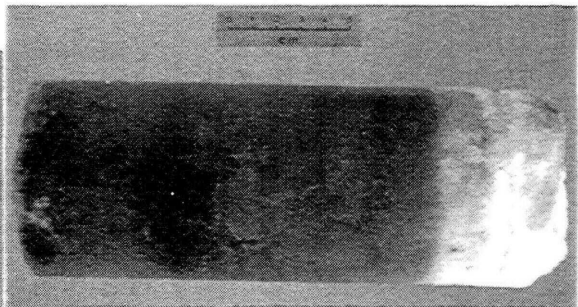
c well: 6-30-86-13W4
depth: 2215 - 2272 ft



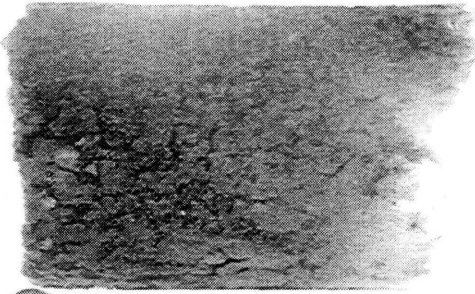
d modern deposit



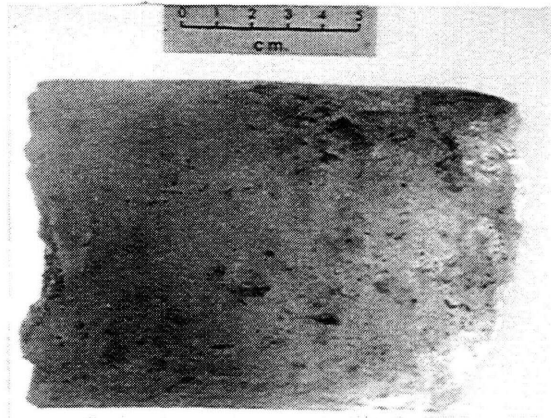
e well: 16-27-55-12W4
depth: 4454 - 4463 ft



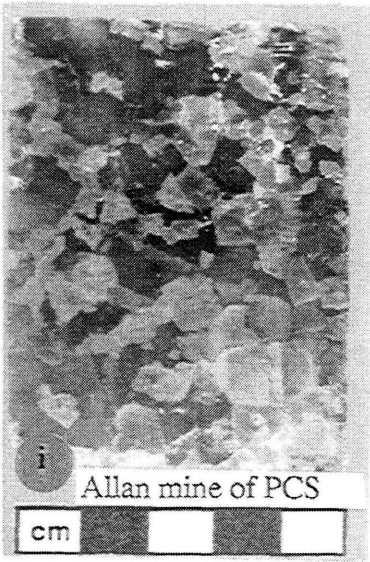
f well: 10-3-49-6W4
depth: 3764 - 3824 ft



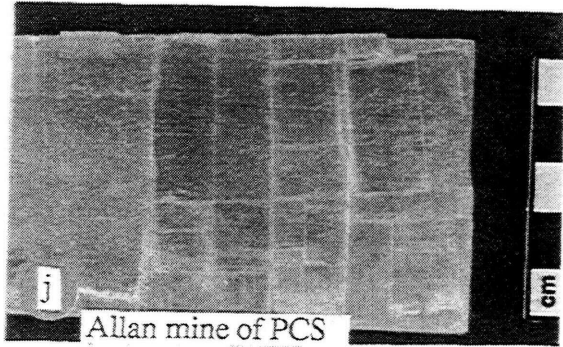
g well: 10-3-49-6W4
depth: 3764 - 3824 ft



h well: 10-32-45-1W4
depth: 3440 - 3500 ft



i Allan mine of PCS



j Allan mine of PCS

FIG. 2.1. Photographs of all type of salt samples

(a) Impure salt, fine crystalline halite, sylvite uniformly distributed with abundance of clay. The sample is from the depth range: 1048.5 - 1066.8 m in well: 10-32-45-1W4, Alberta, Canada, Leofnard Member, Devonian.

(b) and (c) Chevron-crystal salt, white to colourless halite, with 2 to 3-mm thick anhydrite lamination (c, converted from gypsum), cloudy or milky paths of vertically oriented, equigranular (around 2 mm) crystals, and crystallographic orientation is not observable, sample from depth range: 675.1-692.5 m, well: 6-30-86-13W4, Alberta, Canada; Whitkow Member, Prairie Formation, Devonian.

(d) Detrital-framework salt, tiny white (≤ 1 mm) halite crystals with point contacts establishes a primary detrital texture, mostly equigranular and euhedral crystals, with random crystallographic orientation, and high porosity; sample from modern deposit of Dabasun Lake, Qinghai, P.R.China.

(e) Recrystallized salt, large pure crystalline halite, brown clay fragments show up occasionally; transparent, same crystallographic orientation; sample from depth range: 1357.6 - 1360.3 m, well: 16-27-55-12W4, Alberta, Canada, Upper Lotsberg Salt, Devonian.

(f) Recrystallized salt, halite (size: 0.2-0.5 cm) with seasonal intrasediments clay (visually layered); crystallographic orientation is not observable, sample from depth range: 1147.3 - 1165.5 m, well: 10-3-49-6W4, Alberta, Canada, Leofnard Member, Prairie Formation, Devonian.

(g) Recrystallized salt, high content sylvite (≤ 0.5 cm) with minor halite, crystallographic orientation is not observable; sample from depth range: 1147.3 - 1165.5 m, well: 10-3-49-6W4, Alberta, Canada, Leofnard Member, Prairie Formation, Devonian.

(h) Recrystallized salt, pure fine crystalline halite with minor sylvite, crystallographic orientation is not observable; sample from depth range: 1048.5 - 1066.8 m, well: 10-32-45-1W4, Alberta, Canada; Leofnard Member, Prairie Formation, Devonian.

(i) Recrystallized salt, sylvite (darker) with minor halite (lighter) (crystal size: 0.2-1.0 cm) thermomechanically altered salt; sample from the Allan Mine of Potash Corporation of Saskatchewan, the Patience Lake Member, Prairie Formation, Devonian.

(j) Crystal-oriented salt, from dissolution-reprecipitation. It is transparent, one single crystal but perhaps an amalgamated crystal (same crystallographic orientation); sample from the Allan Mine of the Potash Corporation of Saskatchewan; the Patience Lake Member, Prairie Formation, Devonian. The scale of this salt block is about 5.0 meters in diameter.

environments as clastic rocks. The salt layer exhibits isotropic features. Figure 2.1d shows this type of salt with tiny white (≤ 1 mm) halite crystals, mostly equigranular, and euhedral crystals, with random crystallographic orientation, and high porosity.

III Recrystallized and burial metamorphic salt: This type of salt is diagenetically altered by subsurface conditions, and it could be anisotropic or isotropic. Salt in a salt dome fit into this texture. Its crystals may have a strongly preferred orientation (Skrotzki

and Welch, 1983; Larsen, 1983). It may also be strongly altered by temperatures and pressures due to burial in which case it is called anhedral mosaic salt.

Salt can have a strongly preferred crystal orientation due to recrystallization and metamorphism (Strotzki and Welch, 1983; Larsen, 1983). It also can be strongly altered by the temperatures and pressures due to burial where it may be called anhedral mosaic salt. The textures of these three types of salt are depicted in Figure 2.2.

The basic feature of anhedral mosaic salt is its polygonal mosaic texture that is a product of annealing recrystallization whereby grains "optimize" their size, shape and orientation to minimize the energy. Anhedral mosaic salt notably lacks vertical orientation; primary growth features have been destroyed. Instead, the anhedral mosaic consists of clear grains that meet at triple junctions that approach 120° angles in typical annealing-recrystallization polygonal-mosaic fashion. What the velocity characteristics are for this type of salt is still unclear. It is predicted that anhedral mosaic salt mostly exhibits isotropy. However, the recrystallization may be very patchy and the primary unaltered chevron halite could coexist with anhedral mosaic halite, which exhibits weak anisotropy.

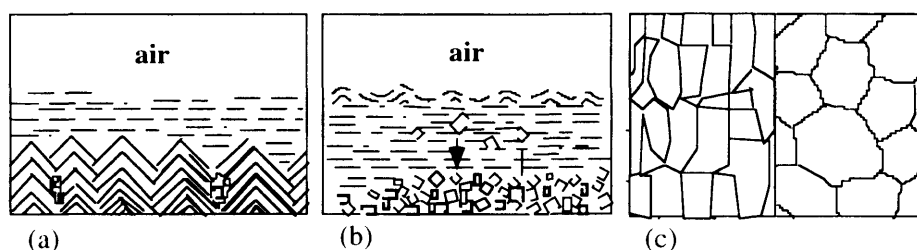


FIG. 2.2. Crystal framework of three major types of salt: (a) chevron-crystal, (b) detrital, (c) recrystallized, burial-metamorphic and anhedral mosaic (right panel) salt.

Recrystallization as applied to metamorphic salt refers to the reconstitution of an existing phase and controlled by pressure and temperature. It is a time-dependent process. The preferred orientation developed in extruded salt has been found as a function of extrusion temperature (Skrotzki and Welch, 1983). Two kinds of preferred orientations can

be developed in salt:

(1) Dimensional-preferred orientation: inequidimensional such as elongate, flaky or prismatic crystals have a tendency towards parallelism of one or more of the morphological axes.

(2) Lattice-preferred orientation: The crystal structures ('lattices') and hence optic directions and various crystallographic features (face, cleavage, etc.) have related orientations.

I use the North American crystal indices convention in this thesis. Square brackets [] denote uniaxial directions; and braces < > denote all similar directions in a crystal. Parentheses () denote a unique face; and curly brackets { } denote all similar faces of a crystal, e.g. the form of a crystal.

In most cases in salt, according to Strotzki and Welch (1983), the preferred orientations are lattice-preferred orientation. With increasing temperature a <100> fibre develops by recrystallization. When crystallization is suppressed by impurities, which happens often in natural rock salt, the deformation texture is more pronounced and the development of the <100> recrystallization fibre starts only at higher temperature.

Figure 2.3 shows the experimental results of Skrotzki and Welch (1983) which indicate that extrusion of NaCl polycrystals above room temperature leads to a <100> <111> double fibre texture. The [100] fibre intensity runs through a maximum at a certain temperature (T_0) where the [111] fibre has a minimum. This result indicates that a texture in salt domes will lead to anisotropic behavior under thermomechanical strain. For the experiment strongly resembled extrusion process, the results suggest that a double fibre texture near <100> and <111> in salt domes is in the vertical direction, i.e., in direction of flow.

One other case is that salt that is produced from dissolution-reprecipitation usually has a lattice-preferred orientation. It is, however, small scale compared with that of burial-metamorphic recrystallization. In this case an initial floodwater causes extensive tubular

networks of vertical and horizontal dissolution cavities. Subsequent evaporative concentration of the flood water results in halite-saturated brines and renewed crystal growth. Figure 2.1e consists of oriented salt crystals, or a single crystal or perhaps amalgamated crystal (same crystallographic orientation). Also, of course, it has strong preferred orientation. It is produced from dissolution-precipitation in the subsurface. Salt classification is summarized in Table 2.1.

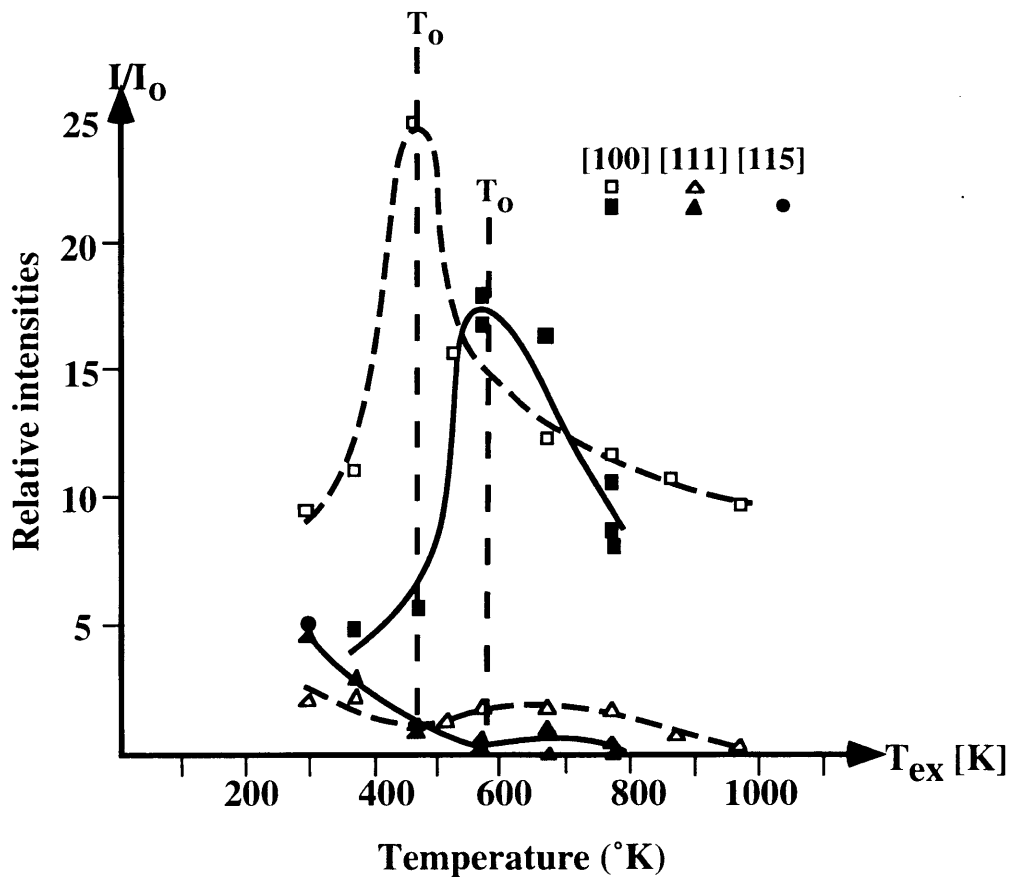


FIG. 2.3. Temperature (T_{ex}) dependence of the intensities of the preferred fibres in extruded synthetic salt (dashed curves, open symbols) and natural salt (solid curves, filled symbols). Intensities are given in units of a random orientation distribution I_0 (modified after Skrotzki and Welch, 1983).

Table 2.1. Salt classification and velocity features

type	pure salt			impure salt
	I	II	III	
subtype				
name	chevron-crystal salt	detrital-framework salt	recrystallized, metamorphic salt	
features	<ul style="list-style-type: none"> ● syndepositional ● vertically oriented and elongated and vertically directed "chevrons" ● vertically oriented and elongated, upward-facing cubes (flat-topped) 	<ul style="list-style-type: none"> ● mechanical accumulations of cubes ● frameworks of abraded crystals sorted by bottom currents ● salt crystals randomly oriented 	<ul style="list-style-type: none"> strongly perferred crystal orientation when strained thermomechanically lack of vertical orientation, anhedral mosaic crystals 	salt crystals uniformly mixed with clastic deposits
velocity property	anisotropic	isotropic	anisotropic	isotropic
occurrence	normal salt units	normal salt units	normal salt units, salt domes, salt plugs	normal salt
environment	ephemeral lake-salt pan permanent brine body	permanent brine body or high-energy ephemeral system	reprecipitation diagenetic alteration of salt	intrasediment growth of salt

2.3. Laboratory measurement of compressional- and shear-wave velocities

As discussed above, salts are classified as various types that may have different attributes of velocity as they are different with respect to the origins of evaporites, the influence of diagenesis, or burial metamorphism. Velocity always is a very important parameter in seismology. In multicomponent seismic studies, V_P/V_S is an useful indicator of lithology. It was reported that the Beaverhill Lake salt has a VSP-determined V_P/V_S 1.97 (Geis et al., 1989) which was recommended as a diagnostic to distinguish salt from other lithologies. In fact our measurements show that V_P/V_S varies as the salt type changes. Laboratory velocity measurements were made on many salt samples with P- and S-wave ultrasonic transducers, simulate in-situ conditions, in which pressure and temperature effects were considered.

2.3.1. Experimental apparatus and procedure

Figure 2.4 shows the schematic diagram of the experimental apparatus. An ultrasonic pulse-transmission method was employed in the experiments. Overburden pressure (P_C) and pore pressure (P_P) can be controlled separately. However, with the exception of detrital-framework salt, most salt samples are considered as non-pore rock. Therefore, neither a pore-pressure controller nor a back-pressure controller were used during the experiments. A pump with a step motor-drive controls overburden pressure. A thermometer (T) was employed to control the temperature of the sample inside the pressure vessel. A heater in the pressure vessel was used to increase the temperature. The transmitting and receiving transducers consist of both compressional (P) and shear (S) piezoelectric crystals of 500 kHz. A P-wave transducer is located in the centre while 8 S-wave transducers are displayed in a circle around the P-wave transducer, by which means

the quasi-S₁ (faster quasi-shear wave) may be received progressively earlier. The transmitting transducer converts the ultrasonic pulse generated by the pulse generator (Figure 2.3.1.1) to elastic waves. The receiving transducer, identical to the transmitting transducer, converts the elastic wave traveling through the rock sample back to electrical signals. The received waveforms are displayed and digitized by an oscilloscope and then stored for further processing and traveltime analysis using a microcomputer.

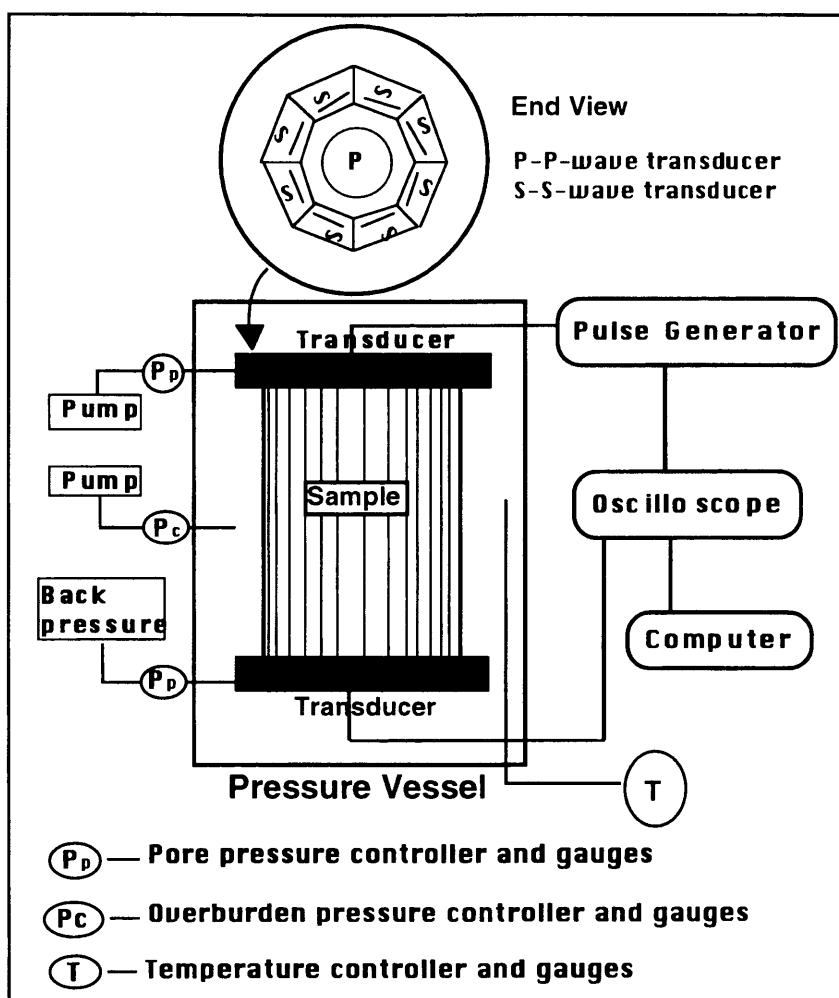


FIG. 2.4. Schematic diagram of the acoustic measurement system.

The waveforms stored in the computer can be retrieved and amplified (in both horizontal and vertical directions) so that accurate traveltimes can be picked. The velocities were calculated using the measured core sample length and picked traveltimes. The total uncertainty in the calculated velocities is estimated to be less than $\pm 1\%$ (Wang et al.,

1991).

The rock salt samples were cut flat on both ends. Each sample had a diameter of 8.8 cm whereas the lengths of samples ranged from 10 to 28 cm. Both recrystallized and detrital-framework salts were measured but the chevron-crystal salt could not be tested because the samples, due to previous cutting, were not round.

The sample was jacketed in a high-pressure and high-temperature plastic sleeve then loaded into a hydrostatic pressure vessel. Overburden pressure was increased to 6000 psi for most samples and then lowered to 0 psi. Then the rock sample was heated and for temperatures from 21.9°C to 139.3°C, velocities were measured to determine the temperature effects. Also one heated sample was used to measure the velocities versus both overburden pressure and temperature.

2.3.2. Experimental results

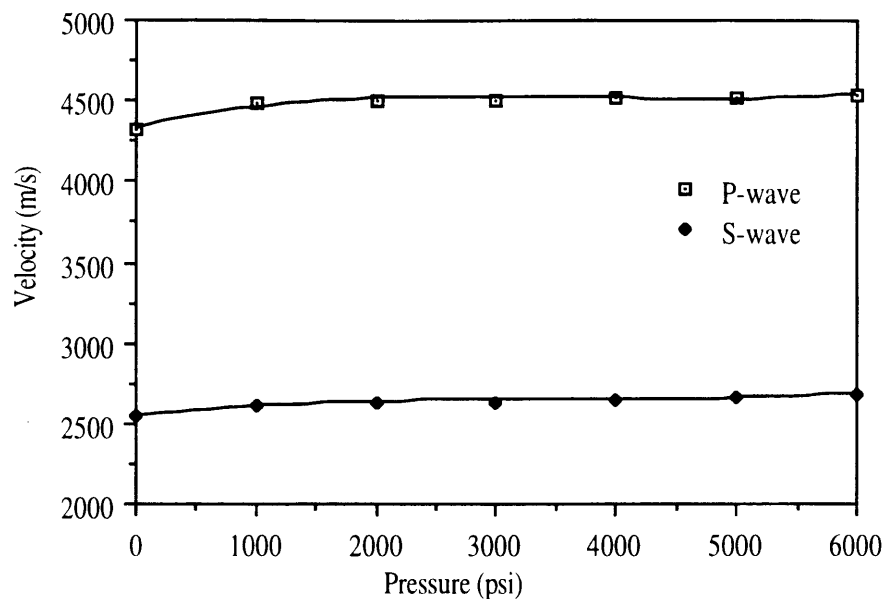
In this velocity measurement, various samples of recrystallized salt and detrital-framework salt have been tested. Chevron-crystal salt could not be jacketed in the high-pressure, high-temperature plastic sleeve due to previous cutting.

In general, apart from the detrital-framework salt, the velocities (both P-wave and S-wave) do not change dramatically as pressure or temperature varies. If salt is not pure halite, V_P/V_S versus pressure or temperature shows two different characteristics: first V_P/V_S increases and gradually drops after 1000 psi or 1500 psi, which indicates a greater increase of compressional-wave velocity than shear-wave, followed by the opposite. In pure halite (no matter whether it has dissolution cavities or not and no matter what the crystal size) V_P/V_S declines as pressure increases, indicating that shear-wave velocity increases relatively more rapidly than the P-wave velocity. Following analyses are based on laboratory tests attached in Appendix C for samples B, C and E).

2.3.2.1 Pressure effects

Figure 2.5 shows, as an example, the velocities and V_P/V_S versus effective pressure in an impure salt sample from the Leofnard Member, Devonian (sample D, Well: 10-32-45-1W4 Alberta, Canada, depth range: 1048.5 - 1066.8 m) which is fine crystalline

(a)



(b)

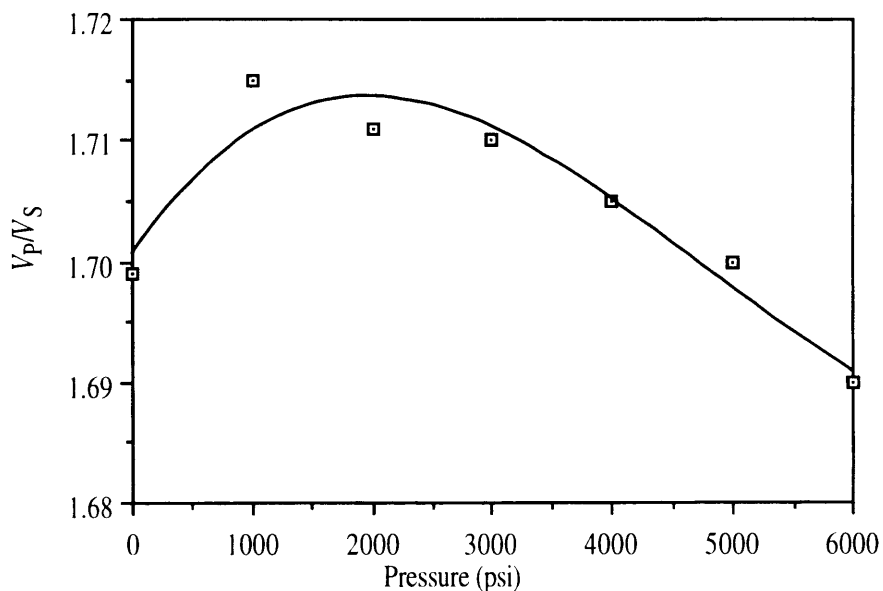


FIG. 2.5. (a) Compressional (V_P) and shear (V_S) velocities and (b) V_P/V_S ratio, versus pressure in an impure salt sample (D).

halite with sylvite uniformly distributed and plenty of clay. As will be discussed in Chapter 4, impure salt exhibits isotropic features. That is, there is only one shear-wave velocity: the one plotted in figure 2.5a. It is indicated in the plot that both compressional (V_P) and shear (V_S) velocities do not increase significantly as the overburden pressure increases. The V_P/V_S ratio increases up to 1 kpsi and gradually drops thereafter. Figure 2.5b, the plot of V_P/V_S ratio versus pressure, can be separated into two parts: below 1 kpsi, the V_S increases slightly but less relative to V_P . Above 1 kpsi V_S increases more rapidly than V_P . This can be seen from the plot of V_P/V_S versus pressure (Figure 2.5b). The V_P/V_S ratios determined range from 1.70 to 1.75. A similar result can be found in the sample of halite with abundant sylvite (see Figure 2.6) from the Leofnard Member, Devonian (well: 10-3-49-1W4, depth range: 3764 - 3824 ft, Alberta, Canada). The V_P/V_S ranges from ~ 1.60 to ~ 1.76 .

However, the pattern of velocity and V_P/V_S of pure halite is different. Even though recrystallized salt visually can be very different as formation history and diagenesis are different, as will be discussed below, experiment results have shown that all pure recrystallized halites have the same plot pattern of V_P/V_S versus overburden pressure, whereas a mixture of halite with sylvite or clay shows a different pattern.

A large pure crystalline halite (crystal size: 3-4 cm) with only occasionally shows of small brown clay fragments was selected for an overburden pressure test (sample G) . In Figure 2.7, even though both compressional and shear velocities do not change significantly as the overburden pressure increases, they increase smoothly. The faster shear-wave velocity V_{S1} increases greater than V_P . It is important to notice that the pattern of V_P/V_S versus pressure is different from the previous case. Both plots of V_P/V_S versus pressure and velocity slope (refer to Appendix C) indicate that shear velocity increases more rapidly as pressure increases than does compressional velocity.

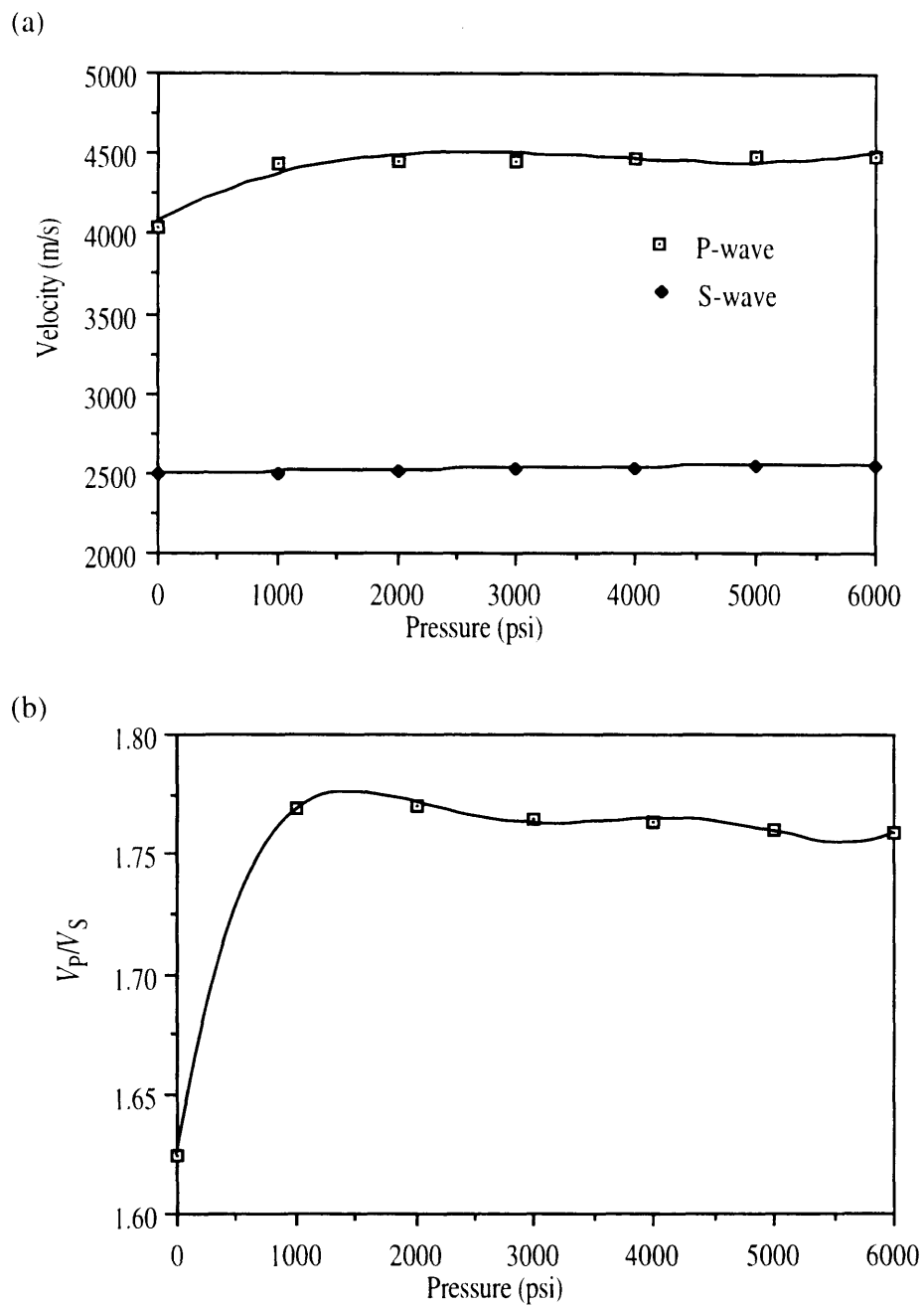


FIG. 2.6. (a) Compressional (V_p) and shear (V_s) velocities and (b) V_p/V_s ratio, versus pressure in a salt sample (A) composed of halite and sylvite .

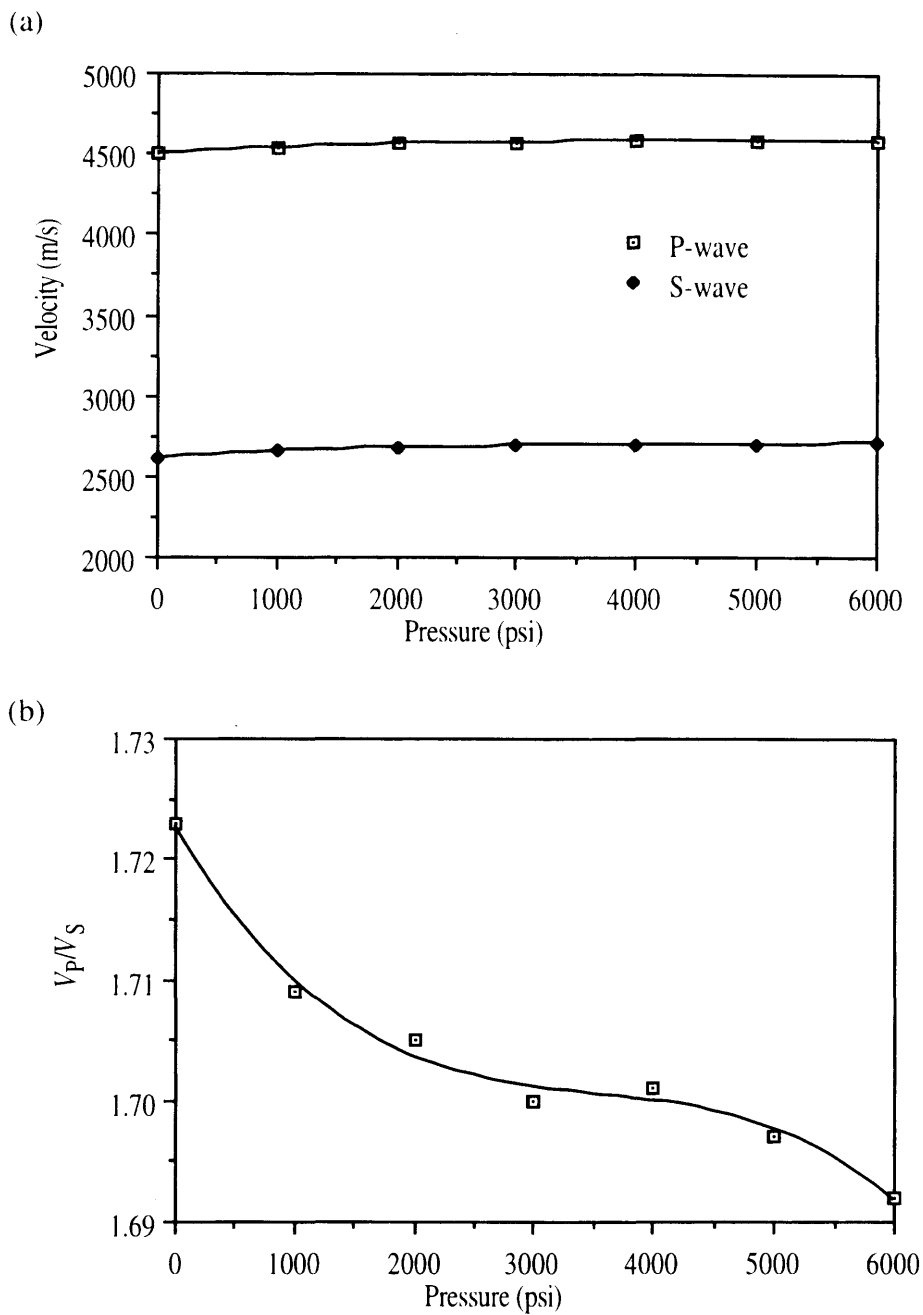


FIG. 2.7. (a) Compressional (V_P) and shear (V_S) velocities and (b) V_P/V_S ratio, versus pressure in a large pure recrystallized halite sample (G).

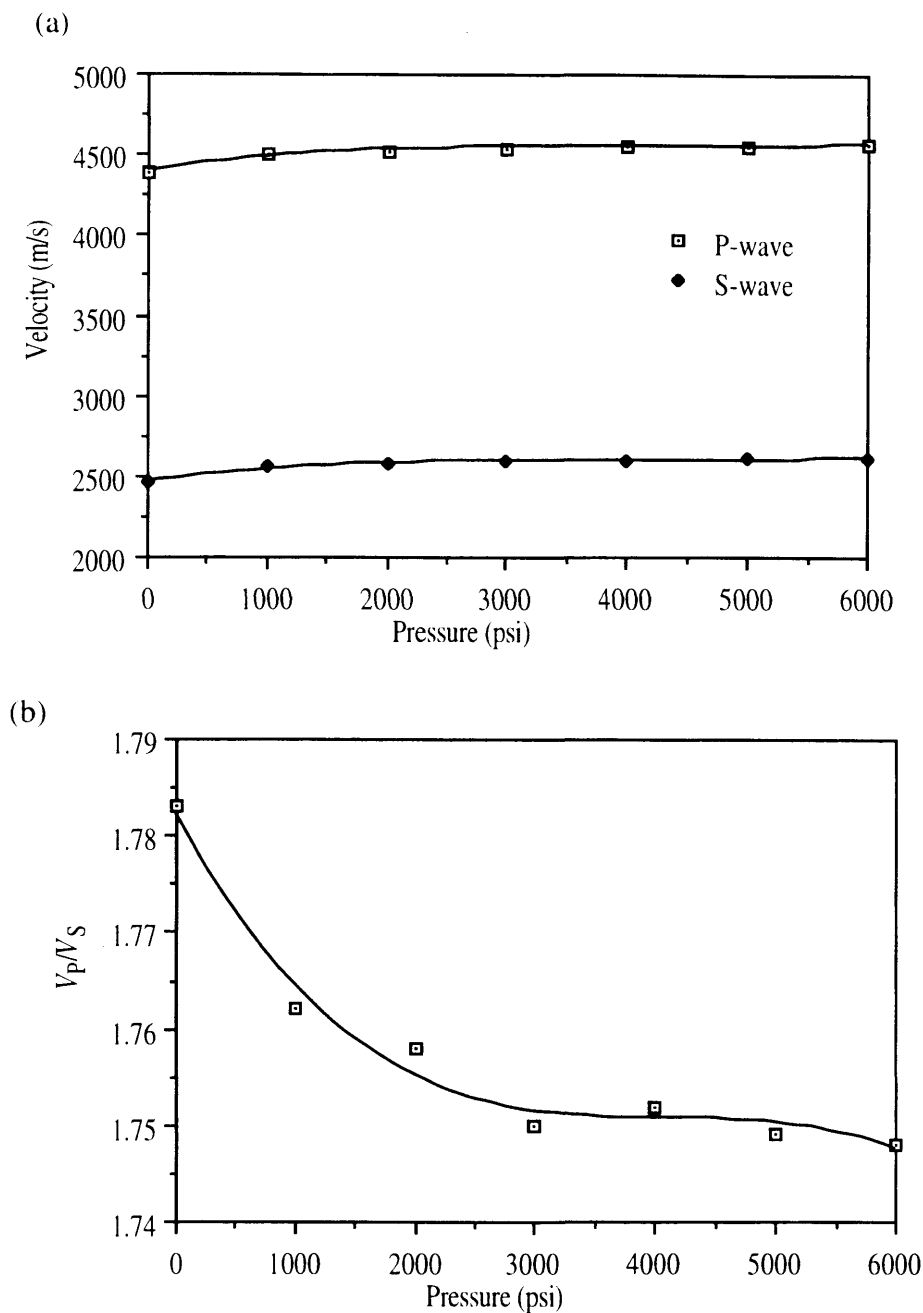


FIG. 2.8. (a) Compressional (V_P) and shear (V_S) velocities and (b) V_P/V_S ratio, versus pressure in a recrystallized pure halite sample (C) with dissolution cavities .

A similar result has been found in sample C which is a pure recrystallized halite (crystal size: 0.5–1.5 cm) with dissolution cavities (see Figure 2.8). Another recrystallized pure halite sample was visually layered due to seasonal environmental change.

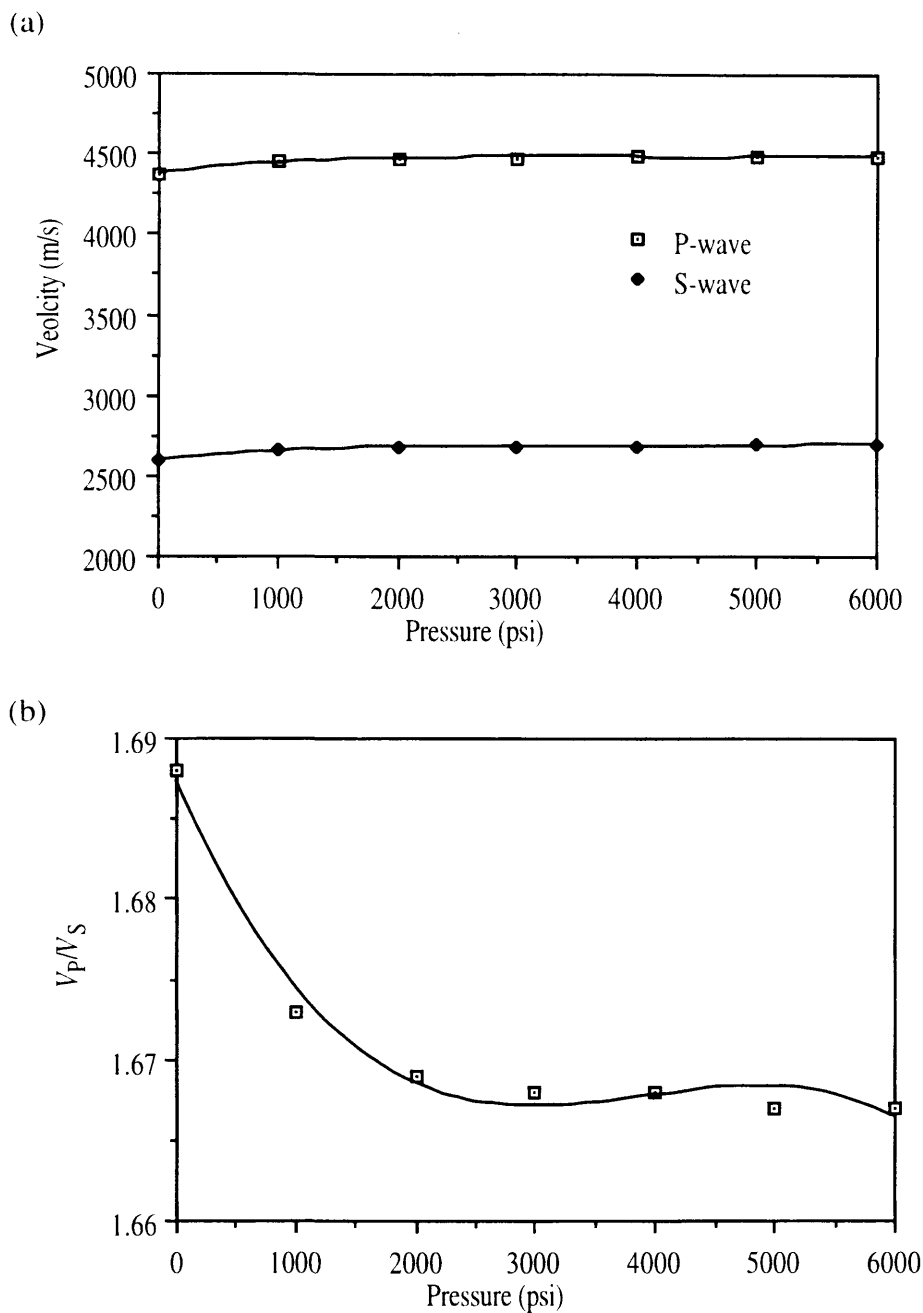
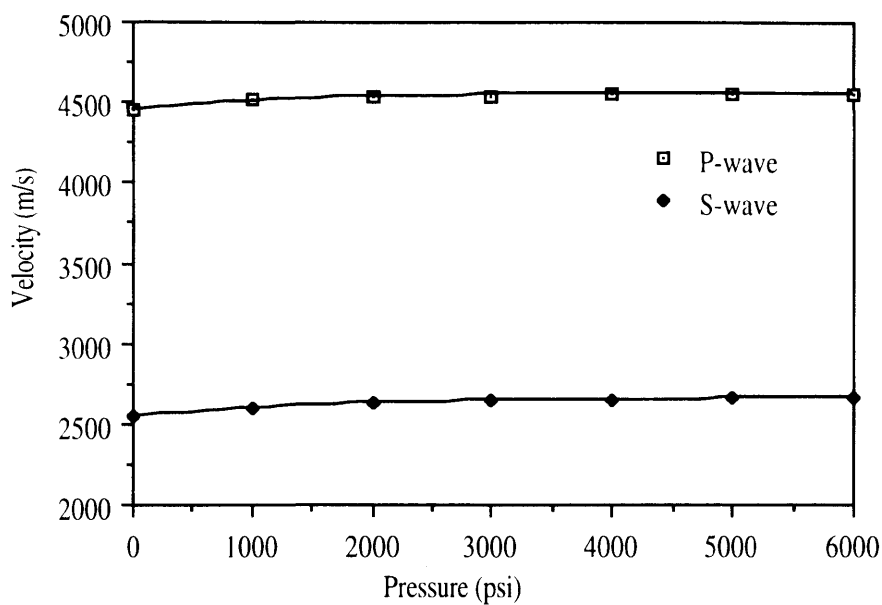


FIG. 2.9. (a) Compressional (V_P) and shear (V_S) velocities and (b) V_P/V_S , versus pressure in a visually layered recrystallized pure halite sample (E).

Still, the pattern of V_P/V_S versus pressure is very close to that of the previous pure halite examples (E) (Figure 2.9 and Figure 2.10). The only difference is that the peak at pressure of 4 kpsi has been truncated. Figure 2.11. shows the pattern of change in the velocity and V_P/V_S in a detrital-framework salt sample (a similar sample to previous pores in the

sample shown in Figure 2.1d) which is pure halite. As predicted, V_P/V_S dramatically increases when pressure increases, but the curve of V_P/V_S shows the same pattern as previous pure halite samples.

(a)



(b)

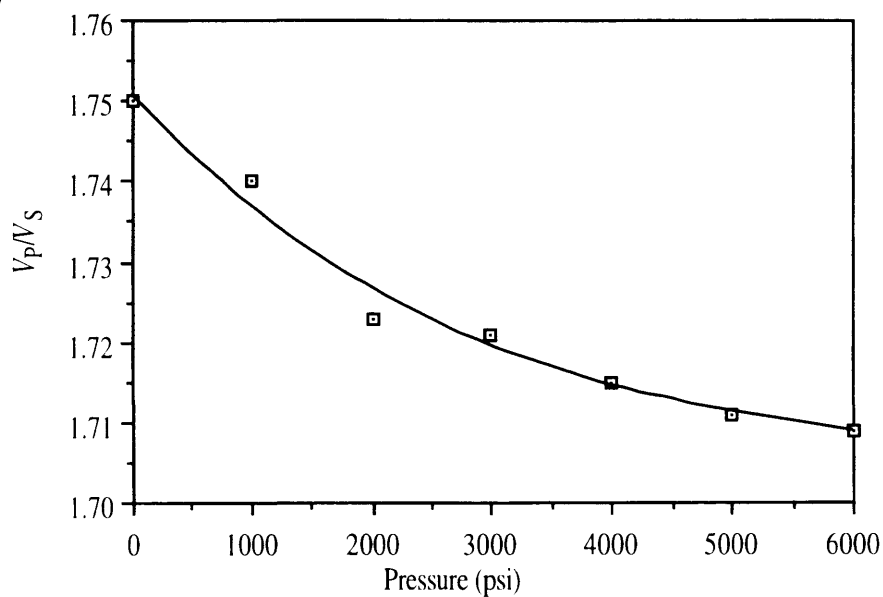
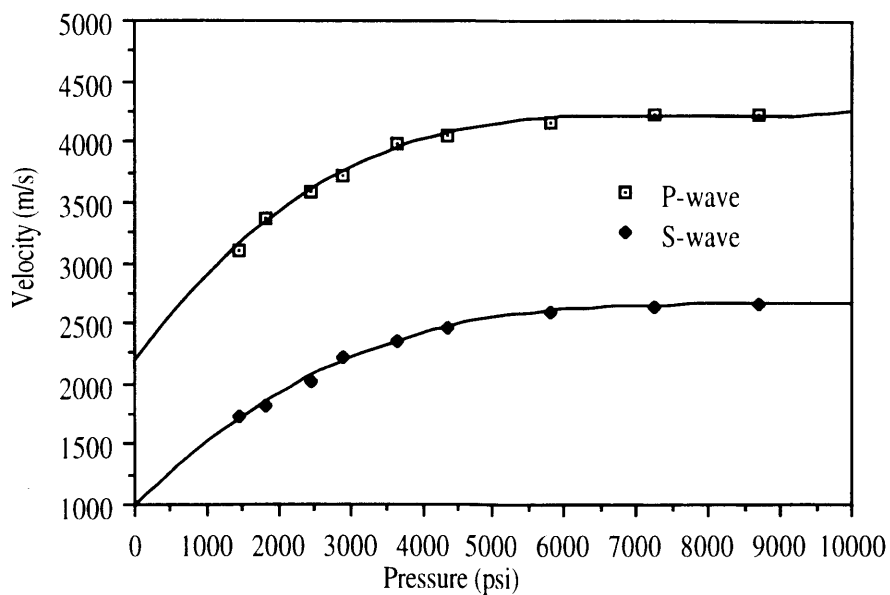


FIG. 2.10. Compressional (V_P) and shear (V_S) velocities (a) and V_P/V_S versus pressure in pure very large halite crystal with minor clay fragment inclusions.

This fact indicates that for recrystallized salt, the salt components are the dominant factor that affects velocities and V_P/V_S . The diagenesis (e.g., salt dissolution) only changes the value of V_P or V_S , but does not change the pattern of V_P/V_S versus pressure.

(a)



(b)

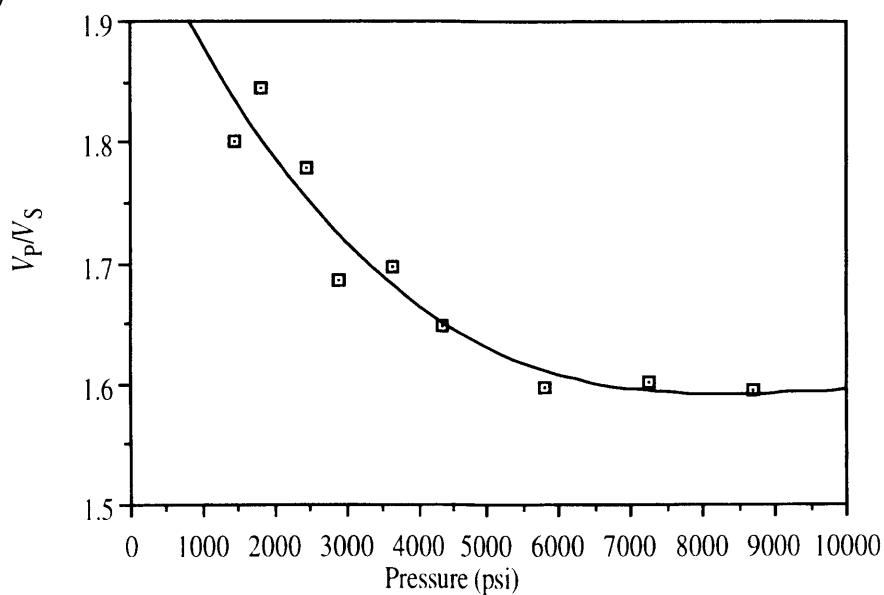


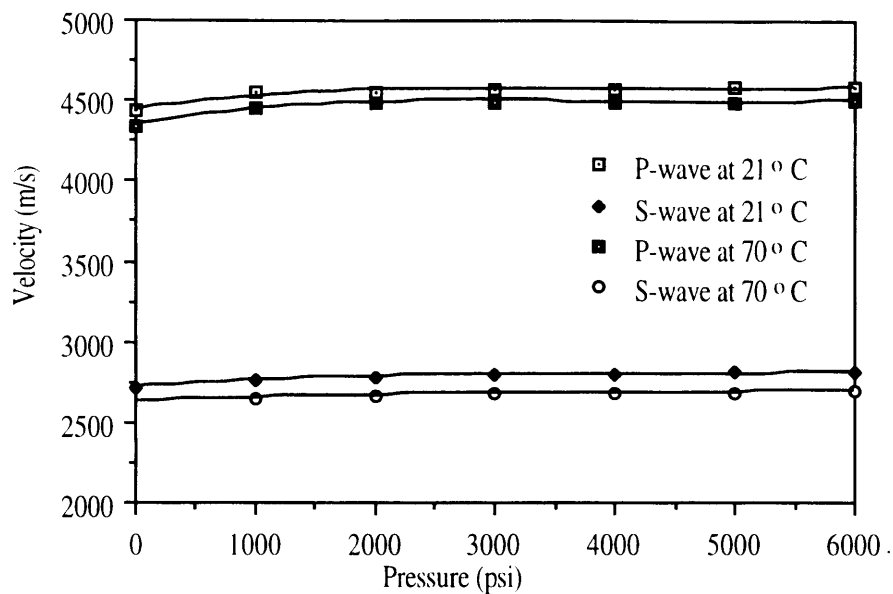
FIG. 2.11. (a) Compressional (V_P) and shear (V_S) velocities and (b) V_P/V_S , versus pressure in pure halite of detrital-framework salt.

2.3.2.2 Temperature effects

As discussed above, velocity of salt always increases with increasing pressure. Figures 2.12a, 2.13a and 2.14a show that the velocities decrease with increasing temperature. The V_P/V_S ratio increases with increasing temperature from 21° to 70°C (Figure 2.12b). This means that, compared with V_P , V_S decreases relatively more rapidly with increasing temperature in a recrystallized salt sample composed of fine crystalline halite with minor sylvite under the same pressure.

The V_P/V_S versus temperature curve (Figure 2.12b) shows similar patterns to those of the V_P/V_S versus pressure curve (Figure 2.13b). A sample composed of halite and minor sylvite was tested and the result plotted in Figure 2.13. A pure halite sample was also tested with increasing temperature (Figure 2.14). The V_P/V_S ratio declines as temperature increases, which indicates that V_P decreases relatively more rapidly with increasing temperature.

(a)



(b)

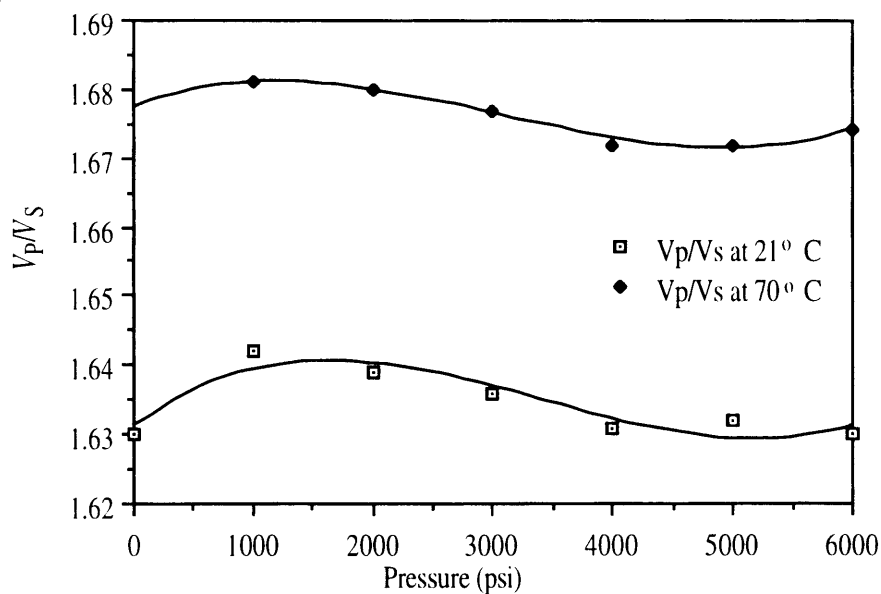


FIG. 2.12. (a) Compressional (V_p) and shear (V_s) velocities and (b) V_p/V_s , versus temperature and pressure in a salt sample composed of fine crystalline halite and minor sylvite.

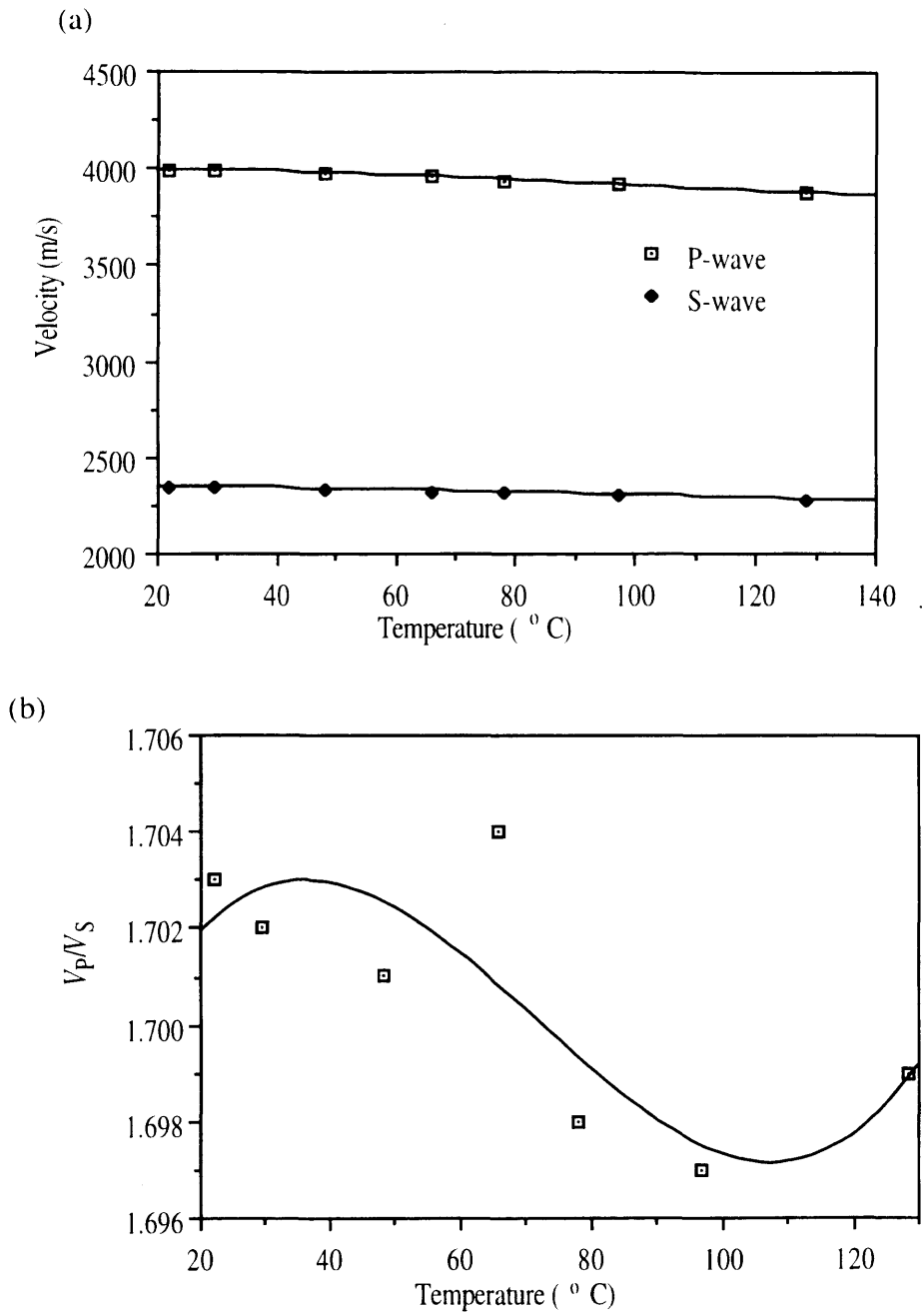
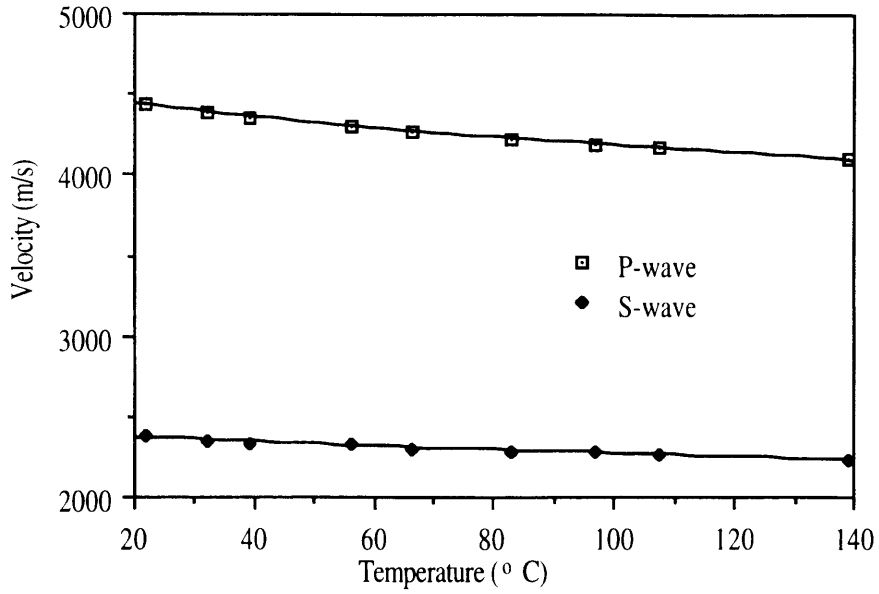


FIG. 2.13. (a) Compressional (V_p) and shear (V_s) velocities and (b) V_p/V_s ratio versus temperature in a salt sample composed of halite with sylvite.

a)



b)

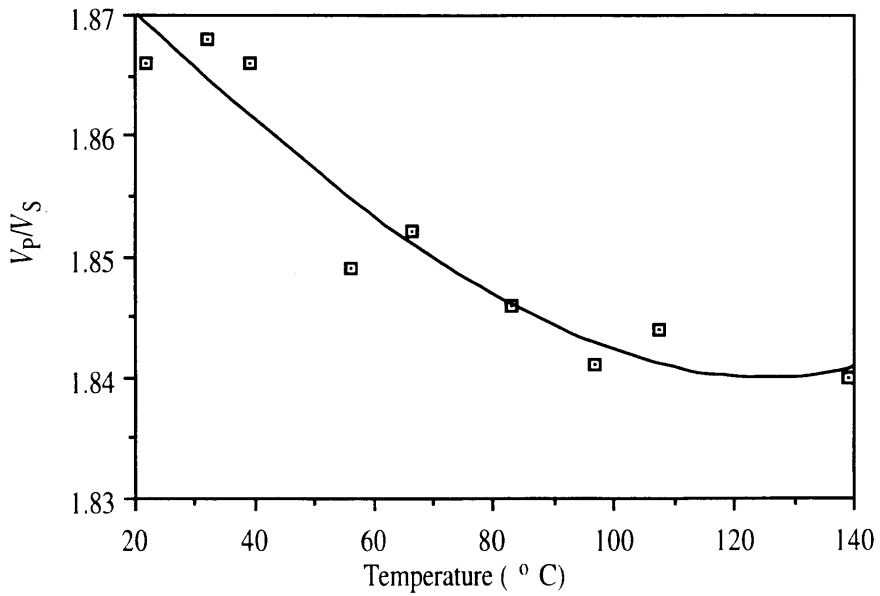


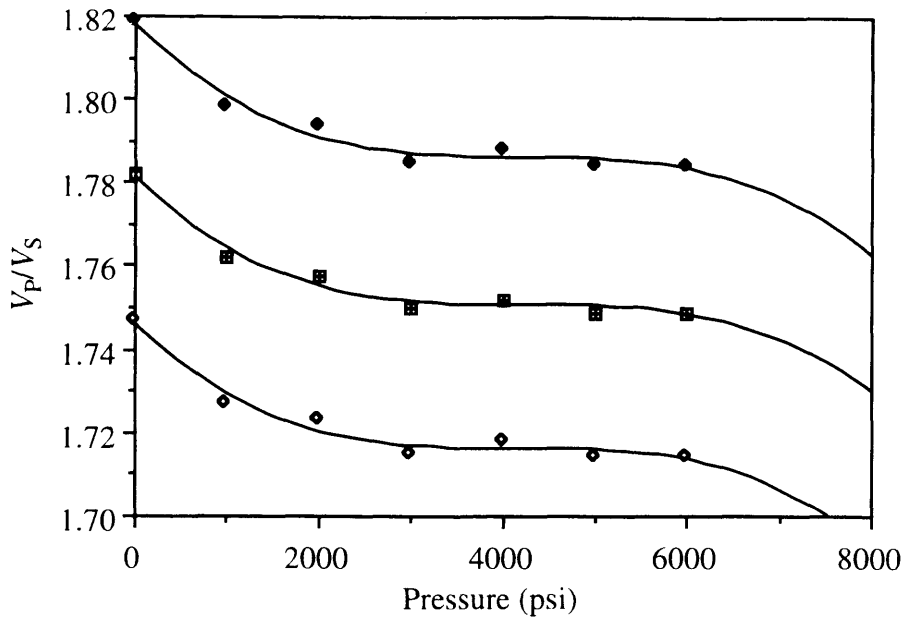
FIG. 2.14. (a) Compressional (V_p) and shear (V_s) velocities and (b) V_p/V_s ratio, versus temperature in a pure halite sample.

2.3.2.3 Sensitivity analysis of V_P/V_S pattern

Though the V_P/V_S pattern difference between pure and impure salt were examined through different samples, the sensitivity of these patterns is subject to the accuracy of velocity measurement. In the velocity measurement, errors might arise from uncertainties in picking the first arrival time of the waves, measuring the sample length, and controlling temperatures and pressures. Both compressional- and shear-wave arrivals are very sharp in the salt because of low attenuation. The end-surfaces were finely polished to parallel during sample preparation. The total error in the velocity values was estimated in the salt velocity measurement to be very similar to that of Wang et al. (1991), i.e. about $\pm 1\%$.

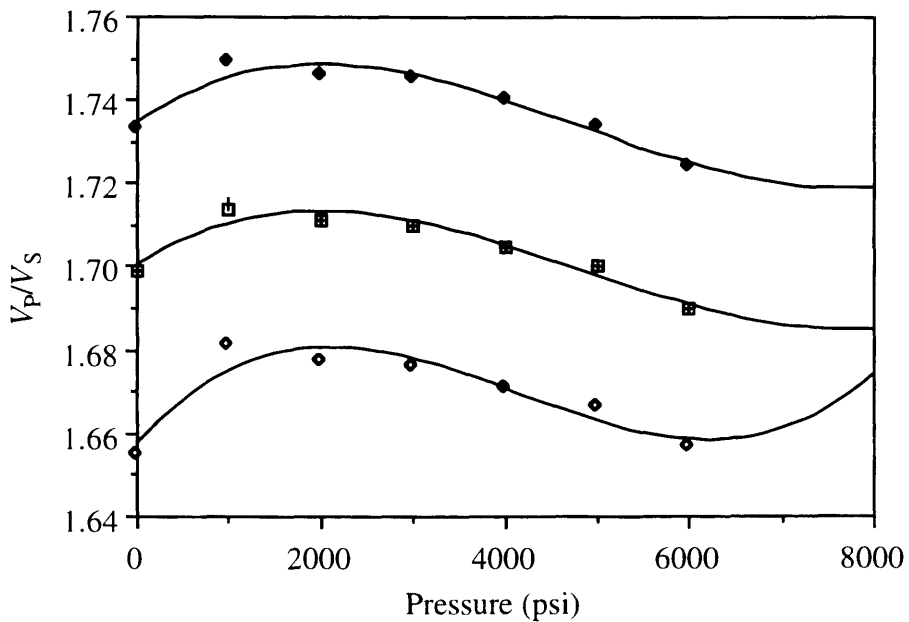
First, P-wave velocity is increased 1% whereas S-wave velocity is decreased 1% ; and second, P-wave velocity is decreased 1% whereas S-wave velocity is increased 1%. The third-order polynomial regression has been applied to the data of V_P/V_S versus pressure or temperature in two different ways so that the sensitivity of V_P/V_S pattern can be seen. The polynomial regression is first applied to the V_P/V_S data described above, then applied to the data for the two cases with error.

In general, the trends of the V_P/V_S patterns versus pressure or temperature for both pure and impure salts are similar to the previous results (see Figure 2.15, 2.16, 2.17, and 2.18 and compare with Figure 2.8b, 2.5b, 2.11b, and 2.14b). The estimated V_P/V_S error can be approximately ± 0.04 in maximum due to 1% total error of velocity measurement. In the case of P- and S-wave velocities are both increased or decreased 1% in value the V_P/V_S curves (see the middle curves in Figure 2.15a, 2.16a, 2.17a, and 2.18a) are the same and almost identical to corresponding V_P/V_S curves without adding velocity error (Figure 2.8b, 2.5b, 2.11b, and 2.14b), which indicates that a systematic error does not make V_P/V_S pattern recognition of pure and impure salts fail. However, if the random error is significant, the V_P/V_S pattern recognition can be failed. These conclusions do not apply to detrital-framework salt as it can be seen in Figure 2.17 due to wider change of velocity as pressure increases.



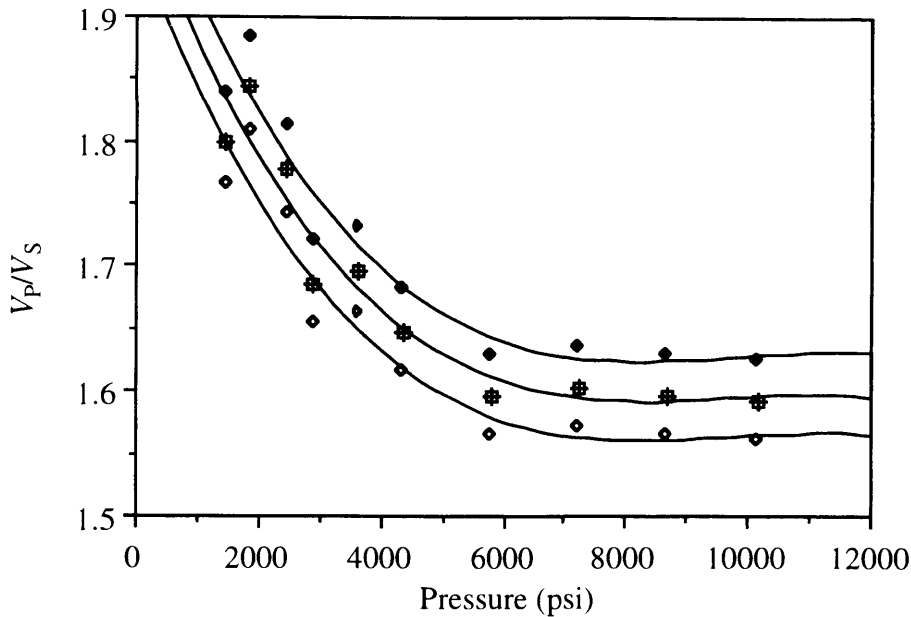
- ▣ both P- and S- velocity increased 1%; + both P- and S-velocity decreased 1%
- ◆ P-velocity increased 1% and S-velocity decreased 1%
- ◊ S-velocity increased 1% and P-velocity decreased 1%

FIG. 2.15. Pressure V_p/V_s pattern sensitivity analysis for pure halite (sample C, with dissolution cavities, compare with Figure 2.8b). Polynomial regression (3rd order) was applied to each individual case as denoted therein.



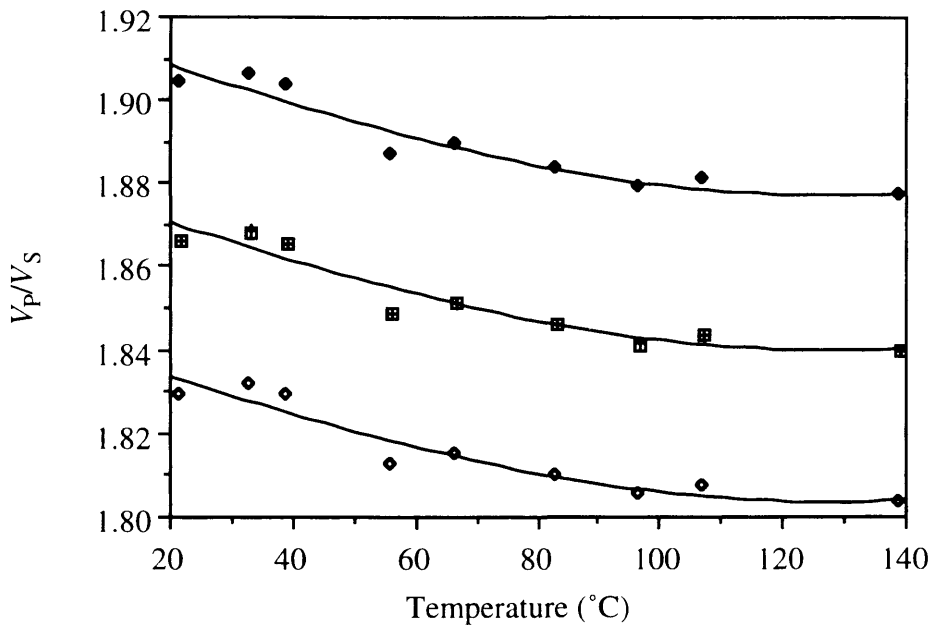
- ▣ both P- and S- velocity increased 1%; + both P- and S-velocity decreased 1%
- ◆ P-velocity increased 1% and S-velocity decreased 1%
- ◊ S-velocity increased 1% and P-velocity decreased 1%

FIG. 2.16. Pressure V_p/V_s pattern sensitivity analysis for impure halite (sample D, mixed with clay, compare with Figure 2.5b). Polynomial regression (3rd order) was applied to each individual case as denoted therein.



- ▣ both P- and S- velocity increased 1%; + both P- and S-velocity decreased 1%
- ◆ P-velocity increased 1% and S-velocity decreased 1%
- ◇ S-velocity increased 1% and P-velocity decreased 1%

FIG. 2.17. Pressure V_P/V_S pattern sensitivity analysis for detrital-framework salt (sample J, compare with Figure 2.11b). Polynomial regression (3rd order) was applied to each individual case as denoted therein.



- ▣ both P- and S- velocity increased 1%; + both P- and S-velocity decreased 1%
- ◆ P-velocity increased 1% and S-velocity decreased 1%
- ◇ S-velocity increased 1% and P-velocity decreased 1%

FIG. 2.18. Temperature V_P/V_S pattern sensitivity analysis for pure halite (sample L, compare with Figure 2.14b). a) polynomial regression (3rd order) was applied to each individual case as denoted therein.

Chapter 3 - Theory of anisotropic media of cubic symmetry

3.1 Introduction

One wants the exact expressions for seismic velocities as functions of propagation direction because velocity variation with propagation direction is one of the fundamental properties of seismic anisotropy. However, it can be extremely complicated to get the exact expressions for velocities with directional dependence in an arbitrary off-symmetry plane. This directional dependence of velocities for transversely isotropic media has been studied by Thomsen (1986) and Eaton and Stewart (1991); and in symmetry planes of orthorhombic media by Brown et al. (1991).

The crystal structure of halite salt belongs to the cubic symmetry class. For this case, I have derived the exact expressions for phase velocities in any direction. Group-velocity formulae are also developed for propagation in symmetry planes. One structure included in the cubic symmetry class has three 4-fold symmetry axes.

3.2 Determination of anisotropic parameters of salt

In order to deduce the stiffnesses of cubic salt, I selected a pure salt crystal sample (100% halite) (measuring 115×115×100 mm) (Figure 3.1). This large salt crystal grew in a very stable environment. Therefore, the crystal alignment was perfect. It is colorless to white, and crystallographic orientation is very clear.

In the cubic symmetry class, we define special directions (1,0,0), (0,1,0), and (0,0,1) as X , Y , Z , respectively. The direction halfway between X and Y is defined as (1,1,0). The planes that are orthogonal to those special directions are called symmetry planes [1,0,0], [0,1,0], [0,0,1], and [1,1,0] (see Figure 3.2). As will be described, phase velocity, group velocity, and stiffness have specific relationships in those directions.

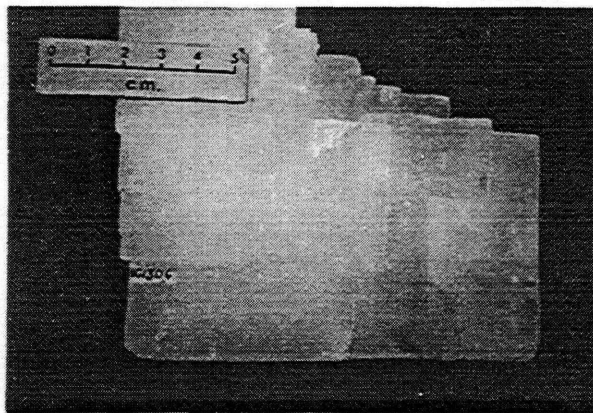


FIG. 3.1. Photograph of a large pure halite crystal (measuring $115 \times 115 \times 100$ mm) used for determining anisotropic parameters of halite.

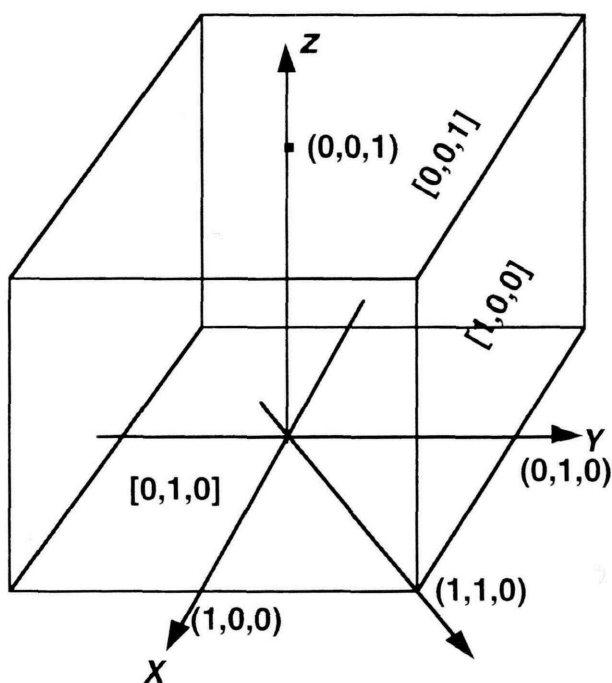


FIG. 3.2. Crystal symmetry and definition of directions $(1,0,0)$, $(0,1,0)$, $(0,0,1)$, and $(1,1,0)$ and symmetry planes $[1,0,0]$, $[0,1,0]$ and $[0,0,1]$, using convention defined in Chapter 2.

Optically, cubic symmetry is isotropic. Elastically, cubic symmetry is anisotropic. This can, simply, be explained by German's Theorem (Helbig, 1994). The optical properties of a crystal (tensor of rank two) are rotationally invariant with

respect to any n -fold axis with $n > 2$. In cubical crystals the three coordinate axes are four-fold, thus cubic crystals are optically isotropic. However, the elastic properties (tensor of rank four) are rotationally invariant with respect to any n -fold axis only when $n > 4$, thus cubic crystals are elastically anisotropic.

The waves propagating in anisotropic elastic media can be described by the well known Kelvin-Christoffel equation:

$$(n_i n_l c_{ijkl} - \rho v^2 \delta_{jk}) P_k = 0 \quad (3.1)$$

where Einstein's summation convention is employed, n_i is the unit vector normal to the wavefront, c_{ijkl} is the tensor of elastic stiffnesses, ρ is the density (for salt $\rho=2.165 \text{ g/cm}^3$, at $25 \text{ }^\circ\text{C}$), v is the phase velocity, δ_{jk} is the Kronecker delta, and P_k is particle motion or polarization vector.

The fourth-order tensors c_{ijkl} can be written as a second-order (6×6) symmetric matrix due to symmetry (Musgrave, 1970; Thomsen, 1986; Winterstein, 1990). In the case of cubic symmetry, only three independent stiffnesses have nonzero values (Musgrave, 1970; Miller and Musgrave, 1956). That is,

$$C_{11} = C_{22} = C_{33}, \quad C_{12} = C_{13} = C_{23}, \quad C_{44} = C_{55} = C_{66} \quad (3.2)$$

In the principal direction $n_i = (1,0,0)$, equation (3.1) gives solutions:

$$C_{11} = \rho v_{11}^2, \quad C_{44} = \rho v_{12}^2 = \rho v_{13}^2 \quad (3.3)$$

where v_{ij} is phase velocity, also equal to the group velocity due to the symmetry. The wave propagation direction is referred to by i , and j refers to the particle motion direction. The relationship between phase velocity and group velocity has been discussed by

Thomsen (1986). In the direction $n_i=(1,1,0)$, equation (3.1) gives the solution for P-wave phase velocity:

$$\rho v_{44}^2 = \frac{1}{2}(C_{11}+C_{12}+2C_{44}) \quad (3.4)$$

where v_{44} is the phase velocity in the direction halfway between symmetry axes. In order to deduce the stiffnesses, velocity measurements were carried out in the specific directions (1,0,0) and (1,1,0) through that salt crystal (Figure 3.1). The P- and S-wave velocities in two specific directions are listed in Table 3.1, together with deduced anisotropic parameters (stiffnesses).

Table 3.1 Salt anisotropy parameters

V_P (km/s)		V_S (km/s)		C_{11} *	C_{12} *	C_{44} *
(1,0,0)	(1,1,0)	(1,0,0)	(1,1,0)	47.0	14.0	12.3
4.66	4.45	2.38	S1: 2.83			
			S2: 2.38			

* unit: 10^{11} dyn/cm²

3.3 Formulae for phase and group velocities in media of cubic symmetry

It can be extremely complicated to get the exact expressions for directional dependence of velocities, which is one of the fundamental properties of seismic anisotropy in an arbitrary off-symmetry plane. However, I have derived the exact expressions for phase velocities in any direction for the case of cubic symmetry. Group-velocity formulae are also developed for propagation in symmetry planes.

Cubic symmetry is the structure that has three 4-fold rotation axes. For the case of cubic symmetry, the $3 \times 3 \times 3 \times 3$ stiffness tensor C_{ijkl} may be reduced to a 6×6 symmetric

matrix in which only three independent stiffnesses have nonzero values (Musgrave, 1970, Miller and Musgrave, 1956). That is:

$$\begin{bmatrix} C_{11} & C_{12} & C_{13} & C_{14} & C_{15} & C_{16} \\ C_{21} & C_{22} & C_{23} & C_{24} & C_{25} & C_{26} \\ C_{31} & C_{32} & C_{33} & C_{34} & C_{35} & C_{36} \\ C_{41} & C_{42} & C_{43} & C_{44} & C_{45} & C_{46} \\ C_{51} & C_{52} & C_{53} & C_{54} & C_{55} & C_{56} \\ C_{61} & C_{62} & C_{63} & C_{64} & C_{65} & C_{66} \end{bmatrix} = \begin{bmatrix} C_{11} & C_{12} & C_{13} & 0 & 0 & 0 \\ C_{12} & C_{22} & C_{23} & 0 & 0 & 0 \\ C_{13} & C_{23} & C_{33} & 0 & 0 & 0 \\ 0 & 0 & 0 & C_{44} & 0 & 0 \\ 0 & 0 & 0 & 0 & C_{55} & 0 \\ 0 & 0 & 0 & 0 & 0 & C_{66} \end{bmatrix} \quad (3.5)$$

In order to provide intuition into and simplify the phase- and group-velocity expressions, I introduce three parameters ε , γ , and φ for cubic symmetry (see Appendix D).

$$\varepsilon = (C_{11} - C_{44})^2 \left(\alpha - \frac{1}{3}\right) - \alpha(C_{44} + C_{12})^2 \quad (3.6)$$

$$\gamma = \beta[(C_{12} + C_{44})^2(3C_{11} - 2C_{12} - 5C_{44}) - (C_{11} - C_{44})^3] \quad (3.7)$$

$$+ \frac{1}{3}\alpha(C_{11} - C_{44})(C_{11} + C_{12})(C_{11} - C_{12} - 2C_{44}) - \frac{2}{27}(C_{11} - C_{44})^3 \quad (3.8)$$

$$\varphi = \arccos\left[-\frac{3\sqrt{3}\gamma}{2(-\varepsilon)^{3/2}}\right] \quad (3.9)$$

where

$$\alpha = n_1^2 n_2^2 + n_2^2 n_3^2 + n_3^2 n_1^2, \text{ and } \beta = n_1^2 n_2^2 n_3^2. \quad (3.10)$$

Recall that the unit vector (n_1, n_2, n_3) is a function of phase angle (θ) . We have the exact expressions for the phase velocities as functions of phase angle in 3-D space (any arbitrary direction) (see Appendix D).

3.3.1 Phase Velocity

The P -wave and two shear-wave phase velocities can be expressed by:

3.3.1.1 P-wave phase velocity

$$v_p^2 = \frac{2\sqrt{(-3\varepsilon)}}{3\rho} \cos\frac{\varphi}{3} + \frac{C_{11} + 2C_{44}}{3\rho} \quad (3.11)$$

3.3.1.2 SV-wave phase velocity

$$v_{sv}^2 = \frac{2\sqrt{(-3\varepsilon)}}{3\rho} \cos\left(\frac{\varphi}{3} + \frac{2\pi}{3}\right) + \frac{C_{11} + 2C_{44}}{3\rho} \quad (3.12)$$

3.3.1.3 SH-wave phase velocity

$$v_{sh}^2 = \frac{2\sqrt{(-3\varepsilon)}}{3\rho} \cos\left(\frac{\varphi}{3} + \frac{4\pi}{3}\right) + \frac{C_{11} + 2C_{44}}{3\rho}. \quad (3.13)$$

The shear-wave singularities (two shear waves having the same phase velocity) in salt are on the major symmetry axes. At these points, formulations can be written as follows:

$$v_p^2 = \frac{\sqrt[3]{(-4\gamma)}}{\rho} + \frac{C_{11} + 2C_{44}}{3\rho} \quad (3.14)$$

$$v_{sv}^2 = v_{sh}^2 = \frac{\sqrt[3]{4\gamma}}{2\rho} + \frac{C_{11} + 2C_{44}}{3\rho} \quad (3.15)$$

3.3.2 Group Velocity

Components of the group velocity can be computed by using the equation developed by Kendall and Thomson (1989), as long as the phase slowness is available. In a symmetry plane the group velocity can be determined from phase velocity using well-known relationships (Postma, 1955; Backus, 1965)

$$V^2(\phi) = v^2(\theta) + \left(\frac{dv}{d\theta}\right)^2 \quad (3.16)$$

$$\tan\phi = \frac{v \tan\theta + \left(\frac{dv}{d\theta}\right)}{v - \left(\frac{dv}{d\theta}\right) \tan\theta} \quad (3.17)$$

It is indicated in (3.16) and (3.17) that along a symmetry axis, group velocity is equal to phase velocity and phase angle (θ) or slowness direction is the same as the group angle (ϕ) or angle of incidence of the ray. This is because the derivative of phase velocity with respect to phase angle in that direction is zero, namely:

$$\frac{dv}{d\theta} = 0. \quad (3.18)$$

Phase velocities (v) and slowness against phase angle (θ) in a typical symmetry plane of salt indicate that, at those points which represent symmetry axes, the velocity is stationary with respect to phase angle in that direction. It is also indicated in (3.16) and (3.17) that group angle (ϕ) is a function of phase angle (θ). More detailed and intuitive discussion is given by Brown et al. (1991). Group-velocity surfaces in these symmetry planes are similar. In one of the symmetry planes, the unit vector (n_1, n_2, n_3) is given by:

$$n_1 = \cos\theta, \quad n_2 = \sin\theta, \quad n_3 = 0. \quad (3.19)$$

From equation (3.10) we have $\alpha = \cos^2\theta\sin^2\theta$ and $\beta = 0$. The following formulae are derived (Appendix A) for group velocities (V_P , V_{SH} , V_{SV}) in a typical plane of cubic symmetry:

$$V_P^2 = v_P^2 - \frac{\cos^2(\varphi/3)\sin^2(4\theta)}{48\rho^2v_P^2\epsilon}(C_{11} + C_{12})^2(C_{11} - C_{12} - 2C_{44})^2 \quad (3.20)$$

$$V_{SV}^2 = v_{SV}^2 - \frac{\cos^2((\varphi + 2\pi)/3)\sin^2(4\theta)}{48\rho^2v_{SV}^2\epsilon}(C_{11} + C_{12})^2(C_{11} - C_{12} - 2C_{44})^2 \quad (3.21)$$

$$V_{SH}^2 = v_{SH}^2 - \frac{\cos^2((\varphi + 4\pi)/3)\sin^2(4\theta)}{48\rho^2v_{SH}^2\epsilon}(C_{11} + C_{12})^2(C_{11} - C_{12} - 2C_{44})^2. \quad (3.22)$$

Again, at those points where there are shear-wave singularities the group velocities are expressed by the following formulae:

$$V_P^2 = v_P^2 + \frac{(4\gamma)^{2/3}\sin^2(4\theta)}{81\rho^2v_P^2(4\gamma)^2}(C_{11} + C_{12})^2(C_{11} + C_{44})^2(C_{11} - C_{12} - 2C_{44})^2 \quad (3.23)$$

$$V_{SH}^2 = V_{SV}^2 = v_{SH}^2 + \frac{(4\gamma)^{2/3}\sin^2(4\theta)}{324\rho^2v_{SH}^2(4\gamma)^2}(C_{11} + C_{12})^2(C_{11} + C_{44})^2(C_{11} - C_{12} - 2C_{44})^2. \quad (3.24)$$

The first quadrant of the wave surfaces (or group-velocity surfaces) on the section, illustrated in Figure 3.6 were generated from slowness surfaces and represent theoretical wavefronts at 1 second. As indicated by Figure 3.6, the qSH wavefront is nearly circular and the maximum shear-velocity difference is approximately 20% in the (1,1,0) direction. Also, the P-wave velocity in that direction approaches a minimum value. The points where

the two shear waves have the same velocity are on the principal or symmetry axes. This agrees with the results observed experimentally (Table 3.1).

3.4 Phase and group velocity surfaces in cubic salt

Let us recall the definition of phase and group velocity. The relationship between phase velocity and group velocity has been discussed by many authors (Musgrave, 1970, Thomsen, 1986, Brown et al. 1991). Except for some special directions, such as symmetry directions, the group-velocity direction (raypath direction) is not, in general, the same as the phase-velocity direction (wavefront-normal) (see Figure 3.3).

Figure 3.3 shows the notation documented by Brown et al. (1991) which is similar to Musgrave's (1970). Physically, except in situations when transducers are too large and/or samples too small, group velocity is the one that can be estimated through laboratory measurement.

The phase- and group-velocity surfaces of cubic salt can be calculated through formulae described above (equation 3.20-3.24) using the anisotropic parameters listed in Table 3.1. Also, components of group velocity can be computed by using the equation developed by Kendall and Thomson (1989), as long as the phase slowness is available.

$$V_i = \frac{C_{ijkl} p_l D_{jk}}{\rho D_{qq}} \quad (3.25)$$

where D_{jk} is a cofactor of the matrix $c_{ijkl} p_i p_l / \rho - \delta_{jk}$, and p_l is slowness.

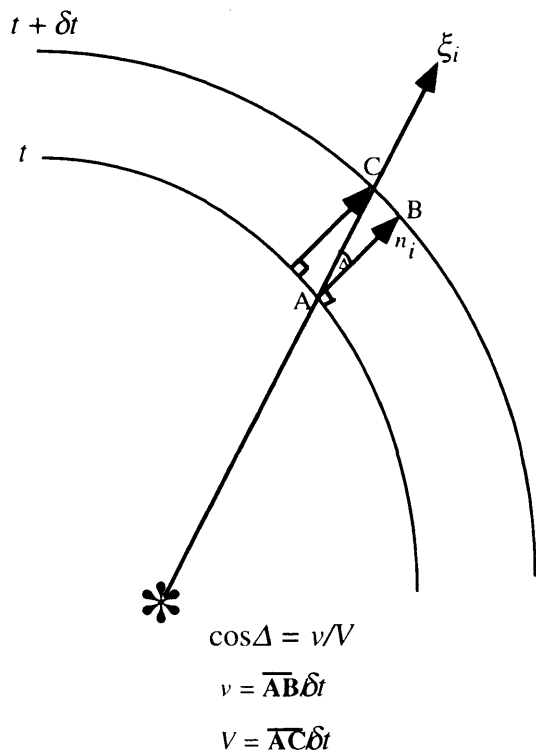


FIG. 3.3 Schematic diagram of a wavefront in an anisotropic medium at times t and $t + \delta t$, showing the phase and group velocities (v and V respectively), their respective unit vectors (n_i and ξ_i) and the angle Δ between n_i and ξ_i (modified after Brown et al., 1991).

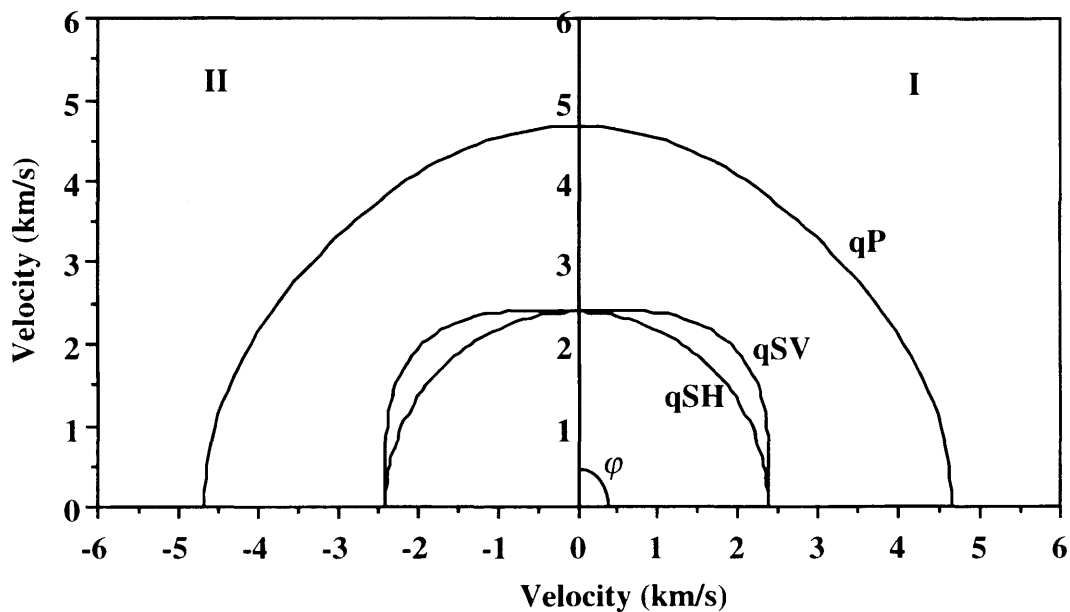


FIG. 3.4. Phase-velocity surfaces for compressional- and shear-wave in 2 quadrants on section $[0,0,1]$ (symmetry plane) for cubic salt.

The phase-velocity surfaces (4 quadrants) on section $[0,0,1]$ were computed and plotted in Figure 3.4, These are identical for faces $[1,0,0]$ and $[0,1,0]$ due to the cubic symmetry. Suppose that there are P-wave and shear-wave sources located in the coordinate $(0.0, 0.0)$. These wave surfaces then represent the theoretical wavefront normal of compressional wave and the two shear waves at 1 second. The phase-slowness surfaces in the first quadrant (Figure 3.5) were generated directly from the phase velocities. The wave surfaces (or group-velocity surfaces) on the section, as the final results were approached, were generated and illustrated in Figure 3.6 (first quadrant). As indicated by Figure 3.6 the qSH -wave surface is nearly circular and the maximum shear-velocity difference is approximately 20% in the $(1,1,0)$ direction which is half way (45°) between the vertical and horizontal axes. Also the shear-wave cusp points, where there are more than two shear velocities, are around this direction. The P-wave velocity in that direction approaches a minimum value. The directions in which the two shear waves have the same velocity are along the symmetry axes. This agrees with the results observed in the experiments (see Table 3.1).

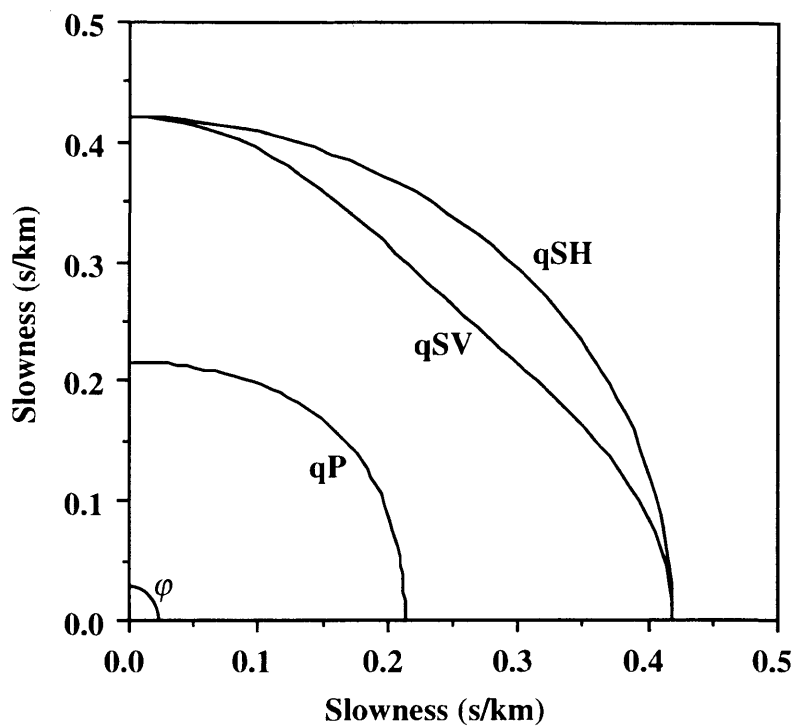


FIG. 3.5. Phase-slowness surfaces for compressional and shear waves in the first quadrant on section $[0,0,1]$ (symmetry plane) for cubic salt.

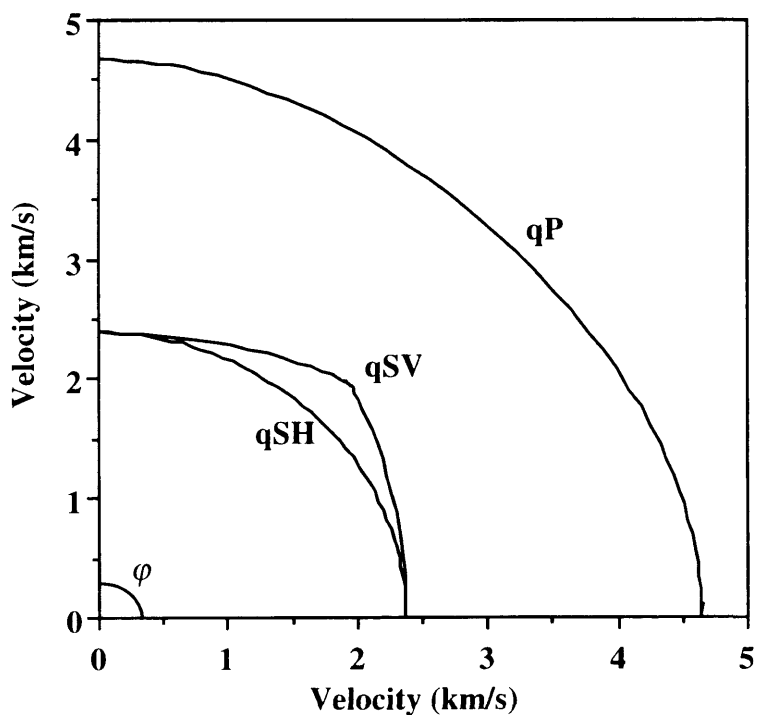


FIG. 3.6. Group-velocity (wave) surfaces for compressional and shear waves in the first quadrant on section $[0,0,1]$ (symmetry plane) for cubic salt.

Chapter 4 - Physical modelling with salts and numerical modelling with cubic salt

4.1 Introduction

Salt anisotropy is related to geological process that salt experienced. It is now clear that chevron salt and recrystallized salt are anisotropic, whereas metamorphic salt can be anisotropic or isotropic depending on the nature of the metamorphic alteration. The features of cubic salt anisotropy and how the anisotropy can be observed have been discussed in chapter 3. In order to study salt anisotropy further, integrated modelling studies have been carried out. In this chapter I will discuss the results of shear-wave physical modelling (zero-offset and offset transmission experiments through different types of salt, physical modelling around a chevron-salt sphere), and the results of numerical modelling through a VSP model with an anisotropic layer.

The physical modelling experimental study was done on 17 salt samples which were collected from six different areas in Alberta, Canada. The shear-wave records are shown for four salt samples: (1) a large pure salt crystal with lengths 115.0, 106.3, 100.4 mm in the A, B, C directions, respectively; (2) a fairly pure salt core (recrystallized salt) with length 95.9 mm and 101.0 mm in diameter (crystal size 5-12 mm, from well: 10-32-45-1W4); 3. a chevron salt sample with length 279.9 mm and 88.0 mm in diameter (crystal shape cannot be seen, from well: 6-30-86-13W6); 4. an impure salt sample mixed with clay with length 145.43 mm and 101.0 in diameter (crystal size 1-5 mm, from well: 10-32-45-1W4). All four samples were used in the zero-offset azimuthal rotation transmission experiment. Only sample 2 was used in the offset transmission experiment, and a salt sphere was made of chevron salt.

This chapter addresses the following issues: (1) it examines what types of salt exhibit anisotropy as predicted in chapter 2; (2) the features of anisotropy ; (3) the percent

velocity change of the two shear waves; (4) shear-wave event identification and analysis on the offset transmission-time section; (5) the properties of chevron-salt and cubic symmetry; and 6) numerical characteristics of a VSP model with cubic salt.

4.2 Physical modelling with different types of salt

4.2.1 Experimental setup

The experiments were set up with piezoelectric P-wave and S-wave transducers as both the acoustic sources and receivers, a sample holder that clamps the sample, a protractor that controls the azimuth, and an azimuth pointer (see Figure 4.1). Both types of transducer are flat-faced cylindrical contact transducers with an active element 12.6 mm in diameter. The P-wave transducer (Panametrics **V103**) is normally polarized, with the maximum sensitivity normal to the contact face. The S-wave transducer (Panametrics **V153**) is plane polarized, with the maximum sensitivity parallel to a direction across the contact face.

For zero-offset transmission modelling with azimuthal rotation of the sample, the shear source and receiver transducers were oriented with the same polarization. For offset transmission experiments the radial component (or SV component) was recorded by using shear source and receiver transducers with polarizations parallel to each other, while the transverse component (or SH component) was recorded by using shear source and receiver transducers with polarizations perpendicular to each other.

Amplified data were sampled every 50 ns using a Nicolet digital oscilloscope connected, through an IBM-XT, which controls the experiment, to a Perkin-Elmer 3240 seismic processing system for storage. Each trace contains 4000 samples and was stored on disk in SEG-Y format. The record length was 0.2 ms.

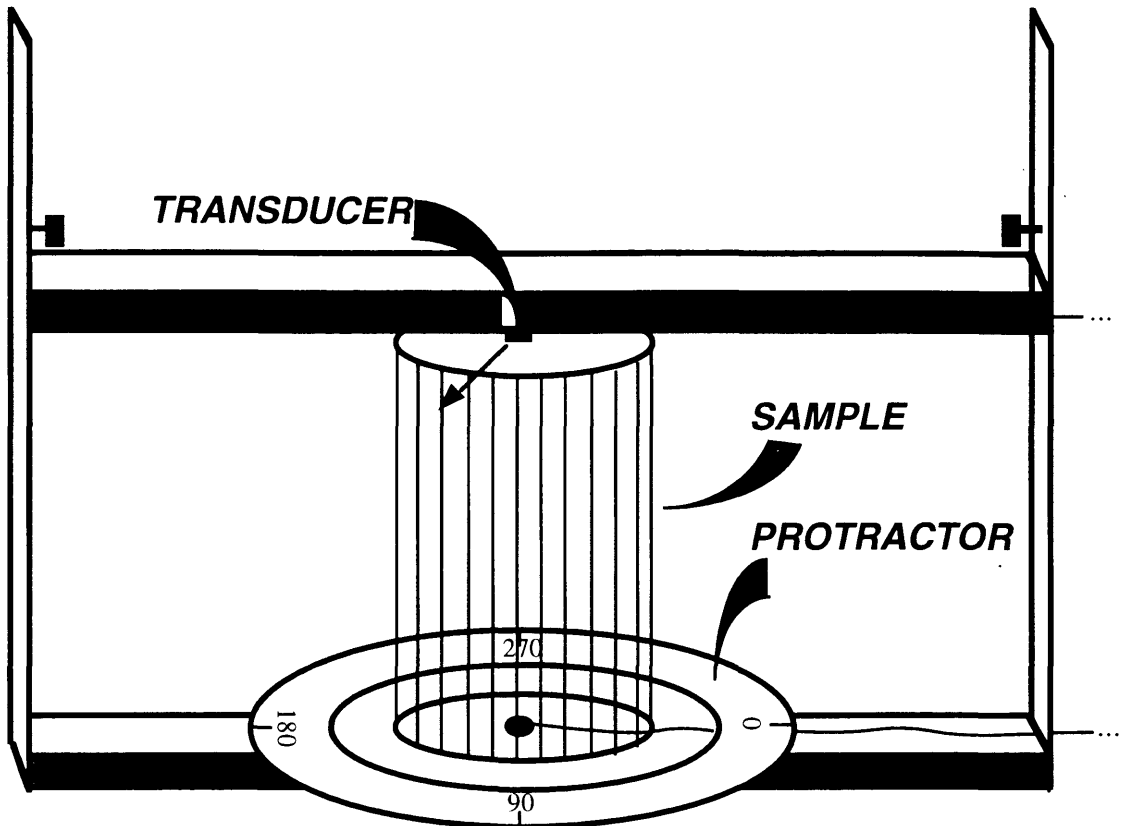


FIG. 4.1 Schematic diagram of apparatus used for shear-wave splitting experiments. The apparatus clamps the sample between two shear-wave transducers of parallel and orthogonal polarization. During the experiment the sample is rotated whereas the transducers remain fixed. A circular protractor scale is used to determine the azimuth of the rotation.

4.2.2 Zero-offset azimuthal-rotation transmission experiment

In this experiment, the sample was placed between two fixed shear-wave transducers which were aligned with parallel polarizations. The sample was rotated between the transducers and a pointer on the sample was used to determine the azimuth of the sample with respect to a fixed circular protractor (Figure 4.1). Data were recorded every 11.25° per trace (from 0° to 360°) with 32 traces per record. Similar experiments were carried out by Tatham et al. (1987) for the study of fracture-induced shear-wave splitting and Cheadle et al. (1991) in an orthorhombic-anisotropy model study.

The transmission records for propagation through a pure salt crystal sample (where a principal axis is the same as a rotational axis) are shown in Figure 4.2. The plot shows that there is no time shift of shear-wave first arrivals in any of the polarization directions. It indicates that the results from actual observations agree with the theoretical wave surfaces, i.e. there is only a single shear-wave velocity along the principal axis.

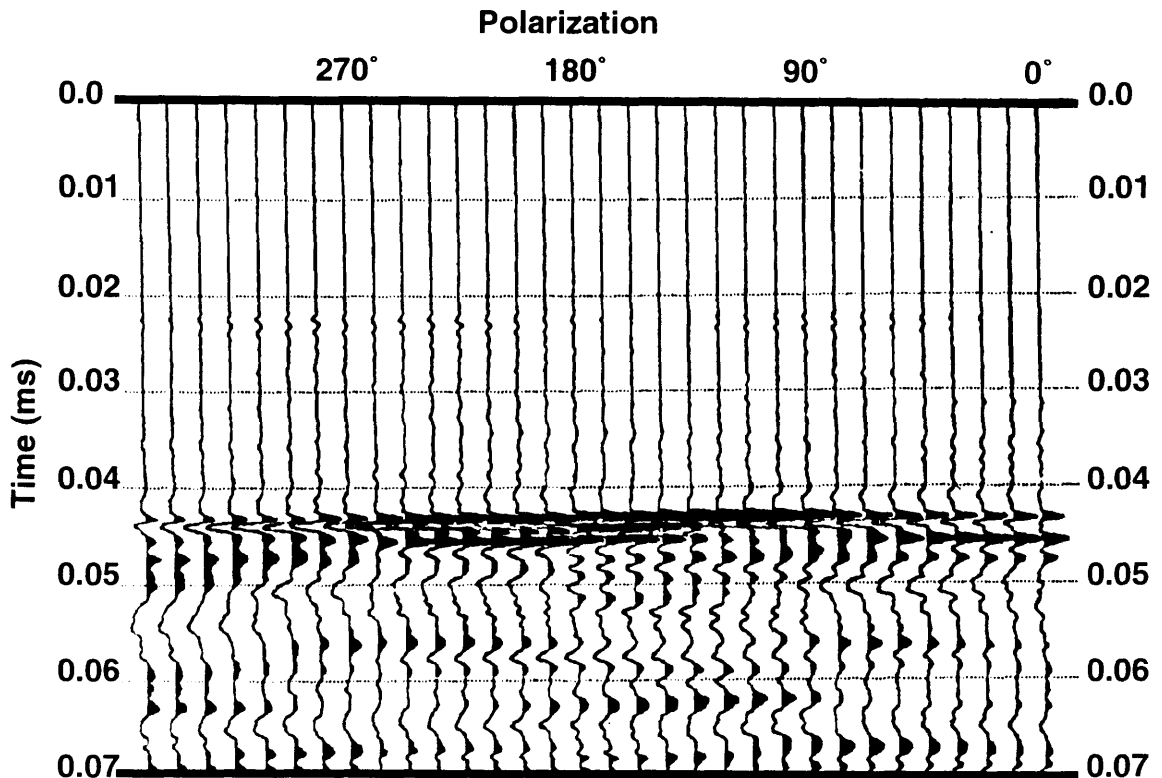


FIG. 4.2. Shear-wave record of a zero-offset transmission experiment on a pure salt crystal (axis length: 100.4 mm), showing no shear-wave splitting; the rotation axis is a principal axis of symmetry (approximately) of the salt crystal. Both shear-wave transducers were rotated from 0° to 360° at increments of 11.25° .

The experimental results from a chevron salt core sample is shown in Figure 4.3. It is shown that the shear-wave first arrival traveltimes change as the polarization changes. The change in shear-wave velocity is 4.8% (Table 4.1). The result for a recrystallized pure salt core sample, for which crystal sizes range from 1 to 6 mm, is shown in Figure 4.4. The shear-wave velocity change is 4.6% (Table 4.1). However, impure salt (mixed uniformly

with clay), with crystal sizes from 1 to 10 mm, does not show shear-wave splitting (Figure 4.5). The P, S1, S2 velocities measured from different samples are summarized in Table 4.1. These values are group velocities based on the transit time. The time picks used to calculate the velocities were made directly on the digital oscilloscope for maximum accuracy.

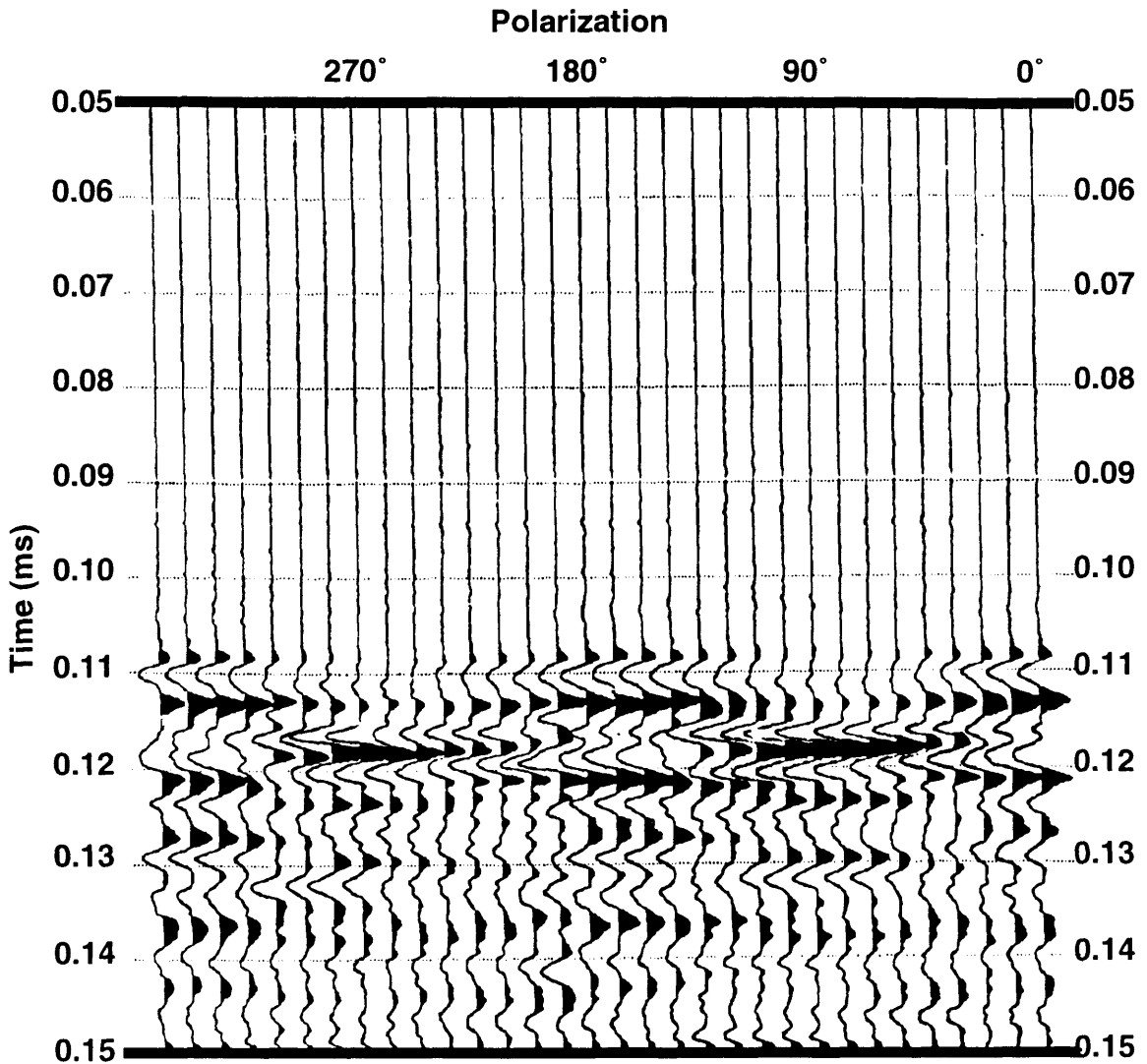


FIG. 4.3 Shear-wave record of a zero-offset transmission experiment on a chevron-salt sample (length: 279.9 mm) with the same experimental setup as in Figure 4.2, showing shear-wave splitting as first arrivals vary with respect to polarization; the rotation axis is the core axis direction.

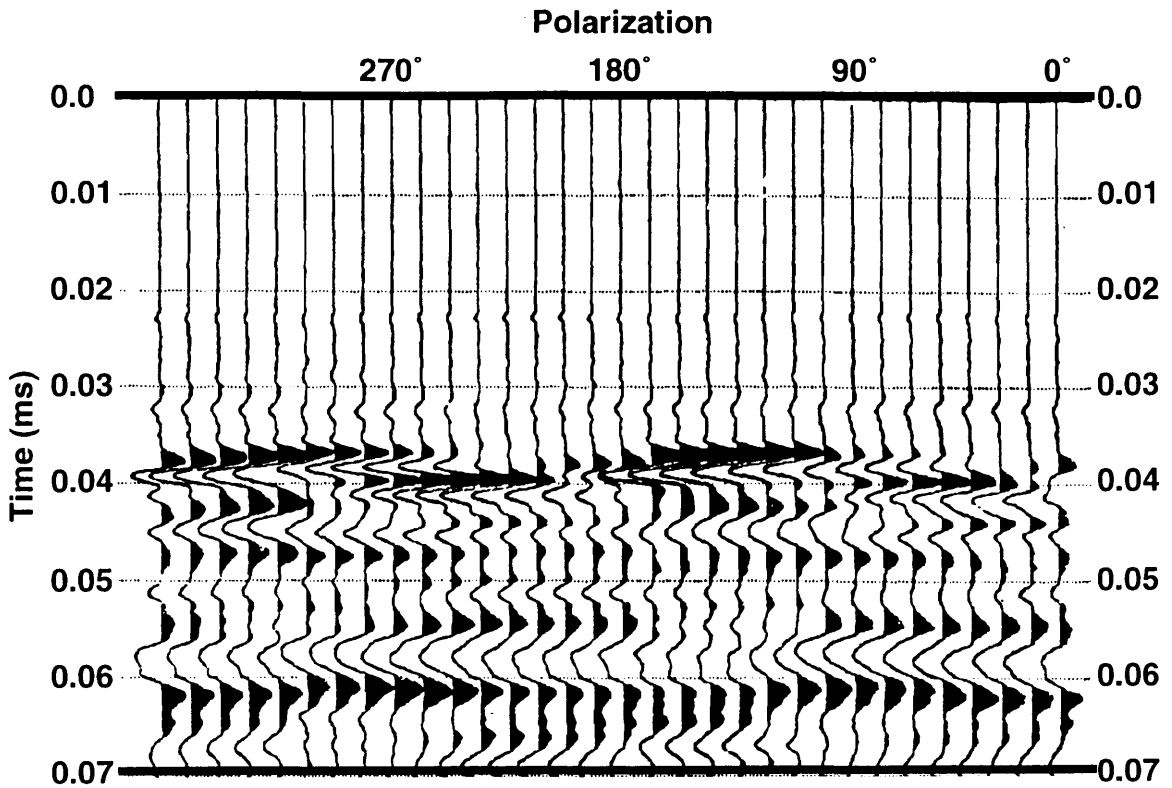


FIG. 4.4. Shear-wave record of a zero offset transmission experiment on a recrystallized salt sample (length: 95.9 mm, crystal size: 1-6 mm) with the same experimental setup as in Figure 4.2; the rotation axis was the core axis, showing shear-wave splitting as first arrivals vary with respect to polarization.

All the shear-wave records that show anisotropy, except on a symmetry axis, have a period of 180° for the two shear-waves. This is an important feature of shear waves propagating in anisotropic media, i.e., there are usually two different polarizations perpendicular to each other. On the sections of wave surfaces such as in Figure 3.5 we can see shear-wave cusp points where more than two shear-wave velocities can be seen.

The above experiments show that chevron-salt and recrystallized salt are anisotropic. The velocity difference between the fast and slow shear-wave velocities, observed from cores in the laboratory, is around 5%, indicating that the core-axis (near-vertical) is not the direction (1,1,0) of maximum anisotropy (20% from theoretical prediction).

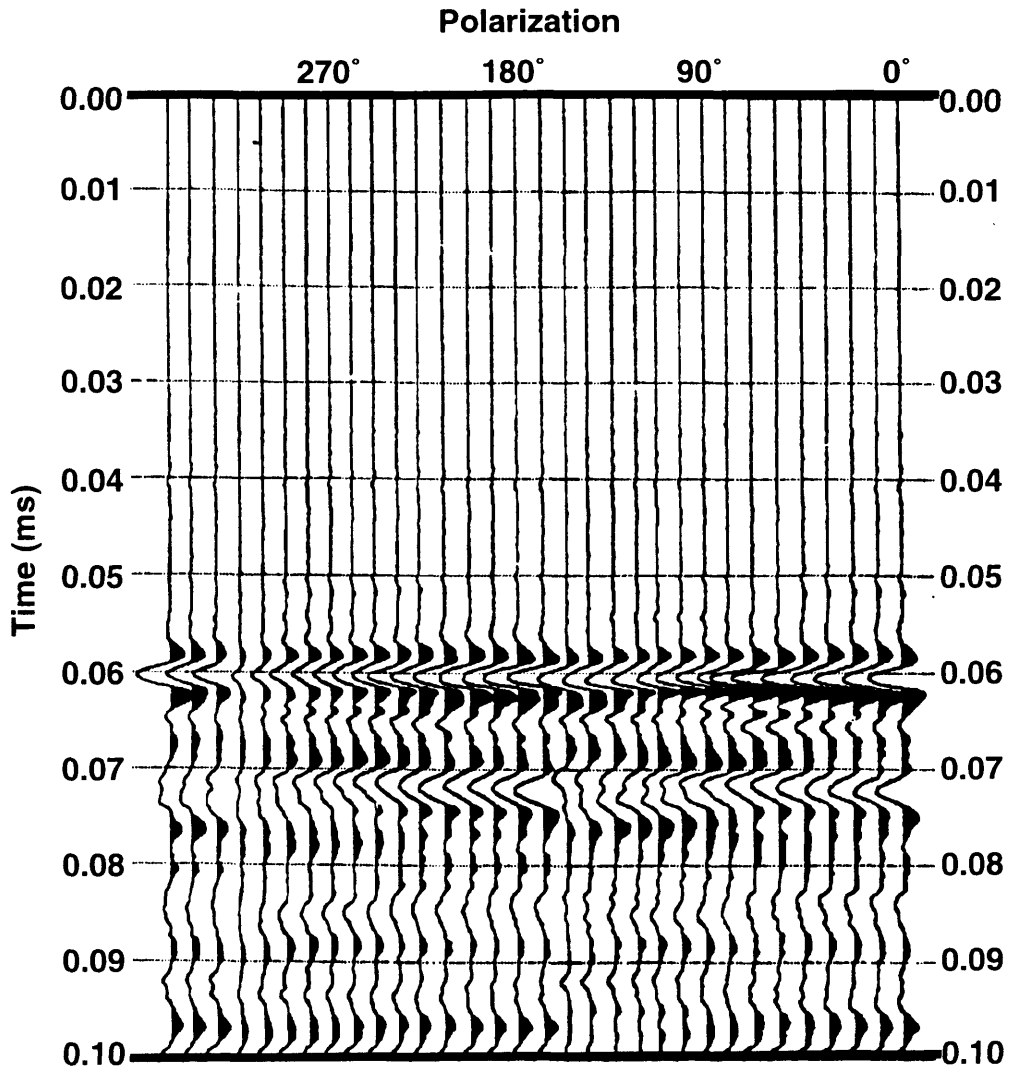


FIG. 4.5 Shear-wave record of a zero-offset transmission experiment on an impure salt sample mixed uniformly with clay (length: 145.4 mm) with the same experimental setup as in figure 4.2, showing no shear-wave splitting; the rotation axis was the core axis.

Table 4.1. Velocities on different types of salt samples

samples	wave propagation direction	length (mm)	P-wave velocity (km/s)	S1 velocity (km/s)	S2 velocity (km/s)	δ -velocity change (%)
pure salt crystal	(1,1,0)	155.80	4.45	2.83	2.38	20.1
recrystallized salt		95.90	4.42	2.69	2.56	4.6
chevron pure salt		279.93	4.51	2.61	2.49	4.8
salt mixed with clay		145.43	4.38	2.58		0

4.2.3 Offset transmission experiment

In the above experiment, S1 was observed at an azimuth of 45° and S2 at an azimuth of 135° in the recrystallized salt sample (Figure 4.4). In the present experiment, compressional and shear transducers have been used to obtain time sections that include both compressional and shear events in the case of nonzero source-receiver offset.

Figure 4.6 shows the plan view and cross-section of the model. One transducer was on the bottom of the model, and the other was moved along the lines on the top of the model. The actual spatial increment between traces is 0.5 cm. The centre of the transducer at the bottom is at an offset of 0.6 cm. The maximum value of X is 9.5 cm. So each section contains 19 traces along the line.

The data have been acquired along three lines: a "random" line (Line 1) at an azimuth of 33.75° (same labelling system as the above experiment); a line along the fast shear direction (Line 2, S1, the direction with shortest first-arrival time on the plot of azimuthal transmission experiment); and a line along the slow shear direction (Line 3, S2).

Before the experimental results are shown, one should note some of the features of this experiment. Due to the limitation of the sample size, distances as small as 0.5 cm were used as receiver interval. This implies some source overlap at adjacent receiver locations

(there may be source effects to the results of the experiment) because the radius of transducers is an even 0.6 cm.

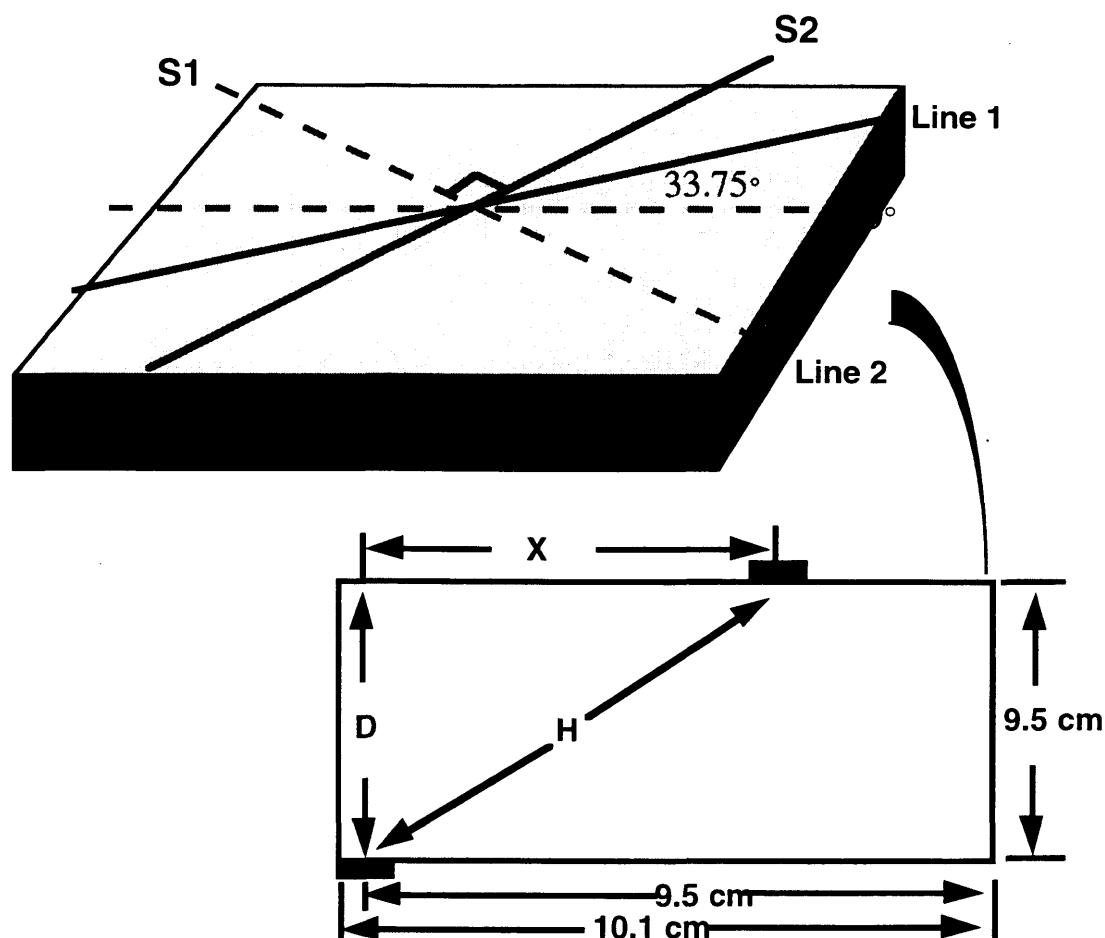


FIG. 4.6 Plan view and cross-sectional schematic diagram of the offset transmission experiment. D (depth) is the length of the salt sample. X is the lateral offset of receiver position, and H is the hypotenuse connecting the source and receiver.

Secondly, the energy radiation pattern of this experiment is that most energy (both P and S) is restricted within a certain solid angle like a "beam" (see Figure 4.7) because of the flat contact between transducers and rock faces. When the source transducer is fixed at a certain location, the energy received from source to receiver decreases rapidly as the source–receiver offset increases .

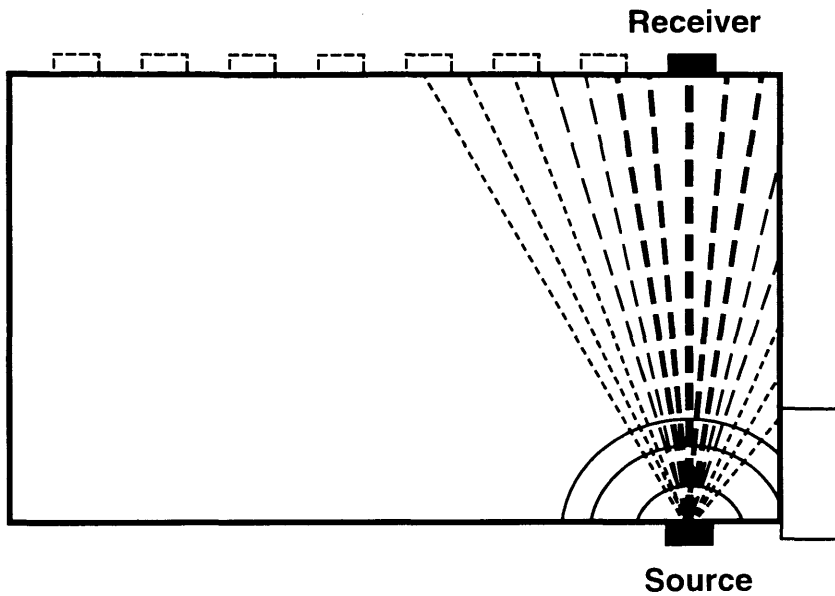


FIG. 4.7. Schematic diagram of energy radiation pattern of source-receiver offset transmission experiment, showing that most energy is restricted within a narrow range of angle (the near offsets); the further the offset the lower the energy density leaving the source.

Thirdly, for SV-wave records, polarity can be reversed due to source-receiver geometry. Excluding the vertical ray path (Figure 4.7) the polarity of SV waves recorded at receivers to the right is the opposite of that recorded at receivers to the left.

As described in Chapter 3, there is no shear-wave splitting on the symmetry axes in an anisotropic medium of cubic symmetry (Figure 4.8), i.e. these are singular directions and there are three such. Therefore, compared with TI media and azimuthal anisotropic media, there is more opportunity for shear-wave raypath to fall near singular directions, where there is no splitting. Still, for any raypath sufficiently off the symmetry axes, shear-wave splitting is observable; and the amount of anisotropy can be as high as 20% in the direction half way between symmetry axes.

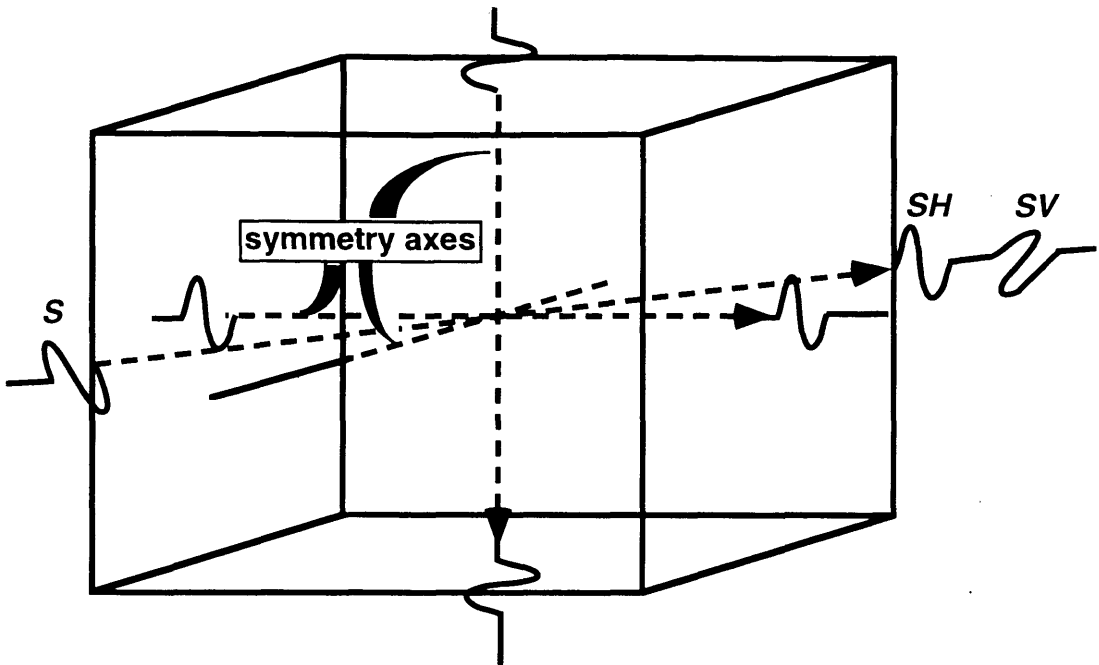


FIG. 4.8. Shear-wave splitting rationale in an anisotropic medium of cubic symmetry; except for propagation on symmetry axes (three directions), shear-wave splitting will occur.

A compressional (P) wave record is shown in Figure 4.9 with P-wave source and P-wave receiver. When the two transducers (source and receiver) are parallel and the contact between transducer and core sample face are well coupled, a P-wave record usually does not show shear waves (Figure 4.9). Exceptions sometimes occur when two ends of the sample are not parallel. The purpose of recording P waves was to observe whether the first P-wave arrivals fall onto a hyperbolic curve. We will find that both the P-wave and S-wave first arrivals are nonhyperbolic.

Line 3 is oriented in the direction close to the polarization of S₂ (slower shear-wave) (Figure 4.6). The data recorded from an inline shear source (polarized in the direction of fast shear) with both inline and crossline receivers (polarized in the direction of slow shear) over a salt block are shown in Figure 4.10.

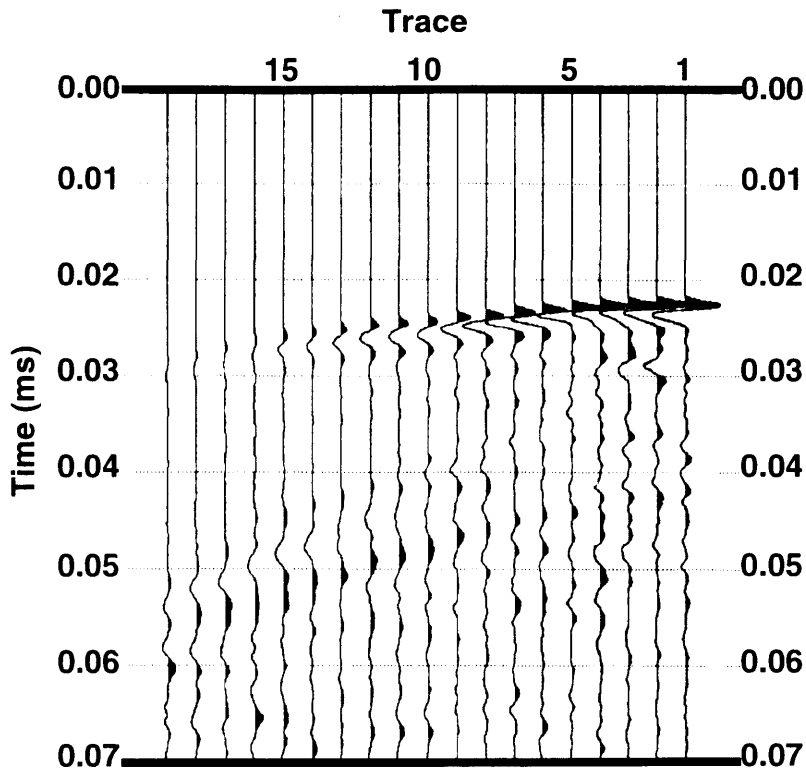


FIG. 4.9. Record of an offset transmission experiment with a P-wave source and P-wave receiver from Line 2.

As was expected, a weak P-wave event, a strong S2 event and a weak S1 event are shown on this section of inline source and inline receiver (Figure 4.10a). On the section of inline source and crossline receiver we expect to see both strong S1 and S2 event because the line is oriented to S2 (slow shear polarization).

Figure 4.11 shows a shear-wave record along the "random" line (Line 1) where clear shear-wave splitting can be detected due to the orientation of the line. The polarity of the fast shear (S1 or SV) is reversed after trace 5. This is explained by the offset effect i.e., the SV polarity reverses when the offset changes sign. In contrast, the S2 or SH polarity does not change polarity when the offset changes sign. This effect enables us to identify S1 and S2 with confidence. Figure 4.12 shows the shear-wave record along Line 2 which is oriented along a direction close to the polarization of S1 (fast shear wave) (Figure 4.6). The

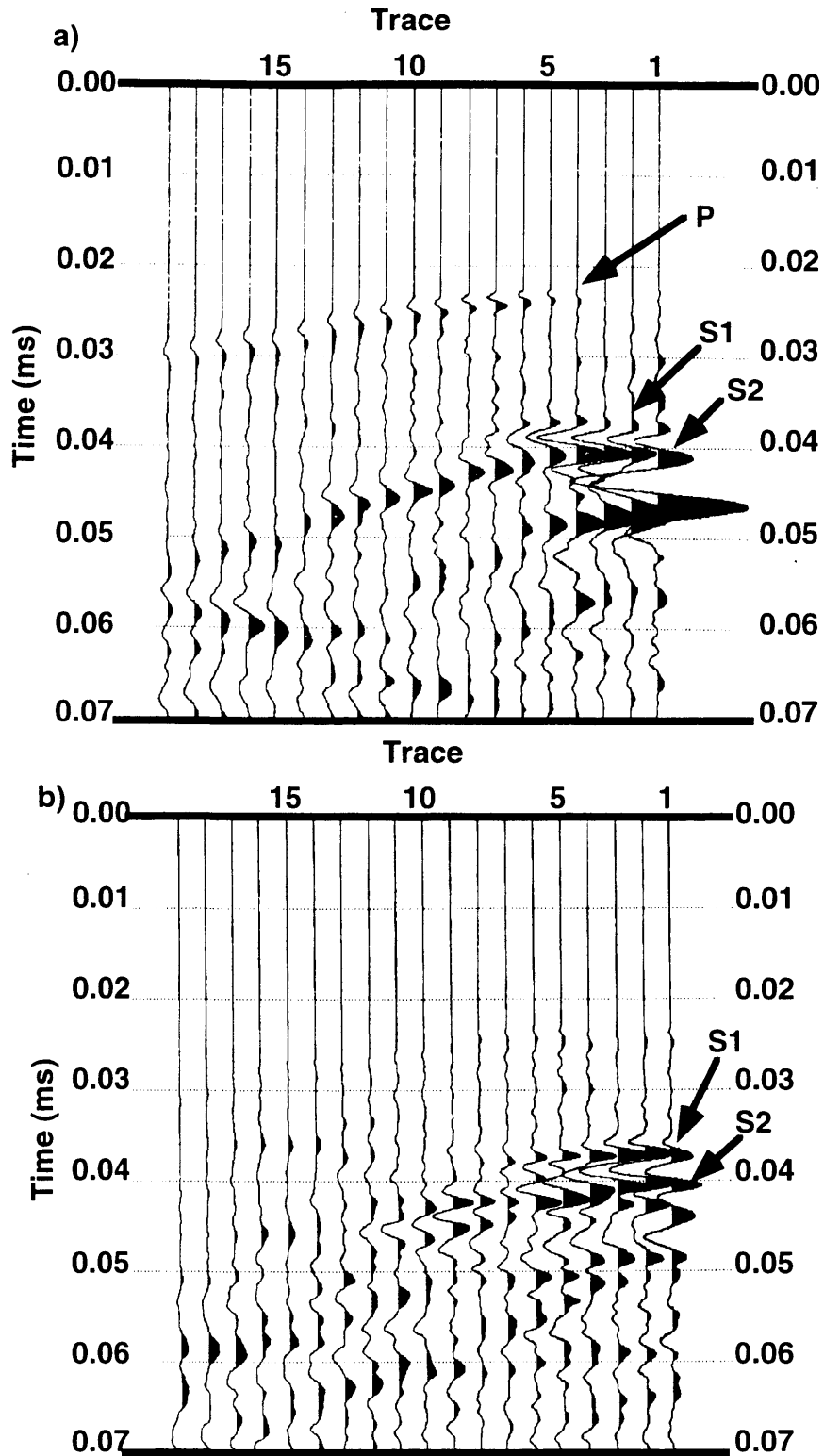


FIG. 4.10. Shear-wave record of an offset transmission experiment along Line 3 with inline shear source and both (a) inline and (b) crossline receivers.

first P-wave event is stronger on the record of the inline source (polarized S1) and inline receiver than on that of the inline source and crossline receiver (polarized S2 direction), which indicates the presence of a component of P-wave energy from shear-wave transducer. Also, as was expected, the amplitudes on the first shear-wave record (Figure 4.12a) are much stronger than that of second (Figure 4.12b). As a matter of fact, it is hard to see fast shear arrivals on the inline source crossline receiver (Figure 4.12b).

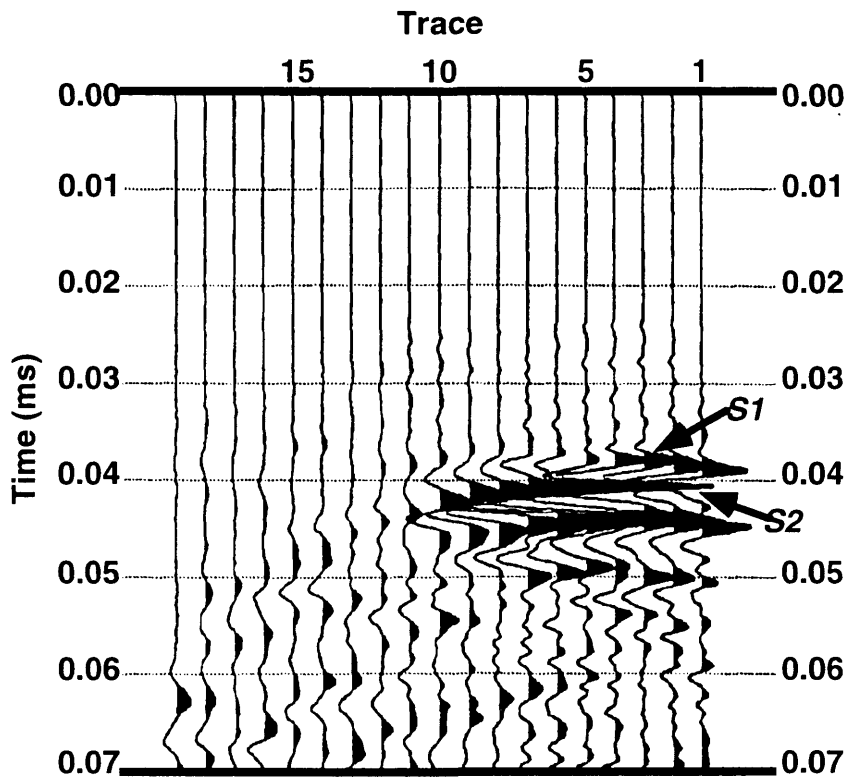


FIG. 4.11. Shear-wave record of an offset transmission experiment along a random line (Line 1) with inline shear source and crossline receiver, showing fast shear (S1) and slow shear (S2) and polarity reversal of S1.

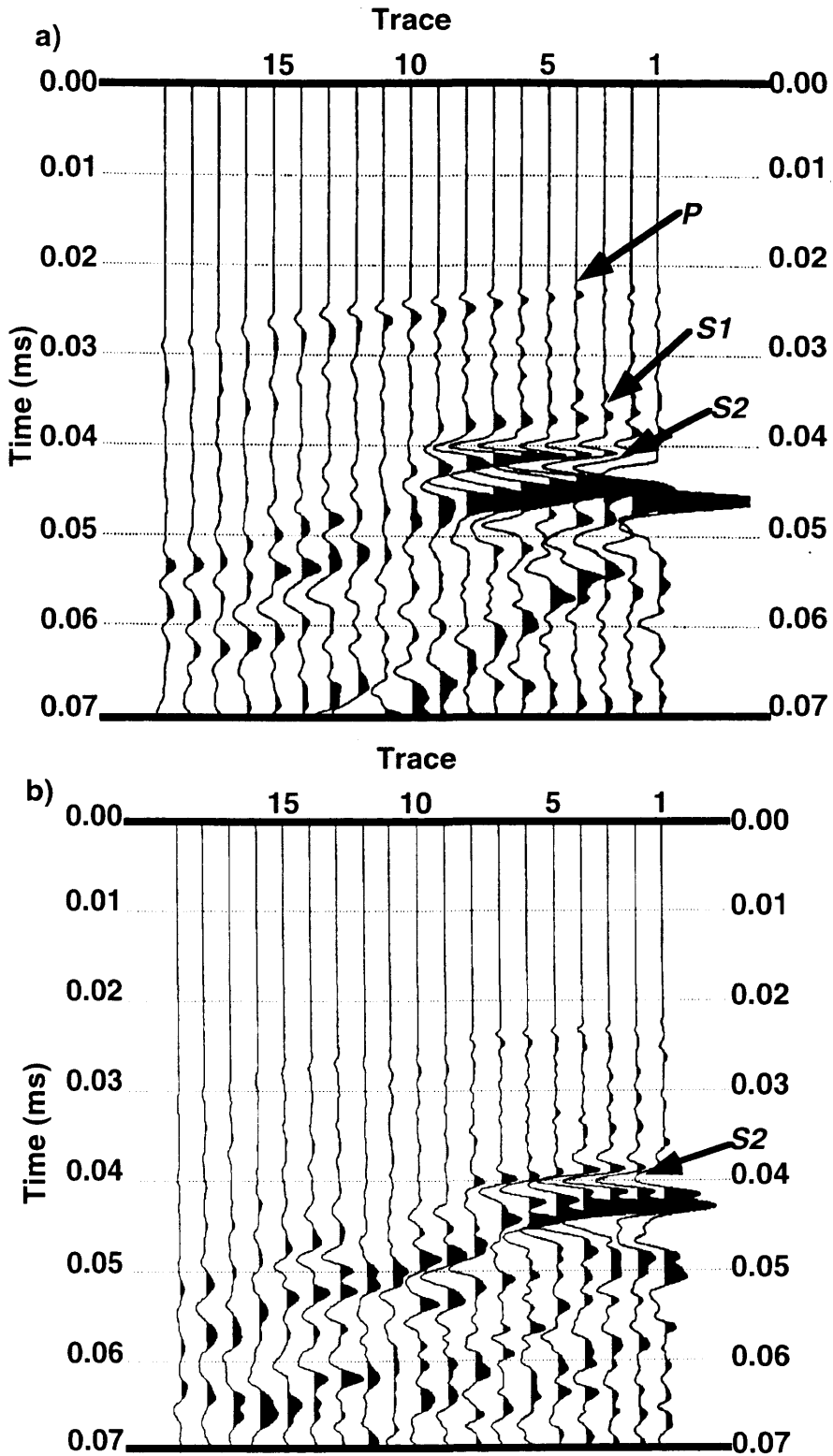


FIG. 4.12. Shear-wave record of an offset transmission experiment along Line 2 (fast shear direction) with inline shear (S1) source and both inline (a) and crossline (b) receivers.

The observations of the offset transmission experiments have further shown chevron and recrystallized salts to be anisotropic. Also, the experiments indicate that shear-wave events can be identified on offset time sections. However, they are probably not hyperbolic and the recorded amplitude of each trace is the vector summation of a faster shear wave and slower one. That is, the two shear waves overlap and interfere with each other. Far-offset shear-wave events die out or change due to the radiation pattern and some effects of anisotropy.

4.2.4 Transmission experiment around a chevron-salt sphere

The third physical modelling study was carried out by recording shear waves propagating through a sphere made of a chevron salt sample which consists of equigranular (around 1-2 mm), white to colourless halite crystals, with vertically oriented cloudy and milky patches. Crystallographic orientation is not observable (salt type IA). The modelling scalings were the same as above (frequency scaling 10,000:1, distance and time scaling 1:10,000). The data were recorded at 15° per trace (from 0° to 180°) with 13 traces per record. The schematic diagram of the modelling geometry is shown in Figure 4.13. The circumference of the circle 1 is 11.7 cm which indicates that the diameter of the sphere is 3.72 cm. In order to observe the anisotropic properties of this salt medium, shear-wave transducers are oriented in three different ways:

- Radial–Radial (R–R) polarization.

The two transducers (source and receiver) are parallel to each other and oriented in the radial (inline) direction.

- Transverse–Transverse (T–T) polarization.

The two transducers are parallel to each other and oriented in the transverse (crossline) direction.

- Radial–Transverse or Transverse–Radial (R–T or T–R) polarization.

The polarizations of the source and receiver transducers are perpendicular to each other.

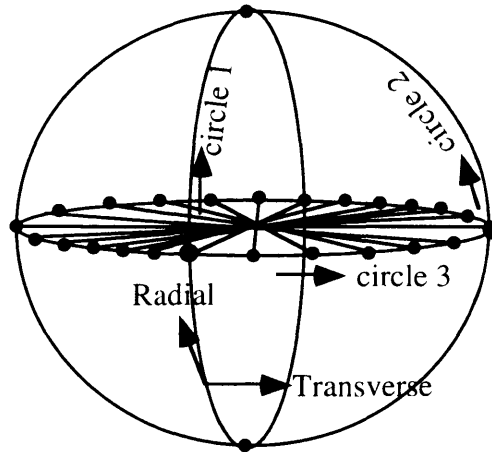


FIG. 4.13. Schematic diagram of the modelling geometry showing the layout of the sources and receivers; black dots represent transducer locations (sources and receivers). In each pair, the source receiver connected by a straight line. Sources and receivers were moved after the 'shot' was finished at one pair of locations (one diameter).

The theoretical curves of group velocities against ray angle are plotted in Figure 4.14 (calculated by applying the equations of Chapter 3). They represent velocities of the P wave first arrival and shear waves (SH and SV) versus ray angle.

The shear-wave transmission records along Circle 1 are plotted in Figure 4.15. Figure 4.15a is the plot with R–R transducer polarization. In the plot, the pattern of first arrivals is very similar to the SV curve in Figure 4.14. Figure 4.15b shows the shear-wave record for T–T polarization. There is not much time-shift of the first arrival and it is similar to the SH curve in Figure 4.14. A little first-arrival time-shift in some traces can be caused by the two transducer polarizations being nonparallel also Circle 1 is randomly selected and may not lie exactly on a symmetry plane. Similar results were obtained along Circles 2 (Figure 4.16a, b, and c) and 3. The shear-wave pattern shown in Figures 4.15 and 4.16 indicates that this type of salt probably exhibits cubic symmetry. Amplitudes are very low

on the shear-wave record with R-T (or T-R) polarization because of the low energy projection.

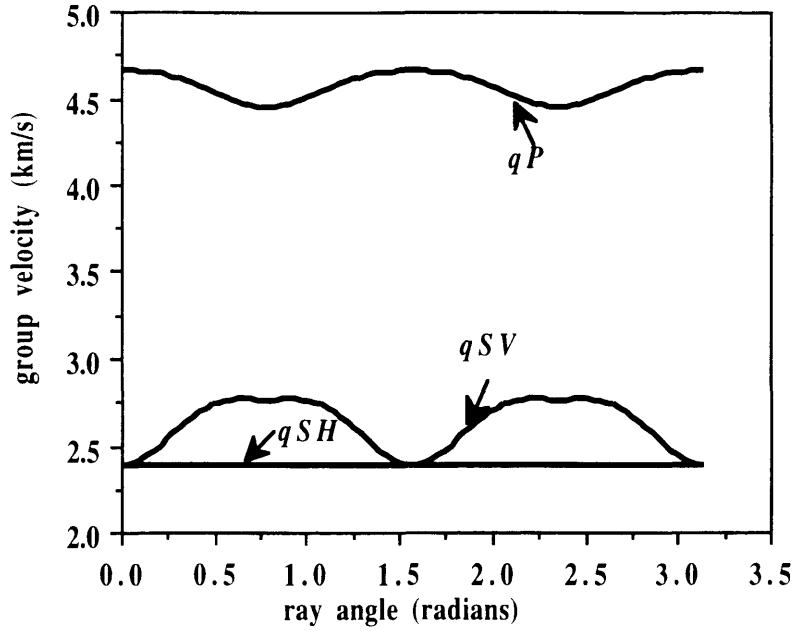


FIG. 4.14. Group velocities versus ray angle calculated from theoretical equations presented in Chapter 3.

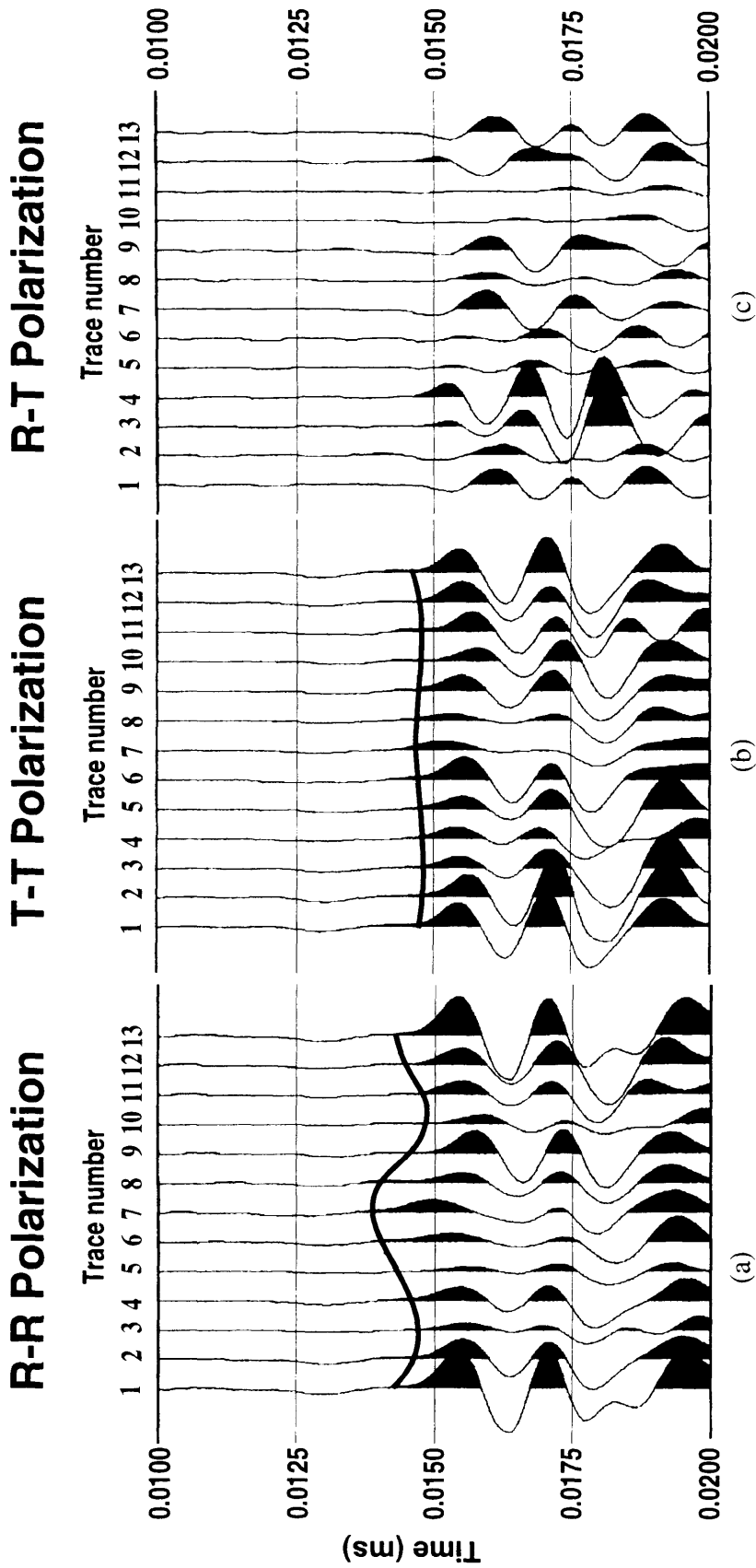


FIG. 4.15. Zero-offset shear transmission record over chevron-salt sphere along circle 1:
 a) R-R polarization; b) T-T polarization; c) T-R polarization

R-R Polarization T-T Polarization R-T Polarization

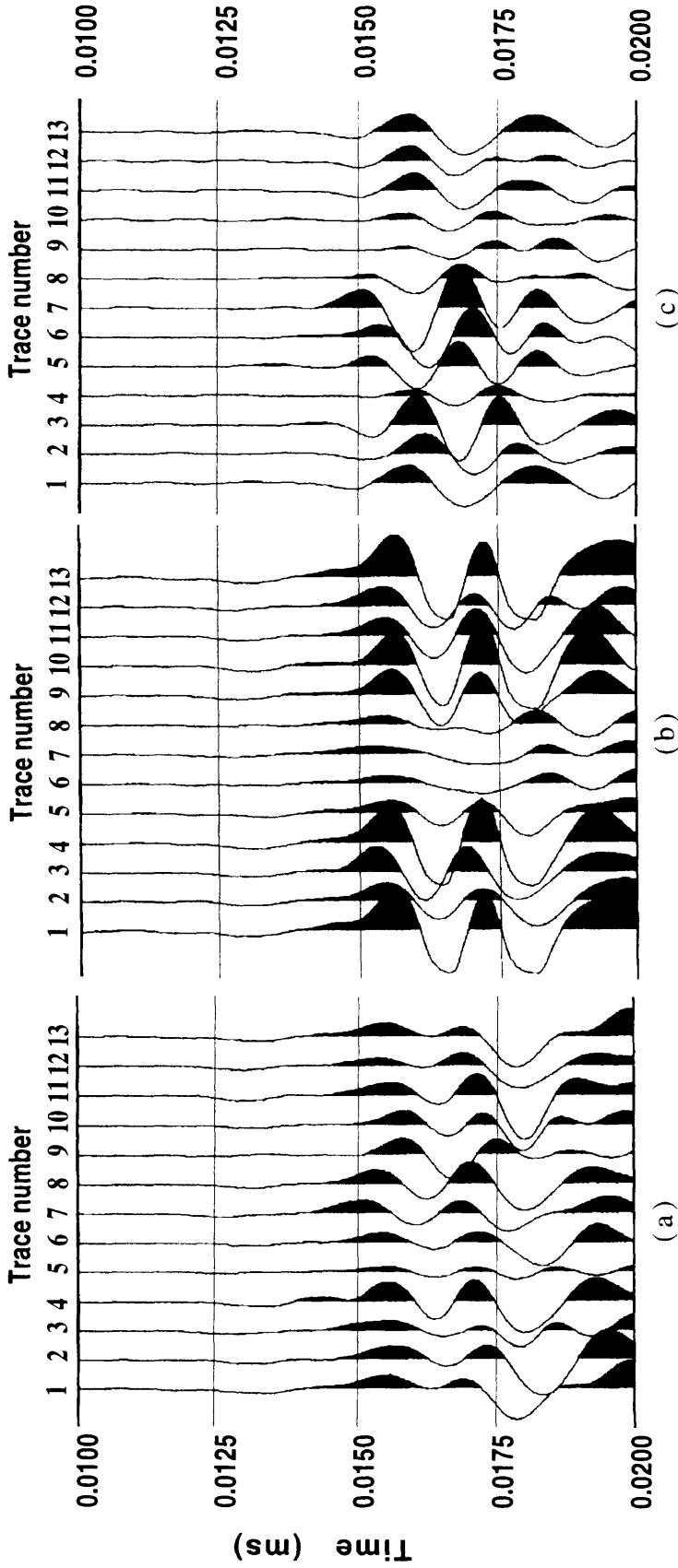
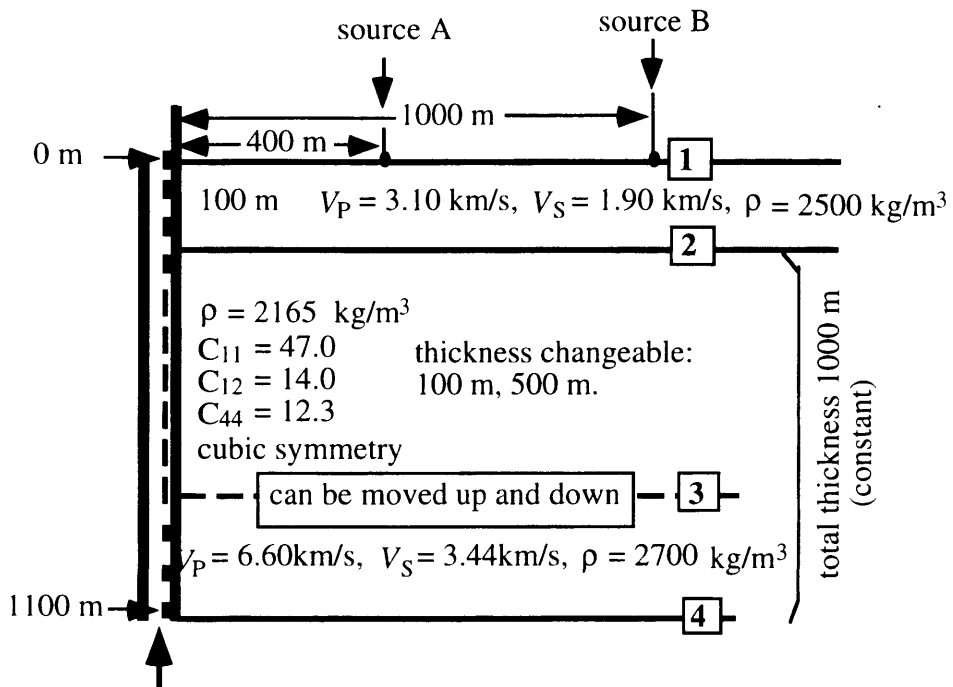


FIG. 4.16. Zero-offset shear transmission record over chevron-salt sphere along circle 2:
 a) R-R polarization; b) T-T polarization; c) T-R polarization

4.3 Numerical modelling with cubic salt

4.3.1 Model description

The geometry of the VSP experiment is schematically shown in Figure 4.17. Let us consider a Cartesian coordinate system in which the x axis, representing source offset, is the horizontal axis. The z axis is vertical and positive downward. The x axis is positive to the east (to the right on Figure 17).



Note: 111 receivers ranging from 0 m to 1100 m in increments of 10 m

Source A and source B are applied separately.

FIG. 4.17. Schematic diagram of VSP numerical model and model parameters with a layer of cubic anisotropic medium (layer 2).

The model consists of three layers separated by four interfaces (Figure 4.17). Interface 1 represents the free surface. Interface 2, the bottom of layer 1, is situated at $z = 100$ m depth. Interface 3, the bottom of layer 2, is situated at two different depths $z = 200$

m and $z = 600$ m due to the thickness change of layer 2. Interface 4, the bottom of layer 3, is situated at depth $z = 1100$ m. All the interfaces are assumed to be horizontal.

The first layer is homogeneous and isotropic with P- and S-wave velocities of 3.1 and 1.9 km/s, and a density of 2500 kg/m^3 .

The second layer is an anisotropic medium of cubic symmetry, namely salt. The elastic parameters are listed in Figure 4.17 (Sun et al., 1991) discussed in Chapter 3. Let us suppose that the salt cube is an upward-facing cube face (flat-topped), e.g. the x and z axes are on major symmetry axes.

Layer 3 is homogeneous and isotropic with P- and S-wave velocities of 6.6 km/s and 3.44 km/s respectively, and a density of 2700 kg/m^3 .

Three-component receivers are moved and located in the vertical borehole every 10 m covering the depth range from 0 to 1100 m for a total of 111 levels. The vertical component (V) is polarized parallel to the z axis, positive downward. The radial component is polarized parallel to the x axis, positive away from the source. The transverse component is polarized perpendicular to xz plane so that the system is right-handed.

Two locations of point sources at the free surface are considered (Figure 8). Source A and B are situated at coordinates (400, 0) and (1000, 0). Source offsets are 400 m and 1000 m. Single-force point sources of unit strength are considered but effects of the free surface at sources are not considered. Two different orientations of the single force were used: a radial force along the line connecting the source and the mouth of the borehole, pointing away from the source, and a transverse force perpendicular to the radial force and z axis and oriented so that the two forces and the z axis form a right-handed system. As a source time function, a Ricker wavelet with a dominant frequency of 50 Hz was used. The signal is approximately cosine shaped.

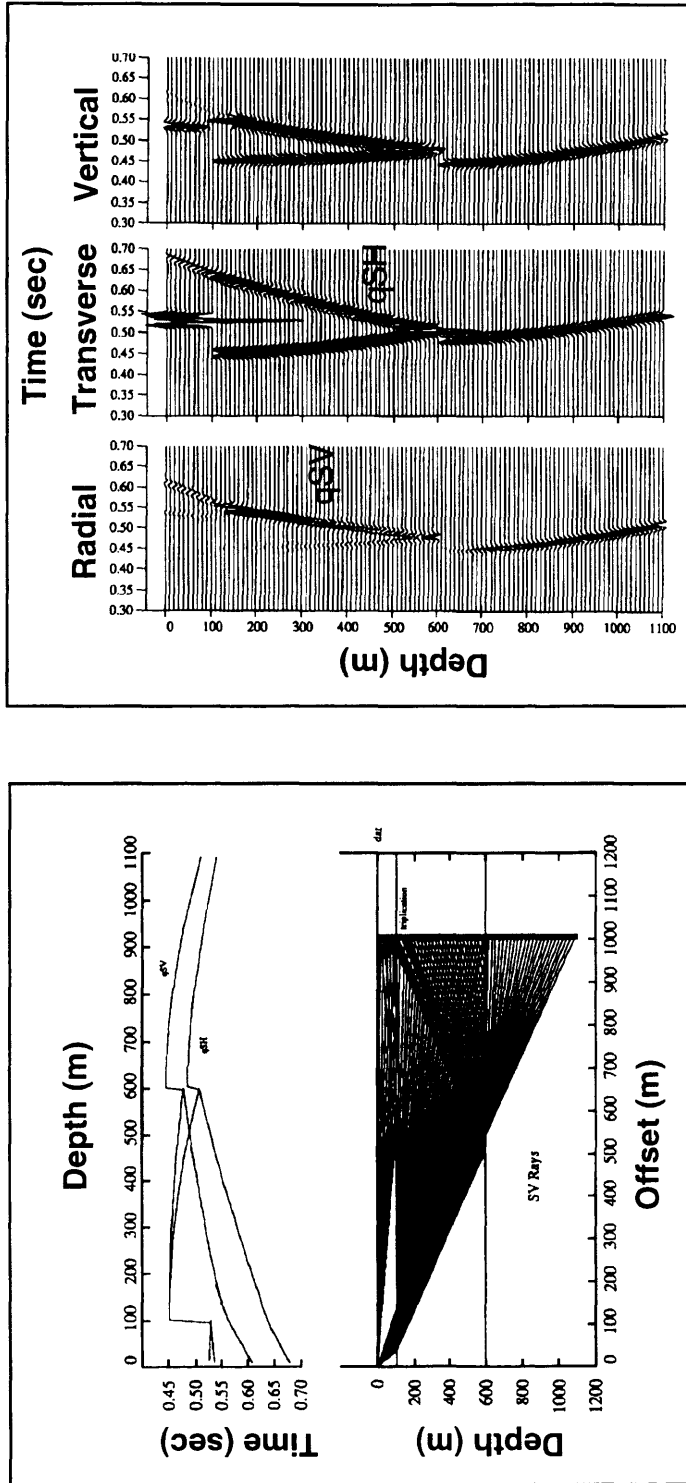
4.3.2 Analysis of VSP synthetic seismograms

All primary reflected unconverted waves, including direct waves, are considered by using the software package developed at Queen's University, Ontario, by Guest (1993). To show the effects of anisotropy, the following comparisons are made from synthetic seismograms computed for two different source locations with different layer-2 thicknesses.

- Same source location with different thickness of layer 2;
- Same thickness of layer 2 with different source location;
- Transverse shear source and radial shear source with same source location and same thickness of layer 2.

Figure 4.18a, 4.19a, and 4.20a show ray diagrams and time-distance curves. Interfaces are also plotted. The time-distance curves of qSV and qSH waves are specified. The wave propagating through layer 1 from the source to the receiver (located at the point where interface 2 intersects the borehole) takes more time than the wave propagating through layer 1 and 2 because the velocity of layer 2 is higher than that of layer 1. The same thing happens between layer 2 and layer 3. Therefore there are time-shifts at cross interfaces in all the time-distance curves (both qSV and qSH). Comparing Figure 4.18 with Figure 4.19, we can see that the larger the offset the more the time-shift. As evident from the time-distance curve and synthetic seismograms, the direct quasi-shear wave splits below 100 m, where the wave enters the anisotropic medium. The time difference between the slowest and fastest quasi-shear waves increases with the depth (Figures 4.18, 4.19, and 4.20). Comparison between Figures 4.18 and 4.19 indicates that the farther the source offset the better the shear-wave feature that can be seen. The source offset is not important when layer 2 (anisotropic layer) is thick enough in terms of observing shear-wave splitting (Figures 4.18 and 4.19). It is seen clearly from all the plots (Figures 4.18, 4.19, 4.20) that two shear waves are reflected back and transmitted into layer 3 from interface 3.

Multisource three-component VSP synthetics are shown in part (b) of all the above three figures. They contain three frames corresponding to the radial, transverse, and vertical components of receivers. There are three panels in parts (b) of Figures 4.18, 4.19, and 4.20. The right and left panels correspond to inline single-force point source; the middle panel corresponds to a transverse single-force point source. No amplitude power scaling is applied; true amplitudes are presented. There are no projections of energy into the transverse component when the radial shear source is applied. Therefore, in this case, converted shear waves from a P-wave source will not enable us to detect shear-wave splitting (two shear waves shown on the same plot can not be detected). Use of a shear source nonparallel to any symmetry direction is required in order to observe shear wave splitting.



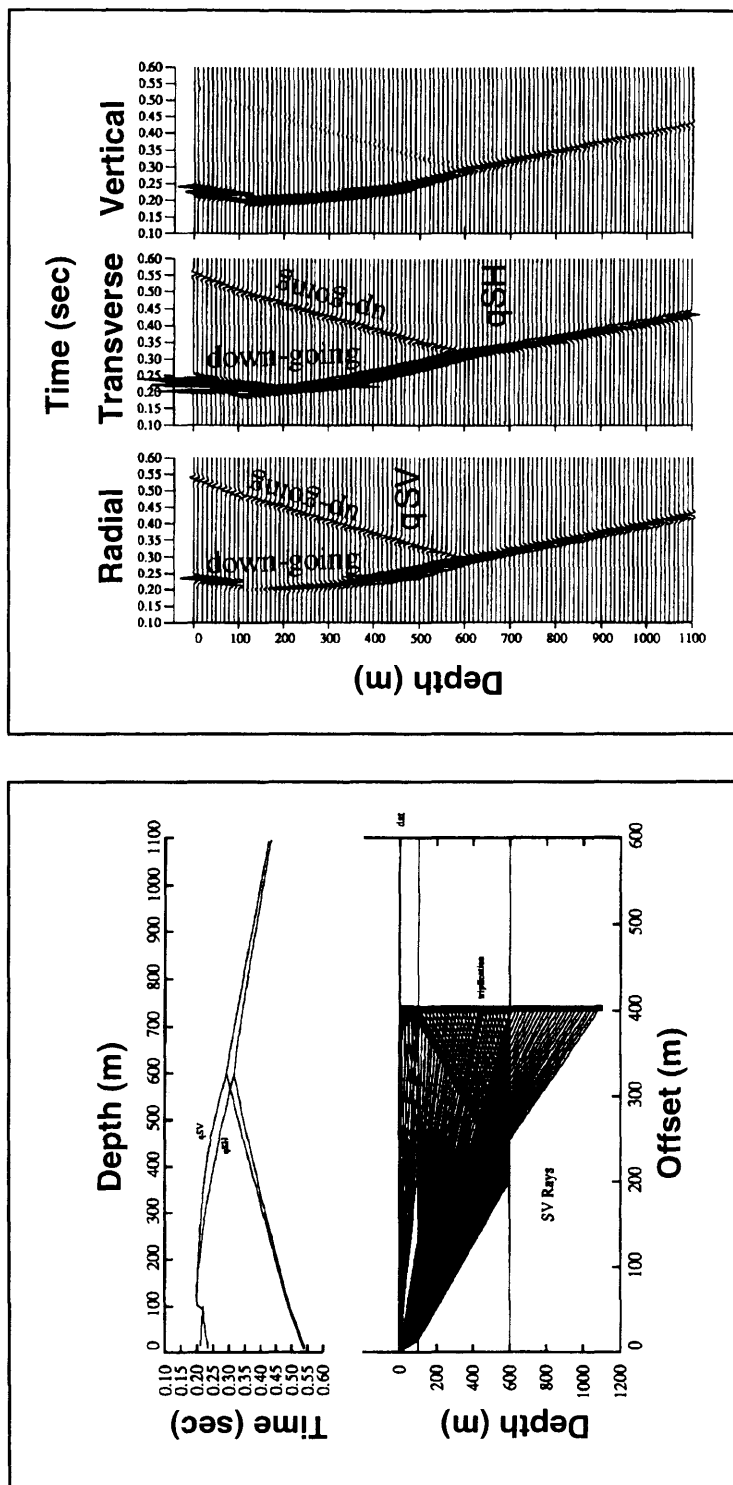
(a)

(b)

FIG. 4.18. Ray diagram, time-distance curves, multisource three-component synthetic seismograms generated by source B (1000 m offset) with 500 m salt thickness (layer 2).

(a) Ray diagram of SV source (bottom) and time-distance curves (top);

(b) VSP synthetics generated by shear sources at location B; shear-waves recorded on the radial and vertical component (left and right panel) were generated by a radial (inline) shear source; shear-wave recorded on the transverse component (middle panel) was generated by a transverse (crossline) shear source.



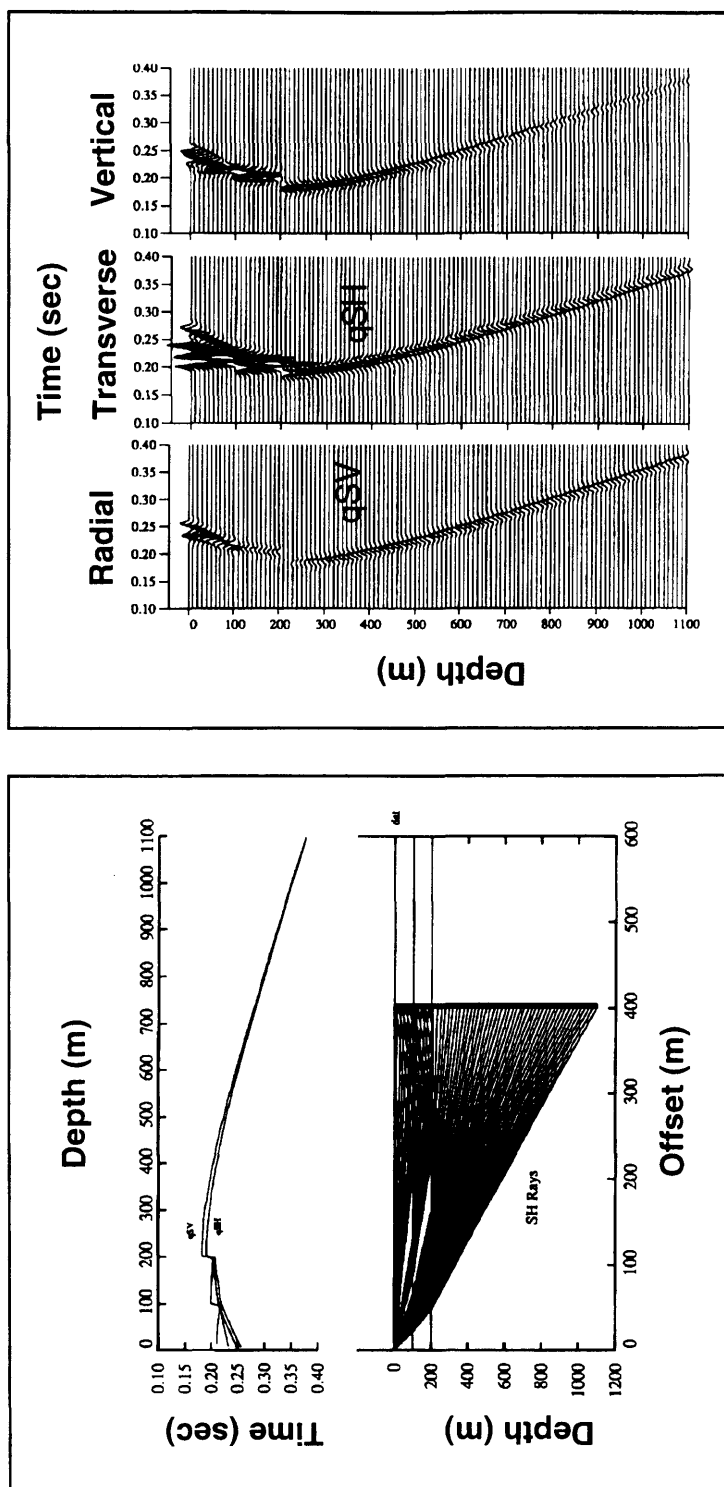
(a)

(b)

FIG. 4.19. Ray diagram, time-distance curves, multisource three-component synthetic seismograms generated by source B (400 m offset) with 500 m salt thickness (layer 2).

(a) Ray diagram of SV source (bottom) and time-distance curves (top);

(b) VSP synthetic seismograms generated by shear sources at location A; shear-waves recorded on the radial and vertical component (left and right panel) were generated by a radial (inline) shear source; shear-wave recorded on the transverse component (middle panel) was generated by a transverse (crossline) shear source.



(a)

(b)

FIG. 4.20. Ray diagram, time-distance curves, multisource three-component synthetic seismogram generated by source A (400 m offset) with 100 m salt thickness (layer 2).
 (a) Ray diagram of SV source (bottom) and time-distance curves (top);
 (b) VSP synthetic seismograms generated by shear sources at location A; shear-waves recorded on the radial and vertical component (left and right panel) were generated by a radial (inline) shear source; shear-wave recorded on the transverse component (middle panel) was generated by a transverse (crossline) shear source, showing difficulties to see shear-wave splitting.

Chapter 5 - Three-component seismic anisotropy experiment around a salt pillar

5.1 Introduction

Because of the important roles played by salt in various exploration scenarios, and because salt crystals (halite, sylvite, etc.) have cubic symmetry and are therefore elastically anisotropic, we have been considering the possibility of using the diagnostic properties of this seismic anisotropy (such as shear-wave splitting) as an additional tool for mapping salt, in combination with the traditional well-logging tools – mainly calipre and gamma-ray logs. In order that salt units exhibit such diagnostic properties for frequencies of relevance to exploration ($f \sim 10\text{--}10^2$ Hz), salt crystals would have to be aligned throughout certain volume so that shear-wave splitting can be seen. As we have observed, some salt core samples (related to certain salt types) have been found to exhibit shear-wave splitting (Chapter 4) in ultrasonic laboratory experiments ($f \sim 10^5\text{--}10^6$ Hz).

This chapter represents a new step, i.e. to see whether in-situ salt might exhibit observable seismic anisotropy in the so-called high-resolution frequency range ($f \sim 10^3$ Hz), closer to that of exploration. In order to study possible seismic anisotropy due to crystal alignment in salt, in-situ experiments were carried out in the Devonian Prairie Evaporite about one kilometre underground in the Allan Potash Mine, near Saskatoon, Saskatchewan. The work was carried out using a high-resolution ($\sim 1\text{-kHz}$) seismic acquisition system and a tomographic (transmission) type of experimental design. The main purpose of the study was to establish whether or not the anisotropic seismic properties of these salts, which are believed to have undergone several episodes of recrystallization and thermomechanical alteration, show any promise of being useful in the mapping of such salt units.

5.2 The high-resolution experiment

A pillar of potash ore (roughly 75% halite and 25% sylvite) was selected for the experiment on the basis of accessibility and rock integrity. A hammer was employed as the energy source (frequencies from about 100 to 2000 Hz) and each record was obtained by vertically stacking the records from five repeated hammer blows. Geophones were affixed to one face of the pillar in three orthogonal orientations. Records were acquired in three separate steps, each with identical geometry but different orientations of the geophone polarization: first normal to the wall, then vertically tangential to the wall, and finally horizontally tangential.

The high-resolution three-component experiment was carried out in the Allan Mine of the Potash Corporation of Saskatchewan, about 40 km southeast of Saskatoon. Keeping salt classification in mind, I observed the salt to be recrystallized and thermomechanically altered. Stratigraphically, it is located in a main production zone of the Patience Lake Member of the Devonian Prairie Formation (Figure 5.1). The pillar consists entirely of recrystallized salt that has undergone some metamorphism and alteration by pressure and temperature.

Experiments were conducted in a mining pillar that was chosen as being freshly excavated and as free of deformation (fracture, flow) as possible. However, deformation begins immediately after excavation so some is unavoidable. A plan view of the pillar is shown in Figure 5.2. High-frequency geophones were attached rigidly to the wall with a small steel bracket. The geophone was screwed to one end of the bracket, which was fixed to the rock with a fastener. Fasteners are threaded Hilti bolts that were driven into the rock salt with a gun using explosive cartridges.

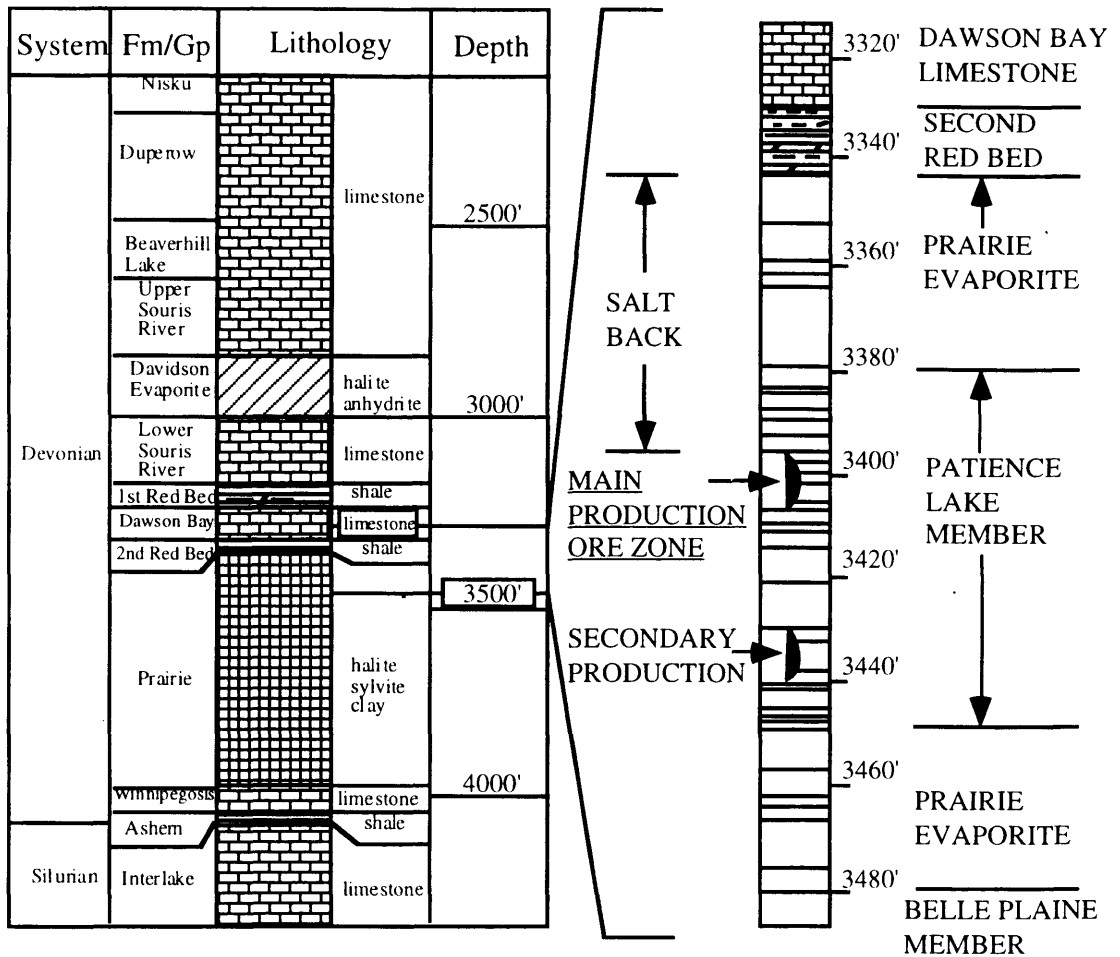


FIG. 5.1. A stratigraphic section of the mining zone, the experiments were carried out in the main production ore zone.

The data were sampled every 0.05 ms and recorded to a length of 50 ms by a 24-channel Bison GeoPro seismograph. Field parameters are listed in Table 5.1. There were 29 shot positions and each shot was recorded simultaneously with 23 receivers that were affixed to the northern part of the west wall at 0.5-m intervals. The sources were positioned over the rest of the pillar at 2-m intervals (Figure 5.2). Five hammer blows were struck at each source location for each component. Both receivers and sources were kept at the same height. The experimental procedure was as follows:

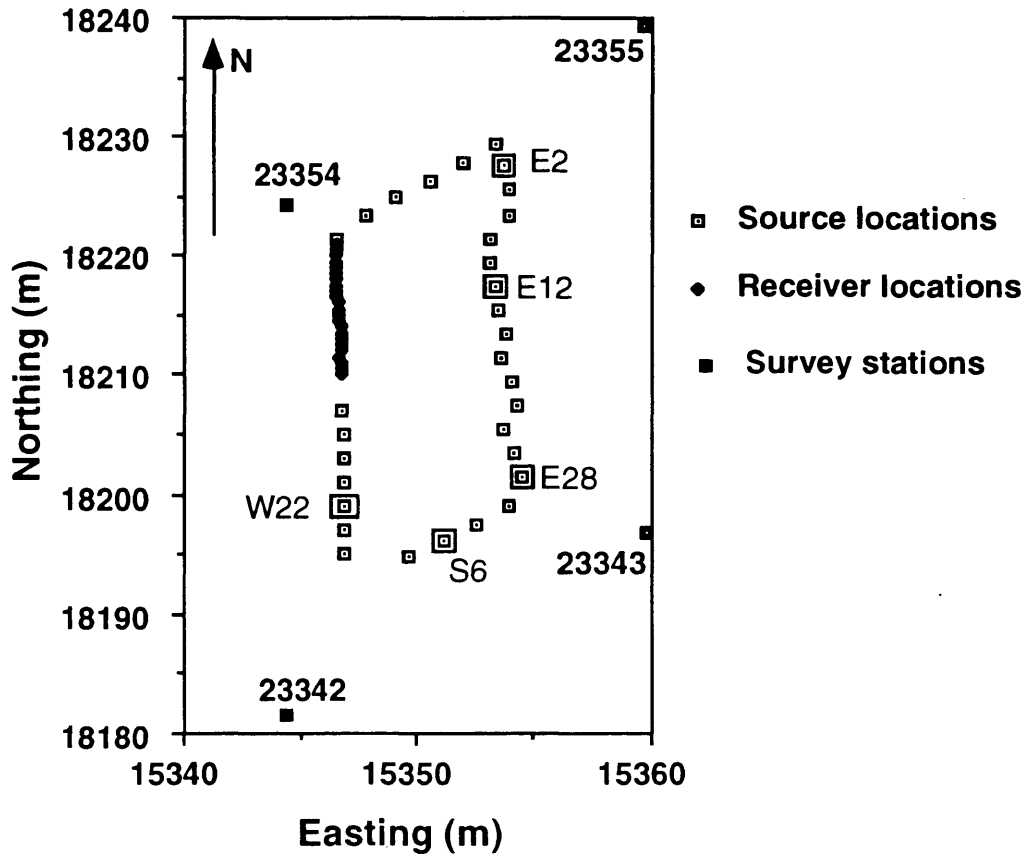


FIG. 5.2. Plan view of the experimental salt pillar showing source and receiver locations and mine-survey stations. Three-component record sets are displayed below for the highlighted source locations.

Table 5.1. Field recording parameters for all experiments.

Filters:	high-cut: 2000 Hz	low-cut: 96 Hz
Sample rate:	0.05 ms	
Channels:	24	
Samples:	1001	
Recording length:	50 ms	
AGC:	off	

- 1) shots around all four sides of the pillar were recorded with geophone polarizations normal to the pillar, denoted N;
- 2) the geophone polarizations were changed to tangential-vertical (crossline, upward), denoted V – everything else unchanged – and the shot series was repeated;
- 3) the geophone polarizations were changed to tangential-horizontal (inline, southward), denoted H, and the shot series was carried out a third time.

Thus, for each of the 29 shots, three-component transmission records were acquired representing propagation through the salt pillar. These records have been analyzed for evidence of shear-wave splitting. In such analysis the peculiar geometry of this survey must be kept in mind (a horizontal line on a vertical rock face) compared with that of conventional reflection-seismic geometry. Here, the sagittal plane is horizontal rather than the conventional vertical; geophones recording horizontal motion normal to the pillar face (N) correspond to the conventional vertical-component phones; geophones recording vertical motion tangential to the pillar face (V) correspond to the conventional transverse or crossline horizontal-component phones, and geophones recording horizontal motion tangential to the pillar face (H) correspond to the conventional radial or inline horizontal-component phones.

There is a clear relationship between polarities on the N and H components for P and SV waves, depending on where the shotpoint was located. However, there is no such clear relationship between polarities on the V and H (or the V and N) components since, *ideally* our hammer blows should not have any net vertical component of force. For this reason, in the absence of very clear first S-wave breaks, there would be some ambiguity in correlating S1 (on N and H) with S2 (on V) for the purpose of determining split-shear time delays: one could, for example, correlate an S1 peak on N with either a peak or a trough of S2 on V.

5.3. Results and interpretation

If seismic anisotropy is observed in this rockmass, there are two possible causes that seem most likely. One candidate is the alignment of salt crystals, which would have occurred during recrystallization under the control of the prevailing stress regime. Another is the microcracking and fracturing that evidently initiates throughout the neighbourhood of the exposed rock faces immediately following excavation. This would be in response to the sudden release of compressive stress normal to each excavated surface (horizontal and vertical surfaces in most mines), giving rise to cracks with accordingly preferred orientations. In the former case, one would expect symmetry directions of the anisotropy to conform to those of the prevailing principal stresses. In the latter case, one would expect these symmetry directions to conform with the normals to the excavated rock faces. In either case we would expect the horizontal plane to be a plane of symmetry, i.e. the vertical direction to be a direction of symmetry, in view of the presumed maximum principal stress due to gravity and the horizontal/vertical nature of the mine cuts. We would, however, expect the two scenarios to give, in general, different horizontal symmetry directions.

Recall that the slownesses and group velocities in halite for qS and qP waves propagating in a symmetry plane of halite (Figures 3.5, and 3.6, Chapter 3), presumably the horizontal sagittal plane of our experiment. Because of the unconventional geometry of this survey, the shear waves normally thought of as SV, polarized within the plane of propagation, are here polarized horizontally; and the shear waves normally thought of as SH, polarized transversely to the plane of propagation, are here polarized vertically. We therefore look for the fast shear waves, qS1 (qSV), on the N- and H-component geophones, and the slow shear waves, qS2 (qSH), on the V-component geophones.

In examining the records obtained in this survey, we find significant shear-wave splitting for many of the shot-receiver directions and little or no splitting for others.

Figures 5.3 to 5.7 show the three-component records acquired for five different shot locations: S-6 (south wall, shotpoint 6), E-12, W-22, E-2 and E-28. The positions of these shots are indicated in Figure 5.2. Note that propagation through the entire spread covers a range of directions. The first two of these shotpoints, S-6 and E-12 (Figures 5.3 and 5.4), have been chosen as record sets showing the least shear-wave splitting, whereas the remaining three, W-22, E-2 and E-28 (Figures 5.5 to 5.7), have been chosen as record sets showing more-or-less maximum splitting.

Directions of no splitting correspond to symmetry directions (see Figure 3.4) so this observed pattern indicates symmetry directions roughly ENE-WSW and NNW-SSE. These do not correspond to the roughly N-S and E-W symmetry of the recording wall, but do concur quite well with directions reported in the literature for observed fracture lineament trends and for the stress regime in the western Canada basin. The observed pattern of shear-wave splitting as a function of direction appears to be incompatible with the hypothesis of excavation stress release as the cause, but quite compatible with the hypothesis of crystal alignment controlled by the prevailing stress field.

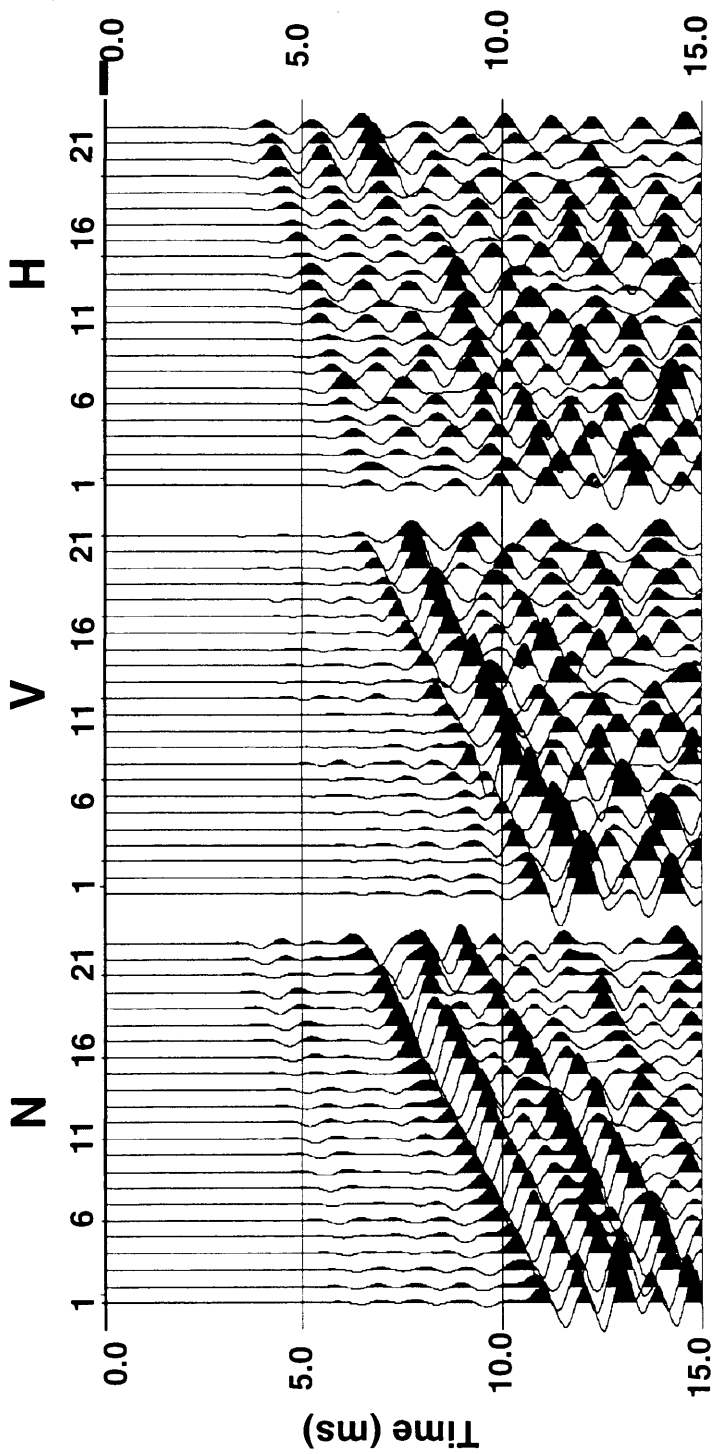


FIG. 5.3 Three-component record set for the shotpoint at S-6, i.e. south wall, shot location 6. There is little or no shear-wave splitting observed.

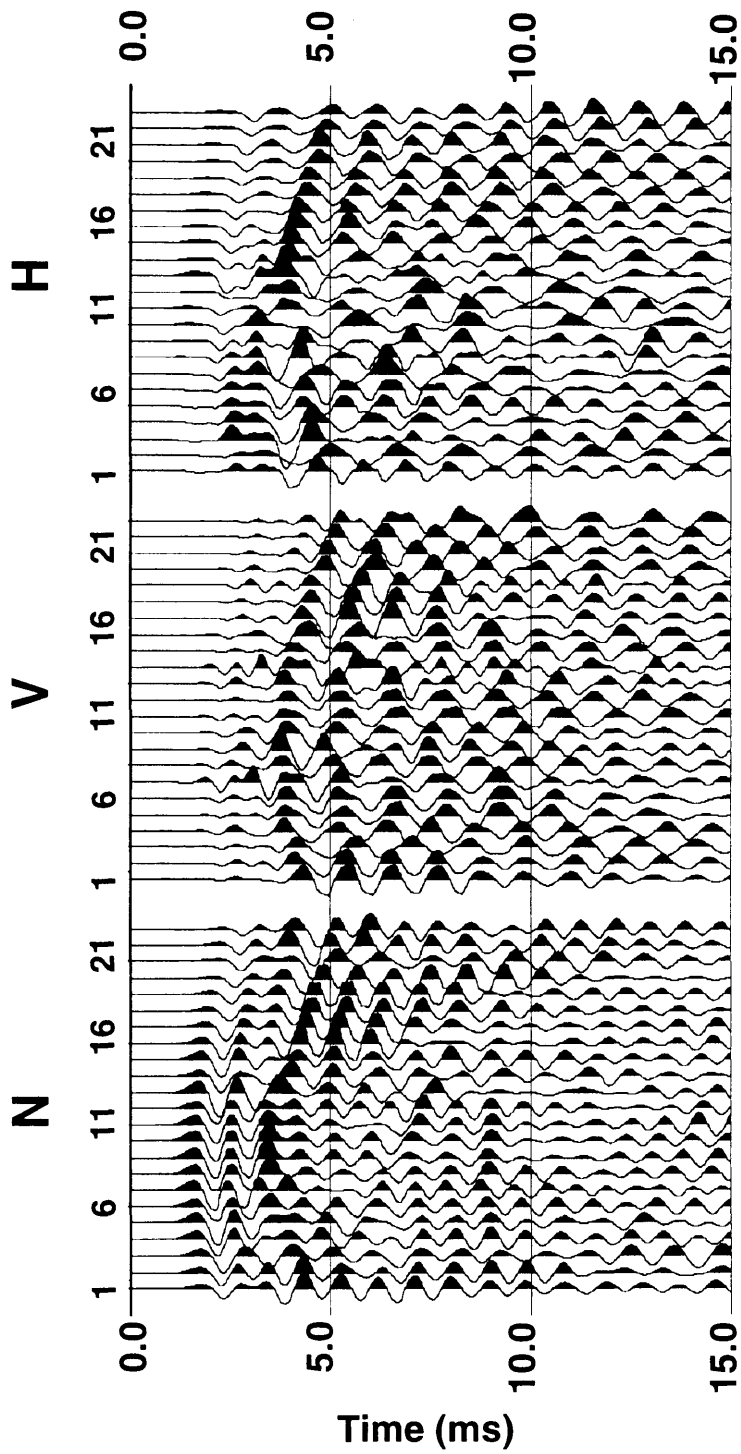


FIG. 5.4. Three-component record set for shotpoint at E 12, i.e. east wall, shot location 12. There is no obvious shear-wave splitting observed particularly on the farthest offsets.

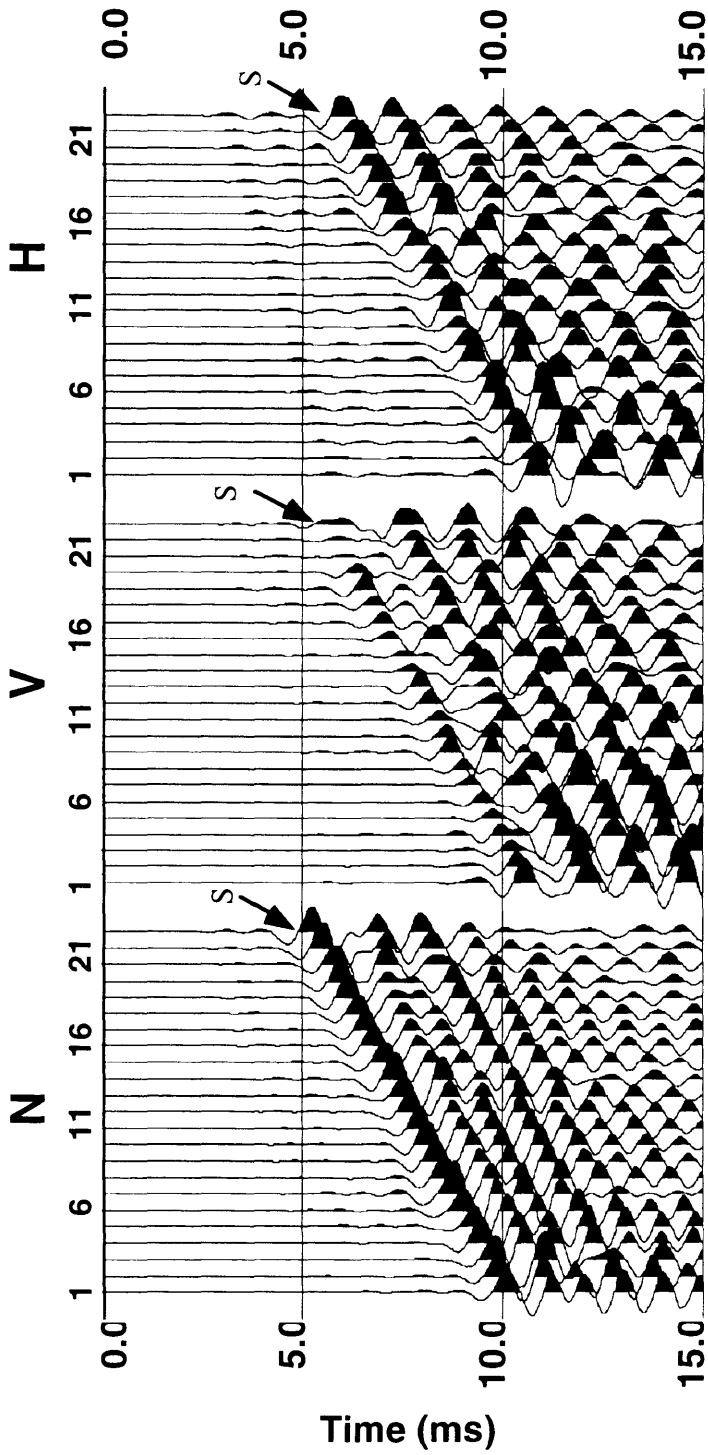


FIG. 5.5. Three-component record set for the shotpoint at W 22, i.e. west wall, shot location 22. there appears to be significant shear-wave splitting on all traces.

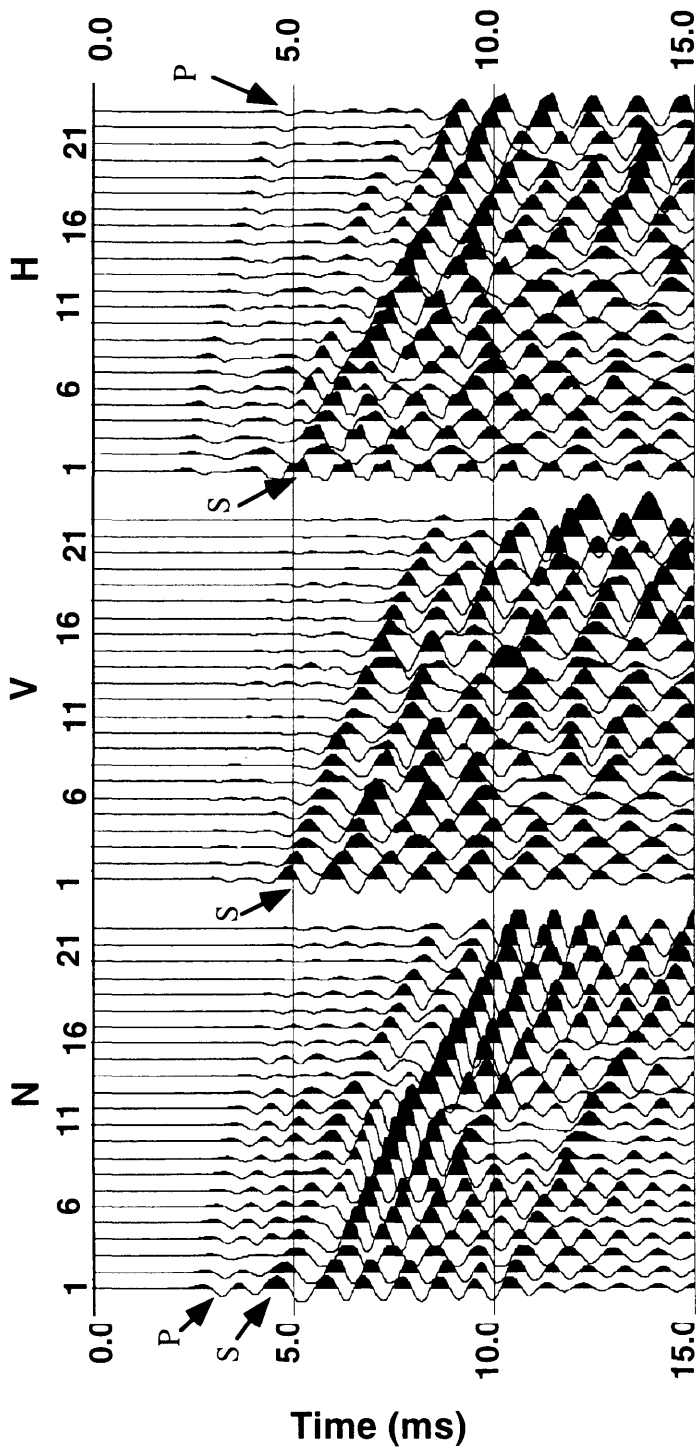


FIG. 5.6. Three-component record set for the shotpoint at E 2, i.e. east wall, shot location 2. There appears to be significant shear-wave splitting on all traces.

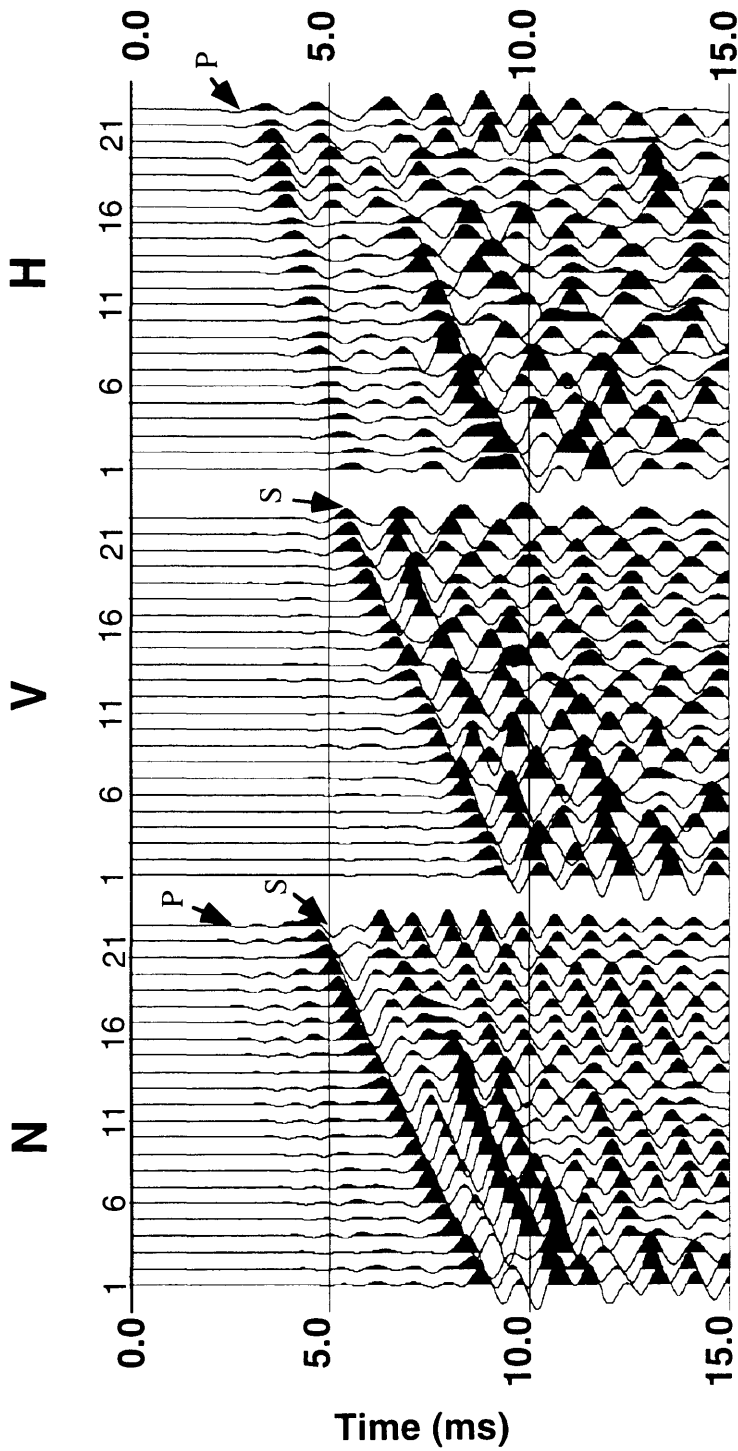


FIG. 5.7. Three-component record set for the shotpoint at E 28, i.e. east wall, shot location 28. There appears to be significant shear-wave splitting on all traces.

Among published studies on the western Canadian plains, Stauffer and Gendzwill (1987) document orthogonal fracture sets, consistently trending NE-SW, that they interpret as having originated in the Late Jurassic or earlier and to be related to North American plate motion. Also, Mollard (1988) reported on the results of several studies on the orientation of fracture lineaments and principal stress axes using a wide array of observations: remote sensing, photolineaments, joint sets, principal stresses from mines and from oil-well breakouts, and inferred tectonic plate motion. These studies all indicate directions close to NE-SW and NW-SE, with the inferred direction of contemporary maximum horizontal compressive stress varying locally over the plains from ENE to NNE.

I have found the hammer-impact source to be quite effective in producing shear waves, in some cases even of greater amplitude than the P waves. This effect has also been observed by D.J. Gendzwill (pers. comm.). The records shown in Figures 5.3 to 5.7 also contain spurious resonances, which could be removed by designing appropriate deconvolution filters. This ringing also contributes to the ambiguity in correlating S1 and S2, as mentioned above. Nevertheless, the compressional- and shear-wave arrivals are clear enough for one to conclude with some confidence that significant time delays exist in Figures 5.5 to 5.7 between the S1 arrivals seen on the normal (N) and the inline (H) components and the S2 arrivals observed on the crossline (V) components.

5.4 Discussion

The recrystallized and thermomechanically altered salt studied in this experiment appears to exhibit seismic anisotropy. The symmetry axes of the anisotropy appear to be consistent with a cause rooted in the alignment of salt crystals, perhaps of the recrystallized and thermomechanically altered salt type. This is in accord with our expectation, on the basis of salt classification, that this type of salt could display elastic anisotropy, depending on the degree and type of alteration. The cracking and fracturing

resulting from the mine excavation appears not to have been a significant factor in the observed anisotropy. This is in agreement with the findings of Holmes et al. (1993) who observed less effect on shear-wave signals from excavation damage than from long-standing stress-controlled rock fabric in an experiment in the Underground Research Laboratory of Atomic Energy of Canada Ltd at Pinawa, Manitoba.

Chapter 6 - Conclusions

This thesis has started to study a relatively new realm of seismic anisotropy – cubic symmetry, and tried to extend research results to salt mapping. Salts first were classified in terms of velocity characteristics and possibility of seismic anisotropy. Both P-wave and S-wave velocities were measured under different pressure and temperature conditions for different types of salt. Theoretical studies can provide prediction of anisotropic characteristics of cubic symmetry. Considerable evidence concerning salt anisotropy has been collected through physical modelling experiments, followed by numerical modelling, both of which can help us to understand and identify shear-wave splitting. A field 3-C study has indicated that the symmetry axes of the anisotropy of a salt pillar appear to be consistent with a cause rooted in the alignment of salt crystals instead of resulting from the mine excavation.

The study of Chapter 2 has shown that there are at least three types of anisotropic salt, chevron-salt, highly recrystallized salt in a stable environment, and thermomechanically altered salt. A metamorphic salt layer may exhibit moderate anisotropy, weak anisotropy, or isotropy depending on the geological process that the salt has experienced. Anisotropic behaviour can accompany the texture in salt domes resulting from thermomechanical strain and alteration. Basically, the velocities observed in the laboratory are probably close to those in the subsurface because the P-wave and S-wave velocities exhibit only a slight increase with increasing pressure and a slight decrease with increasing temperature. However, the V_p/V_s pattern of impure salt or mixtures of pure halite and sylvite is very different from that of pure halite; the former shows first an increase and then a decrease around 1 - 2 kpsi while the latter always shows a V_p/V_s decrease.

Phase- and group-velocity formulae have been developed for cubic symmetry and can be applied to any medium with cubic symmetry. Theoretically, except on symmetry axes, shear-wave splitting can be observed. The maximum shear-velocity difference is in

the (1,1,0) direction (halfway between symmetry axes). The P-wave velocity is also slowest in this direction.

Physical modelling study shows that the shear-wave properties of chevron-crystal salt fit the assumption of cubic anisotropy well. It further proves that chevron-salt, highly recrystallized salt, and thermomechanically altered salt are anisotropic. The maximum velocity difference between fast-shear- and slow-shear-wave velocities is 20% observed from a large pure salt crystal, and around 5% observed from cores in the laboratory. Impure salt shows isotropic behaviour. An offset transmission experiment indicates that shear-wave splitting can be identified on offset time sections. The first-arrival times are not hyperbolic and the amplitude of the split shear-waves usually overlap and interfere with each other, which generally makes shear-wave data analysis complicated in anisotropic media. Far-offset shear-wave observation is limited due to the characteristics of the radiation patterns of the transducers.

The VSP numerical modelling over a salt layer has shown that the greater the source offset the better the shear-wave features that can be observed. Shear-wave splitting cannot be observed on P-SV data if the receivers are on one of the symmetry axes.

According to the result above, shear-wave seismic data may be useful in detecting and mapping salt. We can expect shear-wave anisotropy from 0 to 20%. In order to generate a 5-ms time shift between split shear waves, a thickness of about 125 m of salt (~63 m for two-way time) is required if salt anisotropy is about 10%. For an effective anisotropy of about 5%, as observed on laboratory samples, these thicknesses would become ~250 m and ~125 m respectively. The first figure would be appropriate in a P-SV converted-wave survey.

A so-called high-resolution experiment (frequency range $f \sim 10^3$ Hz) was carried out and showed that the recrystallized and thermomechanically altered salt studied in this experiment appears to exhibit seismic anisotropy. The symmetry axes of the anisotropy appear to be consistent with a cause rooted in the alignment of salt crystals, perhaps of the

recrystallized type. This is in accord with our expectation, on the basis of salt classification, that this type of salt could display elastic anisotropy, depending on the degree and type of alteration. The cracking and fracturing resulting from the mine excavation appears not to have been a significant factor in the observed anisotropy. This is in agreement with the findings of Holmes et al. (1993) who observed that only a secondary effect of excavation damage on shear-wave signals in an experiment in the Underground Research Laboratory of Atomic Energy of Canada Ltd at Pinawa, Manitoba.

References

- Anderson, N.L., 1991, Dissolution of the Wabamun Group salt: Exploration implications, *in* Cavanaugh, T.D., ed., Integrated exploration case studies, North America: Geophys. Soc. Tulsa, 179-209.
- Anderson, N.L. and Brown, R.J., 1991a, Reconstruction of the Wabamun Group salt, southern Alberta, Canada, *in* Cavanaugh, T.D., ed., Integrated exploration case studies, North America: Geophys. Soc. Tulsa, 143-177.
- Anderson, N.L. and Brown, R.J., 1991b, A seismic analysis of Black Creek and Wabamun salt collapse features, western Canadian sedimentary basin: Geophysics, **56**, 618–627.
- Backus, G.E., 1965, Possible forms of seismic anisotropy of the uppermost mantle under oceans: *J. Geophys. Res.*, **70**, 3429–3439.
- Berryman, J.G., 1979, Long-wave elastic anisotropy in transversely isotropic media: Geophysics, **44**, 896–917.
- Brown, R.J., Lawton, D.C. and Cheadle, S.P., 1991, Scaled physical modelling of anisotropic wave propagation: multioffset profiles over an orthorhombic medium: *Geophys. J. Int.*, **107**, 693-702.
- Casas, E., Lowenstein, T.K., Spencer, R.J. and Zhang, P., 1992, Carnallite mineralization in the nonmarine, Qaidam basin, China: Evidence for the early diagenetic origin of potash evaporites: Unpublished research paper.
- Cheadle, S.P., Brown, R.J. and Lawton, D.C., 1991, Orthorhombic anisotropy: A physical seismic modeling, Geophysics, **56**, 1603-1613.
- De Mille, G., Shouldice, J.R. and Nelson, H.W., 1964, Collapse structures of the Prairie Formation, Saskatchewan: *Bull. Geol. Soc. Am.*, **75**, 307-316.
- Eaton, D.W.S. and Stewart, R.R., 1990, 2^{1/2} D elastic ray-Born migration/inversion theory for transversely isotropic media. CREWES Project Res. Report 2.

- Edmunds, R.H., 1980, Salt removal and oil entrapment: *Can. Soc. Petr. Geol., Mem.*, **6**, 988.
- Gardner, G.H.F., Gardner, L.W. and Gregory, A.R., 1974, Formation velocity and density – the diagnostic basics for stratigraphic traps: *Geophysics*, **39**, 770-780.
- Geis, W. T., Stewart, R. R., Jones, M. J., and Katapodis, P. E., 1990, Processing, correlating, and interpreting converted shear waves from borehole data in southern Alberta: *Geophysics*, **55**, 660-669.
- Guest, W. S. 1993, Reflection, transmission, and conversion of elastic wave in inhomogeneous anisotropic media: theory and application to crustal seismic survey: Ph.D. thesis, Queen's Univ., Kingston, Ontario.
- Hardie, L.A. and Eugster, H.P., 1971, The depositional environment of marine evaporites: a case for shallow, clastic accumulation: *Sedimentology*, **16**, 187-220.
- Helbig, K., 1994, Foundations of anisotropy for exploration seismics, Pergamon.
- Holmes, G.M., Crampin, S. and Young, R.P., 1993, Preliminary analysis of shear-wave splitting in granite at the Underground Research Laboratory, Manitoba: *Can. J. Expl. Geophys.*, **29**, 140-152.
- Hopkins, J.C., 1987, Contemporaneous subsidence and fluvial channel sedimentation: Upper Mannville C pool, Berry field, Lower Cretaceous of Alberta: *AAPG Bull.*, **71**, 334-345.
- Jenyon, M.K., 1988, Seismic expression of salt dissolution-related features in the North Sea: *Bull. Can. Petr. Geol.*, **36**, 274-283.
- Jenyon, M.K. and Taylor, J.C.M., 1987, Dissolution effects and reef-like features in the Zechstein across the Mid North Sea High, *in* Peryt, T.M., ed., *The Zechstein facies in Europe*: Springer-Verlag, 51-75.
- Kendall, J-M., and Thomson, C.J., 1989, A comment on the form of the geometrical spreading equations, with some numerical examples of seismic ray tracing in inhomogeneous, anisotropic media: *Geophys. J. Int.*, **99**, 401-413.

- Langstroth, W.T., 1971, Seismic study along a portion of the Devonian salt front in North Dakota: *Geophysics*, **36**, 330-338.
- Larsen, J.G., 1983, New methods in textural and fabric analysis of rock salt related to mechanical test data, Tostrup salt dome, Demark: **6th Internat. Symp. Salt, Salt Inst. Vol. 1**, 323-330.
- Lohmann, H.H., 1972, Salt dissolution in subsurface of British North Sea as interpreted from seismograms: *AAPG Bull.*, **56**, 161-168.
- Lowenstein, T.K., 1982, Primary features in a potash deposit: The Permian HanSalado Formation of west Texas and New Mexico, in Handford, C.R., Loucks, R.G., and Davies, G.R., eds., *Depositional and Diagenetic Spectra of Evaporites – A core workshop: Soc. of Econ. Paleontol. and Mineral., Core Workshop No. 3*, Calgary, 276-304.
- Lowenstein, T.K., 1988, Origin of depositional cycles in a Permian “ saline giant”: The Salado (McNutt Zone) evaporites of New Mexico and Texas: *Geol. Soc. of America, Bull.*, **100**, 592-608.
- Lowenstein, T.K. and Hardie, L.A., 1985, Criteria for recognition of salt-pan evaporites: *Sedimentology*, **32**, 627-644.
- Masters, J.A., 1984, 'Elmworth' Case Study of a Deep Basin Gas Field: *AAPG Mem.* **38**.
- Meijer Drees, N.C., 1986, *Evaporitic Deposits of Western Canada: Geol. Surv. Can., Paper 85-20*.
- Miller, G.F., and Musgrave, M.J.P., 1956, On the propagation of elastic waves in aeolotropic media. III. Media of cubic symmetry: *Proc. Roy. Soc., A*, **236**.
- Mollard, J.D., 1988, Fracture lineament research and applications on the western Canadian plains: *Can. Geotech. J.*, **25**, 749-767.
- Musgrave, M.J.P., 1970, *Crystal Acoustics: Holden-Day, San Francisco*.
- Oliver, T.A. and Cowper, N.W., 1983, Wabamun salt removal and shale compaction

- effects, Rumsey area, Alberta: *Bull. Can. Petr. Geol.*, **31**, 468-482.
- Parker, J.M., 1967, Salt solution and subsidence structures, Wyoming, North Dakota and Montana: *AAPG Bull.*, **51**, 1929-1947.
- Postma, G.W., 1955, Wave propagation in a stratified medium, *Geophysics*, **20**, 780-806.
- Radovich, B.J. and Levin, F.K., 1982, Instantaneous velocities and reflection times for transversely isotropic solids: *Geophysics*, **47**, 316-322.
- Schaller, W.T. and Henderson, E.P., 1932, Mineralogy of drill cores from the potash field of New Mexico and Texas: *US Geol. Surv., Bull.*, **833**, 124.
- Schwerdtner, W.M., 1966, Intragranular gliding in domal salt: *Tectonophysics*, **5**, 353-380.
- Simpson, F., 1984, Potential for additional hydrocarbon recovery from the Colorado and Montana Groups (Cretaceous) of Saskatchewan: *Sask. Geol. Soc., Spec. Publ. no. 7*, 211-244.
- Skrotzki, W. and Welch, P., 1983, Fibre textures in extruded salt: **6th Internat. Symp. Salt, Salt Inst. Vol. 1**, 315-321.
- Smith, D.G. and Pullen, J.B., 1967, Hummingbird structure of south-east Saskatchewan: *Bull. Can. Soc. Petr. Geol.*, **15**, 468-482.
- Spencer, R.J. and Lowenstein, T.K., 1990, Evaporites in McIlreath, I.A., and Morrow, D.W., Eds., *Reprint Series, 4, Diagenesis: Geoscience Canada*, 141-164.
- Spencer, T.W. and Chi, H.C., 1991, Thin-layer fracture density: *Geophysics*, **56**, 833-843.
- Spry, A., 1969, *Metamorphic Textures*: Pergamon Press.
- Stanton, R.L. and Gorman, H., 1968, A phenomenological study of grain boundary migration in some common sulfides: *Econ. Geol.*, **63**, 907-923.
- Stauffer, M.R. and Gendzwill, D.J., 1987, Fractures in the northern plains, stream patterns, and the midcontinent stress field: *Can. J. Earth Sci.*, **24**, 1086-1097.

- Sun, Z., Brown, R.J., Lawton, D.C. and Wang, Z., 1991, Seismic anisotropy and salt detection: A physical modeling study: **61st Ann. Internat. Mtg., Soc. Expl. Geophys.**, Expanded Abstracts, 713-716.
- Tatham, R.H., Mathews, M.D., Sekharan, K.K., Wade, C. and Liro, L.M., 1987, A physical model study of shear-wave splitting and fracture intensity: **57th Ann. Internat. Mtg. Soc. Expl. Geophys.**, Expanded Abstracts, 642-645.
- Thomsen, L., 1986, Weak elastic anisotropy: *Geophysics*, **51**, 1954-1966.
- Wang, Z., Hirsche, W.K., and Sedgwick, G., 1991, Seismic velocities in carbonate rocks: *J. Can. Petr. Tech.*, **30**, No. 2, 112-122.
- Weiler, Y., Sass, E. and Zak, I., 1974, Halite oolites and ripples in the Dead Sea, Israel: *Sedimentol.*, **21**, 623-632.
- Wilmot, B., 1985, The geology of the Lower Cretaceous Mannville Group, Edam Saskatchewan: M.Sc. thesis, Univ. of Calgary.
- Winterstein, D.F., 1990, Velocity anisotropy terminology for geophysicists: *Geophysics*, **55**, 1070-1088.

Appendix A - P- and S-wave velocities of salt versus pressure

SAMPLE	PRESSURE(PSI)							TYPE
	000	1000	2000	3000	4000	5000	6000	
Sample A	Sample length: L = 101.683 mm							Recrystal. salt
V_P (m / s)	4043.1	4430.6	4459.8	4459.8	4469.6	4479.4	4489.3	
V_S (m / s)	2551.6	2504.5	2520.0	2625.3	2535.7	2545.3	2551.6	
V_P/V_S	1.585	1.769	1.770	1.765	1.763	1.760	1.759	
Sample B	Sample length: L = 162.13 mm							Recrystal. salt
V_P (m / s)	4448.0	4516.2	4528.8	4541.5	4547.8	4547.8	4554.2	
V_S (m / s)	2541.2	2596.2	2627.7	2638.4	2651.3	2657.9	2664.4	
V_P/V_S	1.750	1.740	1.723	1.721	1.715	1.711	1.709	
Sample C	Sample length: L = 153.40 mm							Recrystal. salt
V_P (m / s)	4389.1	4505.1	4525.0	4538.5	4551.9	4558.7	4565.5	
V_S (m / s)	2462.3	2556.7	2573.8	2593.4	2597.8	2606.6	2611.1	
V_P/V_S	1.783	1.762	1.758	1.750	1.752	1.749	1.748	
Sample D	Sample length: L = 145.43 mm							Impure salt
V_P (m / s)	4315.4	4488.6	4495.5	4509.5	4516.5	4523.5	4530.5	
V_S (m / s)	2540.3	2618.0	2627.5	2637.0	2649.0	2661.1	2680.7	
V_P/V_S	1.699	1.715	1.711	1.710	1.705	1.700	1.690	
Sample E	Sample length: L = 171.125 mm							Recrystal. salt
V_P (m / s)	4371.0	4456.4	4462.2	4473.9	4479.7	4485.6	4491.5	
V_S (m / s)	2588.9	2663.4	2673.8	2682.2	2686.4	2690.6	2694.9	
V_P/V_S	1.688	1.673	1.669	1.668	1.668	1.667	1.667	
Sample F	Sample length: L = 95.903 mm (21 °C)							Recrystal. salt
V_P (m / s)	4430.0	4545.0	4556.0	4567.0	4567.0	4578.0	4578.0	
V_S (m / s)	2716.8	2767.8	2767.8	2791.9	2800.1	2804.2	2808.3	
V_P/V_S	1.630	1.642	1.639	1.636	1.631	1.632	1.630	
Sample F	Sample length: L = 95.903 mm (70 °C)							Recrystal. salt
V_P (m / s)	4340.0	4461.0	4481.0	4492.0	4492.0	4492.0	4502.0	
V_S (m / s)		2652.9	2667.7	2678.9	2686.4	2686.4	2690.1	
V_P/V_S		1.681	1.680	1.677	1.672	1.672	1.674	
Sample G	Sample length: L = 98.978 mm							Recrystal. salt
V_P (m / s)	4499.0	4540.3	4561.2	4571.7	4582.3	4582.3	4582.3	
V_S (m / s)	2611.6	2657.1	2675.1	2689.6	2693.3	2700.6	2708.0	
V_P/V_S	1.723	1.709	1.705	1.700	1.701	1.697	1.692	

Appendix A (continued) - P- and S-wave velocities of salt versus pressure

SAMPLE	PRESSURE(PSI)										TYPE
	1450	1812	2465	2900	3625	4350	5800	7250	8700	10150	
Sample J											Detrital framework salt
V_P (m / s)	3101	3355	3596	3723	3973	4054	4153	4219	4233	4246	
V_S (m / s)	1722	1819	2023	2208	2342	2461	2601	2634	2652	2668	
V_P / V_S	1.800	1.844	1.788	1.686	1.696	1.647	1.597	1.602	1.596	1.592	

Appendix B - P- and S-wave velocities of salt versus temperature

SAMPLE	TEMPERATURE (°C)										TYPE
	21.9	32.1	39.0	56.2	66.6	83.1	96.6	107.3	139.3		
L											Detrital framework salt
V_P (m / s)	4432.0	4385.0	4358.0	4312.0	4266.0	4222.0	4191.0	4167.0	4097.0		
V_S (m / s)	2375.0	2347.0	2336.0	2332.0	2304.0	2287.0	2276.0	2260.0	2227.0		
V_P / V_S	1.866	1.868	1.866	1.849	1.852	1.846	1.841	1.844	1.840		
SAMPLE L											
V_P (m / s)	3992.0	3987.0	3976.0	3960.0	3939.0	3913.0	3875.0				
V_S (m / s)	2344.0	2342.0	2337.0	2324.0	2320.0	2306.0	2281.0				
V_P / V_S	1.703	1.702	1.701	1.704	1.698	1.697	1.699				

Appendix C - Empirical relations between seismic velocities and pressure or between seismic velocities and temperature

The following empirical formulae show the relationships between seismic velocities (both P and S) and pressure, or between seismic velocities and temperature, for different types of salt. These equations were determined by least-square linear regression based on the data measured in Core Laboratories as described in Chapter 2. The units of velocity, pressure and temperature are as follows:

velocity (v): m/s,

pressure (p): kilopounds per square inch,

temperature (T): °C.

SAMPLE	CURVE	VELOCITY EQUATION	SALT TYPE
A	P-wave	$v = 4068 + 0.40736p - 1.203 \times 10^{-4} p^2 + 1.077 \times 10^{-8} p^3$	$R^2 = 0.943$ Recrystallized
	S-wave	$v = 2489 + 1.8317 \times 10^{-2} p - 2.288 \times 10^{-6} p^2 + 1.6389 \times 10^{-10} p^3$	$R^2 = 0.997$ salt
	V_P/V_S	$V_P/V_S = 1.6241 + 2.983 \times 10^{-4} p - 2.126 \times 10^{-7} p^2 + 36.817 \times 10^{-11} p^3$ $- 1.013 \times 10^{-14} p^4 + 5.667 \times 10^{-19} p^5$	$R^2 = 0.999$
<hr/>			
B	P-wave	$v = 4451 + 7.269 \times 10^{-2} p - 1.848 \times 10^{-5} p^2 + 1.544 \times 10^{-9} p^3$	$R^2 = 0.981$ Recrystallized

S-wave	$v = 2542 + 6.541 \times 10^{-2} p - 1.379 \times 10^{-5} p^2 + 1.053 \times 10^{-9} p^3$	$R^2 = 0.997$	salt
V_P/V_S	$V_P/V_S = 1.751 - 1.590 \times 10^{-5} p + 2.155 \times 10^{-9} p^2 - 1.111 \times 10^{-13} p^3$	$R^2 = 0.981$	
<hr/>			
C			
P-wave	$v = 4396 + 0.1207 p - 3.126 \times 10^{-5} p^2 + 2.664 \times 10^{-9} x^3$	$R^2 = 0.973$	Recrystallized
S-wave	$v = 2467 + 9.9218 \times 10^{-2} p - 2.493 \times 10^{-5} p^2 + 2.081 \times 10^{-9} x^3$	$R^2 = 0.973$	salt
V_P/V_S	$V_P/V_S = 1.782 - 2.271 \times 10^{-5} p + 5.488 \times 10^{-9} p^2 + 4.444 \times 10^{-13} x^3$	$R^2 = 0.977$	
<hr/>			
D			
P-wave	$v = 4327 + 0.1751 p - 4.985 \times 10^{-5} p^2 + 4.422 \times 10^{-9} x^3$	$R^2 = 0.943$	Impure
S-wave	$v = 2545 + 8.0465 \times 10^{-2} p - 2.219 \times 10^{-5} p^2 + 2.106 \times 10^{-9} x^3$	$R^2 = 0.974$	salt
V_P/V_S	$V_P/V_S = 1.701 + 1.463 \times 10^{-5} p - 4.702 \times 10^{-9} p^2 + 3.333 \times 10^{-13} x^3$	$R^2 = 0.923$	
<hr/>			
E			
P-wave	$v = 4377 + 8.5821 \times 10^{-2} p - 2.332 \times 10^{-5} p^2 + 2.050 \times 10^{-9} x^3$	$R^2 = 0.957$	Recrystallized
S-wave	$v = 2593 + 7.841 \times 10^{-2} p - 2.120 \times 10^{-5} p^2 + 1.839 \times 10^{-9} x^3$	$R^2 = 0.970$	salt
V_P/V_S	$V_P/V_S = 1.687 - 1.706 \times 10^{-5} p + 4.595 \times 10^{-9} p^2 - 3.889 \times 10^{-13} x^3$	$R^2 = 0.983$	
<hr/>			
F			
P-wave (21 °C)	$v = 4437 + 0.1190 p - 3.311 \times 10^{-5} p^2 + 2.889 \times 10^{-9} p^3$	$R^2 = 0.955$	Recrystallized
P-wave (70 °C)	$v = 4346 + 0.1350 p - 3.806 \times 10^{-5} p^2 + 3.333 \times 10^{-9} p^3$	$R^2 = 0.978$	salt
S-wave (21 °C)	$v = 2720 + 5.269 \times 10^{-2} p - 1.212 \times 10^{-5} p^2 + 9.722 \times 10^{-10} p^3$	$R^2 = 0.985$	

$$\begin{aligned} \text{S-wave (70 }^\circ\text{C)} \nu &= 2629 + 2.850 \times 10^{-2} p - 4.782 \times 10^{-6} p^2 + 2.870 \times 10^{-10} p^3 & R^2 &= 0.994 \\ V_P/V_S(21^\circ\text{C}) & V_P/V_S = 1.6311 + 1.286 \times 10^{-5} p - 5.143 \times 10^{-9} p^2 + 5.000 \times 10^{-13} p^3 & R^2 &= 0.849 \\ V_P/V_S(70^\circ\text{C}) & V_P/V_S = 1.6773 + 6.831 \times 10^{-5} p - 3.504 \times 10^{-9} p^2 + 3.796 \times 10^{-13} p^3 & R^2 &= 0.981 \end{aligned}$$

G	P-wave	$\nu = 4500 + 4.6101 \times 10^{-2} p - 8.750 \times 10^{-6} p^2 + 5.611 \times 10^{-10} p^3$	$R^2 = 0.996$	Recrystallized
	S-wave	$\nu = 2613 + 5.2335 \times 10^{-2} p - 1.184 \times 10^{-5} p^2 + 9.639 \times 10^{-10} p^3$	$R^2 = 0.997$	salt
	V_P/V_S	$V_P/V_S = 1.723 - 1.673 \times 10^{-5} p + 4.429 \times 10^{-9} p^2 - 4.167 \times 10^{-13} p^3$	$R^2 = 0.990$	

J	P-wave	$\nu = 2165 + 0.8151 p - 1.073 \times 10^{-4} p^2 + 4.658 \times 10^{-9} p^3$	$R^2 = 0.995$	Detrital
	S-wave	$\nu = 971 + 0.6000 p - 7.172 \times 10^{-5} p^2 + 2.865 \times 10^{-9} p^3$	$R^2 = 0.997$	framework
	V_P/V_S	$V_P/V_S = 1.999 - 1.312 \times 10^{-4} p + 1.385 \times 10^{-8} p^2 - 4.775 \times 10^{-13} p^3$	$R^2 = 0.933$	salt

K	P-wave	$\nu = 3980 + 1.0253 T - 2.780 \times 10^{-2} T^2 + 1.044 \times 10^{-4} T^3$	$R^2 = 0.998$	Detrital
	S-wave	$\nu = 2346 + 3.7608 \times 10^{-2} T - 5.958 \times 10^{-3} T^2 + 1.338 \times 10^{-5} T^3$	$R^2 = 0.997$	framework
	V_P/V_S	$V_P/V_S = 1.6969 + 3.781 \times 10^{-4} T - 6.953 \times 10^{-6} T^2 + 3.215 \times 10^{-8} T^3$	$R^2 = 0.615$	salt

L	P-wave	$\nu = 4533 - 5.1662 T + 2.173 \times 10^{-2} T^2 - 5.098 \times 10^{-5} T^3$	$R^2 = 0.999$	
	S-wave	$\nu = 2411 - 2.0908 T + 1.036 \times 10^{-2} T^2 - 3.484 \times 10^{-5} T^3$	$R^2 = 0.984$	

$$V_p/V_s = 1.8795 - 4.668 \times 10^{-4}T - 9.883 \times 10^{-8}T^2 + 1.038 \times 10^{-8}T^3 \quad R^2 = 0.915$$

Appendix D - Phase and group velocity in anisotropic media of cubic symmetry

In the case of cubic symmetry, only three independent stiffness have nonzero values (Musgrave, 1970). That is, with equal values connected by lines:

$$\begin{bmatrix} C_{11} & C_{12} & C_{13} & C_{14} & C_{15} & C_{16} \\ C_{21} & C_{22} & C_{23} & C_{24} & C_{25} & C_{26} \\ C_{31} & C_{32} & C_{33} & C_{34} & C_{35} & C_{36} \\ C_{41} & C_{42} & C_{43} & C_{44} & C_{45} & C_{46} \\ C_{51} & C_{52} & C_{53} & C_{54} & C_{55} & C_{56} \\ C_{61} & C_{62} & C_{63} & C_{64} & C_{65} & C_{66} \end{bmatrix} = \begin{bmatrix} C_{11} & C_{12} & C_{13} & 0 & 0 & 0 \\ C_{12} & C_{22} & C_{23} & 0 & 0 & 0 \\ C_{13} & C_{23} & C_{33} & 0 & 0 & 0 \\ 0 & 0 & 0 & C_{44} & 0 & 0 \\ 0 & 0 & 0 & 0 & C_{55} & 0 \\ 0 & 0 & 0 & 0 & 0 & C_{66} \end{bmatrix}. \quad (D-1)$$

From the well known Kelvin-Christoffel equation, we have the Kelvin-Christoffel stiffnesses:

$$\Gamma_{jk} = \sum_{i=1}^3 \sum_{l=1}^3 n_i n_l C_{ijkl}, \quad j, k = 1, 2, 3$$

where n_i is the unit vector normal to the wavefront, and C_{ijkl} is the tensor of elastic stiffnesses.

In a medium of cubic symmetry, the Kelvin-Christoffel stiffnesses are

$$\Gamma_{11} = n_1^2 C_{11} + (n_2^2 + n_3^2) C_{44}$$

$$\Gamma_{22} = n_2^2 C_{11} + (n_1^2 + n_3^2) C_{44}$$

$$\Gamma_{33} = n_3^2 C_{11} + (n_1^2 + n_2^2) C_{44}$$

$$\Gamma_{23} = \Gamma_{32} = L = n_2 n_3 (C_{44} + C_{12}) \quad (D-2)$$

$$\Gamma_{13} = \Gamma_{31} = M = n_1 n_3 (C_{44} + C_{12})$$

$$\Gamma_{12} = \Gamma_{21} = N = n_1 n_2 (C_{44} + C_{12}).$$

Suppose $\lambda = \rho v^2$ (ρ is the density, v is the phase velocity), the Kelvin-Christoffel equation becomes

$$\begin{pmatrix} \Gamma_{11} - \lambda & N & M \\ N & \Gamma_{22} - \lambda & L \\ M & L & \Gamma_{33} - \lambda \end{pmatrix} \begin{pmatrix} P_1 \\ P_2 \\ P_3 \end{pmatrix} = 0 \quad (D-3)$$

where P_1 , P_2 and P_3 are components of the particle motion or polarization vector. In order to decide the phase velocity we require

$$\begin{vmatrix} \Gamma_{11}-\lambda & N & M \\ N & \Gamma_{22}-\lambda & L \\ M & L & \Gamma_{33}-\lambda \end{vmatrix} = 0 \quad (\text{D-4})$$

So we have:

$$(\Gamma_{11} - \lambda)[(\Gamma_{22} - \lambda)(\Gamma_{33} - \lambda) - L^2] - N[N(\Gamma_{33} - \lambda) - LM] + M[NL - M(\Gamma_{22} - \lambda)] = 0 \quad (\text{D-5})$$

This becomes a cubic equation:

$$\begin{aligned} & \lambda^3 - (\Gamma_{11} + \Gamma_{22} + \Gamma_{33})\lambda^2 + (\Gamma_{11}\Gamma_{22} + \Gamma_{22}\Gamma_{33} + \Gamma_{33}\Gamma_{11} - L^2 - M^2 - N^2)\lambda \\ & - (\Gamma_{11}\Gamma_{22}\Gamma_{33} + 2LMN) + (L^2\Gamma_{11} + M^2\Gamma_{22} + N^2\Gamma_{33}) = 0 \end{aligned} \quad (\text{D-6})$$

Equation (D-6) is a standard cubic equation as:

$$a_0\lambda^3 + a_1\lambda^2 + a_2\lambda + a_3 = 0$$

where $a_0 = 1$; $a_1 = -(\Gamma_{11} + \Gamma_{22} + \Gamma_{33})$; $a_2 = \Gamma_{11}\Gamma_{22} + \Gamma_{22}\Gamma_{33} + \Gamma_{33}\Gamma_{11} - L^2 - M^2 - N^2$ and $a_3 = -(\Gamma_{11}\Gamma_{22}\Gamma_{33} + 2LMN) + (L^2\Gamma_{11} + M^2\Gamma_{22} + N^2\Gamma_{33})$.

From (D-2) we can deduce expressions for the coefficients of (D-6):

$$\begin{aligned} -a_1 &= \Gamma_{11} + \Gamma_{22} + \Gamma_{33} = (n_1^2 + n_2^2 + n_3^2)C_{11} + 2(n_1^2 + n_2^2 + n_3^2)C_{44} \\ &= C_{11} + 2C_{44} \end{aligned} \quad (\text{D-7})$$

where $n_1^2 + n_2^2 + n_3^2 = 1$. Also,

$$\begin{aligned} & \Gamma_{11}\Gamma_{22} + \Gamma_{22}\Gamma_{33} + \Gamma_{33}\Gamma_{11} - (L^2 + M^2 + N^2) \\ &= 2(n_1^2n_2^2 + n_2^2n_3^2 + n_3^2n_1^2)C_{44}^2 + (n_1^2n_2^2 + n_2^2n_3^2 + n_3^2n_1^2)C_{11}^2 \\ &+ 2(n_1^4 + n_2^4 + n_3^4)C_{11}C_{44} + 2(n_1^2n_2^2 + n_2^2n_3^2 + n_3^2n_1^2)C_{11}C_{44} \\ &+ (n_1^4 + n_2^4 + n_3^4)C_{44}^2 - 2(n_1^2n_2^2 + n_2^2n_3^2 + n_3^2n_1^2)C_{12}C_{44} \\ &- (n_1^2n_2^2 + n_2^2n_3^2 + n_3^2n_1^2)C_{12}^2 \end{aligned}$$

Suppose $\alpha = n_1^2 n_2^2 + n_2^2 n_3^2 + n_3^2 n_1^2$, $\beta = n_1^2 n_2^2 n_3^2$, then $n_1^4 + n_2^4 + n_3^4 = 1 - 2\alpha$. And we have

$$\begin{aligned} a_2 &= \Gamma_{11}\Gamma_{22} + \Gamma_{22}\Gamma_{33} + \Gamma_{33}\Gamma_{11} - (L^2 + M^2 + N^2) \\ &= C_{44}^2 + \alpha C_{11}^2 + 2(1-\alpha)C_{11}C_{44} - \alpha C_{12}(2C_{44} + C_{12}) \end{aligned} \quad (D-8)$$

Further,

$$\Gamma_{11}\Gamma_{22}\Gamma_{33} = \beta C_{11}^3 + (\alpha - 3\beta)C_{11}^2 C_{44} + (1 + 3\beta - 2\alpha)C_{11}C_{44}^2 + (\alpha - \beta)C_{44}^3$$

and

$$2LMN = 2\beta(C_{44} + C_{12})^3.$$

Finally,

$$L^2\Gamma_{11} + M^2\Gamma_{33} + N^2\Gamma_{22} = (C_{44} + C_{12})^2[3\beta C_{11} + (\alpha - 3\beta)C_{44}]$$

So that

$$\begin{aligned} a_3 &= (L^2\Gamma_{11} + M^2\Gamma_{33} + N^2\Gamma_{22}) - (\Gamma_{11}\Gamma_{22}\Gamma_{33} + 2LMN) \\ &= (C_{44} + C_{12})^2[3\beta C_{11} + (\alpha - 3\beta)C_{44}] - 2\beta(C_{44} + C_{12})^3 \\ &\quad - \beta C_{11}^3 - (\alpha - 3\beta)C_{11}^2 C_{44} - (1 + 3\beta - 2\alpha)C_{11}C_{44}^2 - (\alpha - \beta)C_{44}^3. \end{aligned} \quad (D-9)$$

From (D-6) we have: $\lambda^3 + a_1\lambda^2 + a_2\lambda + a_3 = 0$

The roots of this are :

$$\lambda = \theta_1 \sqrt[3]{-\frac{\varepsilon}{2} + \sqrt{\frac{\varepsilon^2}{4} + \frac{\omega^3}{27}}} + \theta_2 \sqrt[3]{-\frac{\varepsilon}{2} - \sqrt{\frac{\varepsilon^2}{4} + \frac{\omega^3}{27}}} - \frac{a_1}{3} \quad (D-10)$$

$$\text{where } \varepsilon = \frac{2a_1^3}{27} - \frac{a_1 a_2}{3} + a_3, \quad \omega = a_2 - \frac{a_1^2}{3} \quad (D-11)$$

θ_1 and θ_2 are:

$$\text{for } \lambda_1 \quad \theta_1 = \theta_2 = 1$$

$$\text{for } \lambda_2 \quad \theta_1 = e^{-2\pi i/3} \quad \theta_2 = e^{2\pi i/3}$$

$$\text{for } \lambda_3 \quad \theta_1 = e^{2\pi i / 3} \quad \theta_2 = e^{-2\pi i / 3} \quad (\text{D-12})$$

Notice, if we substitute $\lambda = x - \frac{\alpha_1}{3}$ into (1) we get:

$$x^3 + \omega x + \varepsilon = 0, \quad \omega \text{ and } \varepsilon \text{ as given in (3). Note also } \theta = \sqrt[3]{1}.$$

Substituting from (D-7), (D-8) and (D-9) into (D-11), we get:

$$\omega = (c_{11} - c_{44})^2 \left(\alpha - \frac{1}{3} \right) - \alpha (c_{44} + c_{12})^2 \quad (\text{D-13})$$

and

$$\begin{aligned} \varepsilon = & \beta \left[(c_{12} + c_{44})^2 (3c_{11} - 2c_{12} - 5c_{44}) - (c_{11} - c_{44})^3 \right] + \\ & \frac{\alpha}{3} (c_{11} - c_{44})(c_{11} + c_{12})(c_{11} - c_{12} - 2c_{44}) - \frac{2}{27} (c_{11} - c_{44})^3 \end{aligned} \quad (\text{D-14})$$

$$\text{let } \delta = \frac{\varepsilon^2}{4} + \frac{\omega^3}{27} \quad (\text{D-15})$$

There are two cases to consider

$$(1) \delta \geq 0; \quad (2) \delta \leq 0$$

In case (2), $\sqrt{\delta}$ is imaginary and we have cube roots of complex numbers: $\sqrt[3]{-\frac{\varepsilon}{2} \pm \sqrt{-\delta}i}$.

Still we know that the three roots λ , are all real because of the symmetry of the Kelvin-Christoffel matrix. And indeed, the 2 imaginary parts will cancel out because $\sqrt[3]{-\frac{\varepsilon}{2} + \sqrt{-\delta}i}$ and $\sqrt[3]{-\frac{\varepsilon}{2} - \sqrt{-\delta}i}$ are complex conjugates, as are θ_1 and θ_2 . In case (1) it can be shown

that $\delta > 0$ leads to complex roots, therefore in this case $\delta = 0$ only. Introduce also

$$\phi = \tan^{-1} \left[\frac{\sqrt{-\delta}}{-\varepsilon/2} \right] = \cos^{-1} \left[\frac{-3\sqrt{3}\varepsilon}{2(-\omega)^{3/2}} \right]$$

Phase Velocity

Now, following general formulations give phase velocity of an arbitrary off-symmetry and symmetry planes in 3-D space.

P-wave phase velocity:

when $\delta < 0$

$$v_P^2 = \frac{2\sqrt{-3\varepsilon}}{3\rho} \cos\frac{\varphi}{3} + \frac{C_{11} + 2C_{44}}{3\rho} \quad (D-14)$$

SV-wave phase velocity:

$$v_{SV}^2 = \frac{2\sqrt{-3\varepsilon}}{3\rho} \cos\left(\frac{\varphi}{3} + \frac{2\pi}{3}\right) + \frac{C_{11} + 2C_{44}}{3\rho} \quad (D-15)$$

SH-wave phase velocity:

$$v_{SH}^2 = \frac{2\sqrt{-3\varepsilon}}{3\rho} \cos\left(\frac{\varphi}{3} + \frac{4\pi}{3}\right) + \frac{C_{11} + 2C_{44}}{3\rho} \quad (D-16)$$

When $\delta = 0$ the two shear waves have the same phase velocity; such points are called shear-wave singularities. The formulations can be written as:

$$v_P^2 = \frac{\sqrt[3]{-4\gamma}}{\rho} + \frac{C_{11} + 2C_{44}}{3\rho} \quad (D-17)$$

$$v_{SV}^2 = v_{SH}^2 = \frac{\sqrt[3]{4\gamma}}{2\rho} + \frac{C_{11} + 2C_{44}}{3\rho}. \quad (D-18)$$

Group Velocity

In a symmetry plane, group velocity can be determined from phase velocity by using the relation (Postma, 1955; Backus, 1965

$$V^2(\varphi) = v^2(\theta) + \left(\frac{dv}{d\theta}\right)^2. \quad (D-19)$$

Because of the symmetric feature of the unit vector (n_1, n_2, n_3) , I arbitrarily choose one of the symmetry planes (others are equivalent) have:

$$n_1 = \cos\theta, \quad n_2 = \sin\theta, \quad n_3 = 0, \quad \text{then } \alpha = \cos^2\theta\sin^2\theta, \quad \beta = 0 \quad (D-20)$$

$$V_P^2 = v_P^2 - \frac{\cos^2(\varphi/3)\sin^2(4\theta)}{48\rho^2v_P^2\varepsilon} (C_{11} + C_{12})^2(C_{11} - C_{12} - 2C_{44})^2 \quad (D-21)$$

$$V_{SV}^2 = v_{SV}^2 - \frac{\cos^2((\varphi + 2\pi)/3)\sin^2(4\theta)}{48\rho^2v_{SV}^2\varepsilon} (C_{11} + C_{12})^2(C_{11} - C_{12} - 2C_{44})^2 \quad (D-22)$$

$$V_{SH}^2 = v_{SH}^2 - \frac{\cos^2((\varphi + 4\pi)/3)\sin^2(4\theta)}{48\rho^2 v_{SH}^2 \epsilon} (C_{11} + C_{12})^2 (C_{11} - C_{12} - 2C_{44})^2 \quad (D-23)$$

At those points where the two shear waves have same phase velocity (singularities), they also have the same group velocity, given by:

$$V_P^2 = v_P^2 + \frac{(4\gamma)^{2/3}\sin^2(4\theta)}{81\rho^2 v_P^2 (4\gamma)^2} (C_{11} + C_{12})^2 (C_{11} + C_{44})^2 (C_{11} - C_{12} - 2C_{44})^2 \quad (D-24)$$

$$V_{SH}^2 = V_{SV}^2 = v_{SH}^2 + \frac{(4\gamma)^{2/3}\sin^2(4\theta)}{324\rho^2 v_{SH}^2 (4\gamma)^2} (C_{11} + C_{12})^2 (C_{11} + C_{44})^2 (C_{11} - C_{12} - 2C_{44})^2 \quad (D-25)$$